

Quantum Dynamics with Exotic Symmetries

by

Charles Nicholas Stahl

A.B., Princeton University, 2018

M.Ast., Cambridge University, 2019

A thesis submitted to the
Faculty of the Graduate School of the
University of Colorado in partial fulfillment
of the requirements for the degree of
Doctor of Philosophy
Dept. of Physics
2024

Committee Members:

Rahul Nandkishore, Chair

Michael Hermele

Andrew Lucas

Leo Radzhovsky

Markus Pflaum

Stahl, Charles Nicholas (Ph.D., Physics)

Quantum Dynamics with Exotic Symmetries

Thesis directed by Professor Rahul Nandkishore

Often the abstract will be long enough to require more than one page, in which case the macro \OnePageChapter should *not* be used.

But this one isn't, so it should.

Dedication

For whom it may concern. \mathcal{E}

Acknowledgements

Here's where you acknowledge folks who helped. But keep it short, i.e., no more than one page, as required by the Grad School Specifications.

Contents

Chapter

1	Introduction	2
1.1	Quantum dynamics and symmetry	2
1.2	Topological order and higher-form symmetry	3
1.3	Hilbert-space shattering and multipole symmetry	3
1.4	Outline of Dissertation	3
2	1-form Walker Wangs	5
2.1	Introduction	5
2.2	Self-correction in the three-fermion model	8
2.2.1	The model	9
2.2.2	Enforcing a 1-form symmetry	16
2.2.3	Diverging symmetric energy barrier	18
2.3	Paramagnetic bulk	22
2.4	Discussion	27
3	Boundary Memory	29
3.1	Introduction	29
3.2	Background	31
3.2.1	Quantum memories and nonzero temperature	31
3.2.2	Higher-form symmetries	35

3.2.3	Self-correction with a 1-form symmetry	37
3.3	Restricting to a boundary symmetry	41
3.3.1	Hamiltonian and logical operators	41
3.3.2	Enforcing the symmetry	45
3.4	Interpretation	47
3.5	Conclusions	51
4	Single-shot quantum memory	53
4.1	Introduction	53
4.2	Intertwining toric codes	56
4.2.1	Brief review of subsystem codes	56
4.2.2	In the bulk	58
4.2.3	Constructing boundaries	61
4.2.4	Logical operators	63
4.3	Errors and error correction	65
4.3.1	Local errors	67
4.3.2	Transversal logical errors	71
4.3.3	Single-shot error correction	73
4.4	Phase Diagram of the ITC	79
4.4.1	Gapped phases in the ITC	80
4.4.2	Topological order in each phase	83
4.4.3	Constructing phase diagrams	86
4.5	Remaining questions	90
5	Multipole Superfluids	93
5.1	Introduction	93
5.2	Effective action	96
5.3	Hydrodynamic phases	99

5.4 Exploring the dipole condensate	104
5.5 Discussion	105
6 Robust shattering	107
6.1 Introduction	107
6.2 Warm-up: One-dimensional pair-flip dynamics	109
6.3 The quad-flip model	113
6.3.1 Summary	113
6.3.2 Boundary conditions	118
6.3.3 Quad-flip model and robustness	120
6.3.4 Fragmentation	123
6.4 Generalized no-crossing models	126
6.4.1 Square ice	127
6.4.2 Dualities and generalized PXP models	128
6.4.3 Three-dimensional models	133
6.5 Conclusions	135
7 Conclusions	137
References	138
Appendix	
A More boundary conditions for the intertwined toric code	146
B Appendices to Hydrodynamics	149
B.1 Quasihydrodynamics	149
B.2 Derivation of the effective action	151

C Appendix to Robust shattering	155
C.1 Additional dualities	155
C.2 Enumerating sectors and frozen states	156
C.2.1 Krylov sectors in the pair-flip model	156
C.2.2 Labels in 1D with periodic boundaries	162
C.2.3 Labels in 2D with periodic boundaries	163
C.2.4 Frozen states in the QF model	164

Figures

Figure

2.1	Definition of O and U legs in the Walker-Wang model	10
2.2	Confined anyon string in the bulk of the Walker-Wang model	11
2.3	Stabilizers on the boundary of the Walker-Wang model	13
2.4	Orientation for the $T^2 \times I$ 3d 3-fermion model	13
2.5	Deconfined boundary string operators	14
2.6	The symmetry-enforced region	19
2.7	Symmetric decomposition of a boundary string operator	20
2.8	Symmetry operators at the boundary of the lattice	24
2.9	Logical operator decomposition with paramagnetic bulk	26
3.1	Decomposition of a logical operator	40
3.2	Local Hilbert space for the model	41
3.3	Stabilizers for the 3d toric code on edges	43
3.4	Stabilizers for the 3d toric code on faces	43
3.5	Stabilizers for the 2d toric code on the boundary	44
3.6	The terms we enforce	45
3.7	Excitations on the boundary	46
3.8	Removing flux from the boundary	47
3.9	Effective description of the model	49

3.10 Boundary for the \mathbb{Z}_4 model	51
4.1 Characteristic measurement outcomes in the ITC	55
4.2 Check operators in an alternative presentation of the ITC	66
4.3 Syndromes in the KVC-inspired presentation of the ITC	74
4.4 An error in the ITC and its overcomplete syndrome	79
4.5 Phase diagram for the Hamiltonian in (4.66)	87
4.6 Phase diagram for the Hamiltonian in (4.67)	87
4.7 Phase diagram for the Hamiltonian in (4.68)	89
5.1 A rough organization of the three hydrodynamic phases	95
5.2 Parametric plot of the dispersion in the charge condensate	104
5.3 Dispersion in the dipole condensate phase close to the dissipationless limit	105
6.1 Bethe lattice and height model	115
6.2 Schematic illustration of a valid configuration of noncrossing loops	117
6.3 States in the quad-flip model	125
6.4 Three dual descriptions of the same state	133
C.1 The sign convention that we introduce to define domain wall variables	155
C.2 Exact distribution of Krylov sectors in the pair-flip model	161
C.3 Constraints between horizontal and vertical labels	163
C.4 Exact counting of frozen states	166

‘What is the use of a book,’ thought Alice, ‘without pictures or conversations?’

Chapter 1

Introduction

'Twas brillig, and the slithy toves
Did gyre and gimble in the wabe:
All mimsy were the borogoves,
And the mome raths outgrabe.

Central question: What is the steady state of quantum dynamics? Think of quantum dynamics as evolution of a state throughout Hilbert space.

The least interesting steady state of quantum dynamics is the maximally mixed state, $\rho \sim \mathbb{1}$.

1.1 Quantum dynamics and symmetry

If we want to look for interesting steady states we might want to say what we mean by “interesting.” Instead, we will do the opposite. The least interesting steady state of quantum dynamics is the thermal state, $\rho \sim \exp(-\beta H)$, which is a mixture of all states, weighted by their energies. Names for evolution toward this state include thermalization and relaxation, and betray the interpretation of this state as boring.

The simplest way to avoid evolving to this state is by imposing constraints on the evolution, most naturally through a symmetry. In this case, Hilbert space splits up into symmetry sectors, labeled by eigenvalues of the symmetry operators. A particularly common symmetry to enforce is energy conservation. Averaging over all states with a particular set of symmetry numbers is called the microcanonical ensemble. In some cases, especially when considering energy conservation, it is natural to instead average over all of Hilbert space, but weight different states by their symmetry

numbers. This is called the canonical or grand canonical ensemble. The thermal state

$$\rho \sim e^{-\beta H} = \sum_a e^{-\beta E_a} |\psi_a\rangle \langle \psi_a|, \quad (1.1)$$

where $\beta = 1/T$ is the inverse temperature,

Talk about classical information storage here.

1.2 Topological order and higher-form symmetry

Landau's paradigm was certainly powerful, and for a time people believed that any violations of ergodicity beyond enforced symmetries came from spontaneous symmetry breaking. This belief began to crumble, however, with the discoveries of the integer quantum hall effect in 19-something and the fractional quantum hall effect in 19-something-else.

1.3 Hilbert-space shattering and multipole symmetry

1.4 Outline of Dissertation

In what remains of this thesis, we will explore a small sample of exotic symmetries and how they lead to interesting quantum dynamics.

In Chapter 2, we build a quantum memory inspired by Ref. [112]. This chapter generalizes the Roberts and Bartlett construction in three important ways: First, we confirm the prediction of Ref. [112] that their construction works for any so-called Walker-Wang model. Then, we show that the symmetry only needs to be enforced within some region of the model rather than the entire bulk. Finally, we construct a model consisting of a trivial paramagnet that is nevertheless self-correcting with a judicious choice of symmetry.

In Chapter 3, we continue to expand on the work of the previous chapter by constructing a symmetry-protected quantum memory where the symmetry is only enforced on the 2d boundary. The new ingredient is a topologically ordered bulk, which possesses an emergent symmetry. Thus, a symmetry exists throughout the entire model but only needs to be enforced on the boundary.

In Chapter 4, we use the results of Ch. 2 to build a single-shot quantum memory. The advantages of this construction are the physical interpretability of the construction itself and of the resulting single-shot code. We study the physical properties of the code and interpret it as a many-body quantum system with a nontrivial phase diagram.

In Chapter 5, we change gears to discuss multipole symmetries. Whereas the original motivation for these symmetries was the Hilbert-space shattering that occurs at early times, here we instead study the quantum dynamics at late times using the formalism of fluctuating hydrodynamics. We look at various hydrodynamic phases corresponding to different patterns of spontaneous symmetry breaking and how they appear in hydrodynamic dispersion relations.

In Chapter 6, we apply higher-form symmetries to the concept of Hilbert-space shattering in order to come up with models of topologically robust shattering. The shattering is robust in the sense that any dynamics compatible with the symmetry display shattering as long as they act on a finite number of spins. This is new because most existing models only display shattering for dynamics up to some finite size. We explore connections between our new model and existing models, and conjecture some other models that might display a stronger form of shattering.

Finally, in Chapter 7, we wrap up the discussions of this thesis with some connections between the chapters, some open questions, and some directions for future research.

Chapter 2

1-form Walker Wangs

Whether self correcting quantum memories can exist at non-zero temperature in a physically reasonable setting remains a great open problem. It has recently been argued [112] that symmetry protected topological (SPT) systems in three space dimensions subject to a strong constraint—that the quantum dynamics respect a *1-form symmetry*—realize such a quantum memory. We illustrate how this works in Walker-Wang codes, which provide a specific realization of these desiderata. In this setting we show that it is sufficient for the 1-form symmetry to be enforced on a sub-volume of the system which is measure zero in the thermodynamic limit. This strongly suggests that the ‘SPT’ character of the state is not essential. We confirm this by constructing an explicit example with a *trivial* (paramagnetic) bulk that realizes a self correcting quantum memory. We therefore show that the enforcement of a 1-form symmetry on a measure zero sub-volume of a three dimensional system can be sufficient to stabilize a self correcting quantum memory at non-zero temperature.

2.1 Introduction

A self correcting quantum memory can robustly store quantum information without need for active error correction, because its native dynamics suppresses errors for a time that diverges in the thermodynamic limit. The toric code in four space dimensions [70] provides a paradigmatic example of a self correcting quantum memory, in which the self correction property survives to non-zero temperature. However, whether these desirable properties can be realized in a physically reasonable system remains a great open problem. As far as we are aware, no such examples are

currently known. ‘Fracton’ models like the Haah cubic code [45] come close, but alas, at non-zero temperature the memory time saturates to some temperature dependent finite value, even in the thermodynamic limit [102, 122].

Roberts and Bartlett (R&B) have recently shown [112] that a symmetry enriched topological phase on the two dimensional boundary of a three dimensional symmetry protected topological (SPT) bulk can realize a self correcting quantum memory at non-zero temperature, if we enforce a strong constraint—namely that the dynamics respects a *1-form symmetry*. A 1-form symmetry [33, 73, 107, 128, 136] is a symmetry that acts on manifolds of co-dimension one, and thus represents a very strong constraint. This remarkable breakthrough serves as the inspiration for the present work.

In this article we show how a self correcting quantum memory may be realized in Walker-Wang models, thereby extending the R&B construction to a new family of models. Additionally, we point out in this context that it is sufficient for the 1-form symmetry to be enforced in a volume which is measure zero in the thermodynamic limit. This strongly suggests that it is inessential for the bulk to be in an SPT phase. We confirm this by constructing an example whereby enforcement of a 1-form symmetry gives rise to a self correcting quantum memory on the boundary of a *trivial* three dimensional bulk. Thus we show that enforcement of a 1-form symmetry in a measure zero sub-volume of a three dimensional system can be sufficient to give rise to self correction.

To set the stage for the discussion it is useful to first review the well known physics of toric codes [70]. The ground states of the 2d toric code are loop gasses, in that they can be written as a product of closed loop operators acting on a reference state. The ground states of the 4d toric code are membrane condensates in the same sense. We will refer to these loops and membranes as nonlocal stabilizers, because they are elements of the stabilizer group that have a large support. All elements of the stabilizer group, both local and nonlocal, are closed. One characteristic of topological order is a ground-state degeneracy on manifolds with non-trivial topology. Nontrivial operators on the ground space are non-contractible versions of the nonlocal stabilizers. In the 2d toric code they are non-contractible loops, while in the 4d toric code they are non-contractible membranes. Excitations above the ground state appear at the boundaries of open versions of nonlocal stabilizers.

For the 2d toric code these are point-like excitations on the ends of strings, while in the 4d toric code they are flux tube-like excitations on the boundary of open membranes. Finally, the 3d toric code has one sector with stabilizers that look like those of the 2d toric code and one with stabilizers that look like those of the 4d toric code. As such, its ground states can be written as loop gasses or membrane gasses.

All three toric codes have topological order at zero temperature, but have different nonzero temperature behavior. In four dimensions the toric code remains (quantum) topologically ordered up to some transition temperature $T_* > 0$, while the 2d toric code is trivially ordered for any nonzero temperature. The 3d toric code remains topologically ordered for small nonzero temperatures, but the order is classical [19]. From the information theory perspective this means the code can protect a classical probabilistic bit but not a qubit.

In both the 2d and 3d toric codes the nonzero temperature behavior can be traced to the finite energy barrier $\Delta < \infty$. The bath can lend a constant amount of energy to create two point defects and then transport them at no energy cost across the system. When they annihilate they leave behind a non-contractible nonlocal stabilizer, which we said acted nontrivially on the ground space. For the 4d toric code, the bath must create a membrane that stretches across the system. Since the energy cost of open membranes is linear in perimeter, the energy barrier to membrane operators is linear in system size. In the thermodynamic limit the energy barrier Δ is unbounded.

With this motivation, considerable work has been done to try to find 3-dimensional systems with unbounded energy barriers, and a number have been found, such as Haah's cubic code [45] and Michnicki's welded code [85]. They are collectively referred to as marginally self-correcting [122]. These codes have an energy barrier that grows less than linearly, either logarithmically (Haah's) or polynomially (Michnicki's). However, it has been shown that the bath still disorders these models at any $T > 0$, so that the memory time is bounded independent of system size [102, 122]. As in the 2d and 3d toric codes, the marginally self-correcting models have point-like excitations. At nonzero temperature these excitations exist at some nonzero density, leading to an energy barrier that is bounded by a function of the temperature.

The R&B proposal directly removes the point excitations from the picture. This is achieved by enforcing what is called a 1-form symmetry [33, 73]. Enforcing the symmetry is equivalent to giving the relevant Hamiltonian terms infinite coupling constants. For example, consider the 2d toric code. If the dynamics are restricted to states where the plaquette and vertex terms have eigenvalue +1, then no point excitations can exist. This is an example of an enforced 1-form symmetry, defined in Sec. 2.2.2. However, this is not an example of a self correcting quantum memory, because the logical operators cannot be applied transversally, i.e. as a series of local operations which respect the symmetry. Thus, enforcing a 1-form symmetry on the 2d toric code eliminates the pointlike excitations, but at the cost of our ability to apply logical operators.

The R&B proposal [112] instead creates a code that, when the symmetry is enforced, behaves like the 4d toric code in that logical operators can be applied transversally but with a large enough energy barrier that the bath applies them with probability 0 in the thermodynamic limit, at sufficiently low but non-zero temperature. This is achieved using a 2d topological order on the boundary of a 3d SPT.

In this paper we show how to achieve the same results using the 3d 3-fermion model [17], a specific example of a confined Walker-Wang model. We expect that this prescription should work for any confined Walker-Wang model [66, 133]. We show that the relevant symmetry need only be enforced “close” to the boundary, in a sense that we will explain, suggesting that the SPT nature of the bulk may be inessential to the phenomenon. We then show that a model with a trivial paramagnetic bulk can display the same phenomena. The 1-form symmetry directly protects the quantum memory by introducing an appropriate coupling between pointlike excitations on the boundary and confined fluxes in the bulk. We conclude with a discussion of 1-form symmetry protection in the topologically ordered 3d toric code and some discussion of possible future work.

2.2 Self-correction in the three-fermion model

In this section we will first define the 3d 3-fermion model in the absence of the protecting symmetry and show it is not self-correcting. We then define the 1-form symmetry and show what

nonlocal stabilizers and excitations can exist in its presence. Finally, we show the 3d 3-fermion model is self-correcting in the presence of the 1-form symmetry.

Confined Walker-Wang models—such as the 3d 3-fermion model—are a natural setting for this procedure. Like the model in Ref. [112], they describe 2d topological order on the boundary of a 3d trivial bulk. As the name suggests, they can be interpreted as models where anyons are deconfined on the boundary and confined by a linear potential in the bulk. We will see that the 1-form symmetry forces any anyons traveling across the boundary to be connected to anyons traveling through the bulk. Linear confinement in the bulk is then what gives this model an unbounded energy barrier.

2.2.1 The model

The three-fermion model can be viewed as two copies of the 3d toric code, “twisted” together so that flux from one code confines the point-like excitations of the other. To be concrete, consider a cubic lattice with two qubits on each edge. We will refer to them as σ and τ qubits, and they will be acted on by Pauli matrices written as σ^α and τ^α respectively, with $\alpha = x, z$. Two independent toric codes would have the Hamiltonian

$$\begin{aligned} H_{\text{TC}} &= - \sum_v A_v^\sigma - \sum_v A_v^\tau - \sum_f B_f^{\sigma 0} - \sum_f B_f^{\tau 0}, \\ A_v^\sigma &= \prod_{e \in \partial v} \sigma_e^x, \quad B_f^{\sigma 0} = \prod_{e \in \partial p} \sigma_e^z, \\ A_v^\tau &= \prod_{e \in \partial v} \tau_e^x, \quad B_f^{\tau 0} = \prod_{e \in \partial p} \tau_e^z, \end{aligned} \tag{2.1}$$

so that the two codes do not talk to each other at all. We will refer to the two types of terms as vertex terms and face terms. Here ∂ is the boundary operator and ∂^\dagger is the dual boundary operator. These operators are related in that $a \in \partial b$ is equivalent to $b \in \partial^\dagger a$.

In each code there are string-like operators with point-like excitations and membrane operators with loop-like excitations. We will call flipped A_v^σ terms e -particles and flipped A_v^τ terms m -particles. Since flipped B_f^σ and B_f^τ terms naturally come in dual lines, we will refer to them as σ -flux and

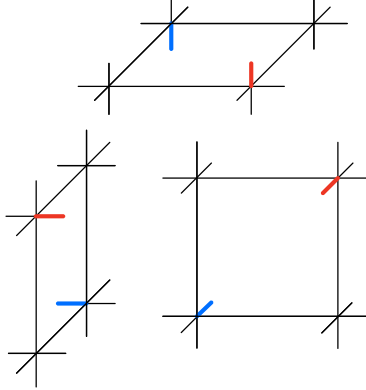


Figure 2.1: Once we have fixed a projection, we can choose the O and U legs to be the ones the lie over and under the plaquette. In this illustration the O legs are red and the U legs are blue.

τ -flux, respectively. e -particles see σ -flux (with non-trivial Berry phase) and m -particles see τ -flux. Finally, e -particles exist on the ends of e -strings, σ -flux lives on the boundaries of σ -membranes, etc.

We now twist the codes together by decorating the face operators to create the 3d 3-fermion Hamiltonian,

$$\begin{aligned}
 H_{\text{3d3f}} &= - \sum_v A_v^\sigma - \sum_v A_v^\tau - \sum_f B_f^\sigma - \sum_f B_f^\tau, \\
 A_v^\sigma &= \prod_{e \in \partial v} \sigma_e^x, \quad B_f^\sigma = \sigma_O^x \sigma_U^x \tau_U^x \prod_{e \in \partial p} \sigma_e^z, \\
 A_v^\tau &= \prod_{e \in \partial v} \tau_e^x, \quad B_f^\tau = \sigma_O^x \tau_O^x \tau_U^x \prod_{e \in \partial p} \tau_e^z,
 \end{aligned} \tag{2.2}$$

where the edges O and U lie “over” and “under” the given face, given a specific choice of 2d projection. This is shown in Fig. 2.1, where the O edges are red and the U edges are blue. We will see that the result of this decoration is that, for example, a string of σ^z operators that would usually create two deconfined e particles now also creates a line of τ -flux and two lines of σ -flux. This means point excitations are confined in the bulk.

Membrane operators are the same as they were in the toric code, being dual membranes of σ^x or τ^x operators. However, a “bare” string operator consisting of σ^z or τ^z now creates flux excitations along its entire length in addition to creating point excitations on its ends. In particular,

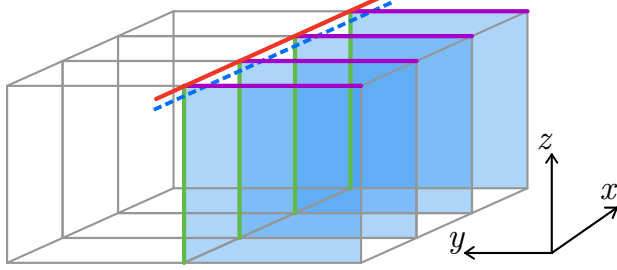


Figure 2.2: In order to define the $S_{\mathcal{C}}^e$ on the red line \mathcal{C} , first draw the line \mathcal{C}' , which is the dashed blue line. Then the “over” decoration is the purple legs and the “under” decoration is the green legs. In the end, the shaded blue faces are τ -flux. Compare to Fig. 4 in Ref. [17].

a bare string of σ^z operators creates two lines of σ -flux and one line of τ -flux. A bare string of τ^z operators creates two lines of τ -flux and one line of σ -flux.

Since this is a model of \mathbf{Z}_2 topological order, the two lines of σ -flux that a string of σ^z operators makes can be locally removed. Explicitly, we can construct the decorated string operator

$$S_{\mathcal{C}}^e = \prod_{j \in \text{under}} \tau_j^x \sigma_j^x \prod_{k \in \text{over}} \sigma_k^x \prod_{i \in \mathcal{C}} \sigma_i^z, \quad (2.3)$$

where \mathcal{C} is a curve, possibly open. To understand the decorations first draw a line \mathcal{C}' that is equal to \mathcal{C} offset infinitesimally in the $+\hat{x} - \hat{y} - \hat{z}$ direction (note this is a different direction than in [17] because our axes are aligned differently and we will access a different boundary). The decoration “over” consists of all edges adjacent to \mathcal{C} that lie over \mathcal{C}' (in our 2d projection), while the decoration “under” consists of edges adjacent to \mathcal{C} that lie under \mathcal{C}' . This configuration is shown in Fig. 2.2.

The entire configuration leaves behind a string of τ -flux, which cannot be locally removed. We therefore find that e -particles, which are created at the endpoints of $S_{\mathcal{C}}^e$, are linearly confined in the bulk.

There is also an $S_{\mathcal{C}}^m$ operator,

$$S_{\mathcal{C}}^m = \prod_{j \in \text{under}} \tau_j^x \prod_{k \in \text{over}} \tau_k^x \sigma_j^x \prod_{i \in \mathcal{C}} \tau_i^z, \quad (2.4)$$

which creates m -particles at its endpoints. It also leaves behind a single line of σ -flux, so the m -particles are also confined. Finally, there is a composite operator $S_{\mathcal{C}}^{\epsilon} = S_{\mathcal{C}}^e S_{\mathcal{C}}^m$ that creates composite ϵ particles confined by composite flux.

The flux that confines the point particles is the same as the flux on the boundary of membranes, in that both are dual lines of flipped face operators. We can then view the decorations on the string operator as a long narrow membrane whose boundary excitations cancel the superfluous flux lines. However, for both $S_{\mathcal{C}}^e$ and $S_{\mathcal{C}}^m$ there is one line of flux that cannot be canceled.

Confinement means the 3d 3-fermion model contains no topological order in the bulk, because there is no way to transport point particles across the system and return to the ground space. The result is that the 3d 3-fermion model is trivial when defined on manifolds without boundary.

On a manifold with a boundary, it is easy to terminate the code in a way that creates topological order. To do this, truncate the lattice using “smooth” boundary conditions, so that no legs are sticking out. Then truncate any stabilizers to include all their operators that act on qubits that haven’t been removed. Such stabilizers are shown in Fig. 2.3 The result is a 2d \mathbf{Z}_2 topological order where all anyons are fermions [17].

We emphasize that this is a choice of boundary conditions. It is possible to add a 2d 3-fermion model to the boundary and condense pairs, removing the topological order. However, since the boundary order is topological, it cannot be removed by arbitrarily small perturbations. Furthermore, it is possible to protect the boundary topological order by enforcing a 0-form time reversal symmetry [17]. In that sense the bulk is SPT-ordered. We will instead enforce a 1-form symmetry, as described in the next subsection.

We will consider the 3d 3-fermion model defined on a lattice with topology $T^2 \times I$, where T^2 is the torus and I is the unit interval $[0, 1]$. This can be constructed from a cubic lattice by identifying the boundaries in the x - and z -directions, so that the only true boundaries are at $y = 0, 1$. We will refer to these as the the right and left boundaries, respectively. Each boundary supports two qubits. This configuration can be found in Fig. 2.4.

We could call the topology $T^2 \times I$ the hollow donut, because it can be embedded in flat 3d

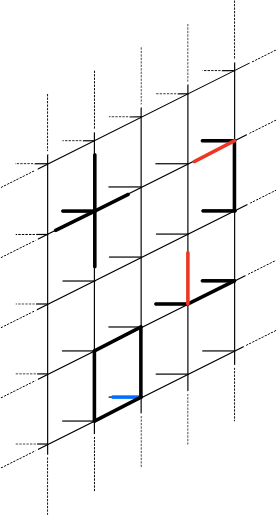


Figure 2.3: The stabilizers on the boundary are truncated versions of the ones in the bulk. Red represents O edges and blue represents U edges. The two face operators that reach into the bulk each have a U edge that is not shown (they are not truncated), while the boundary face operator does not have any O edge.

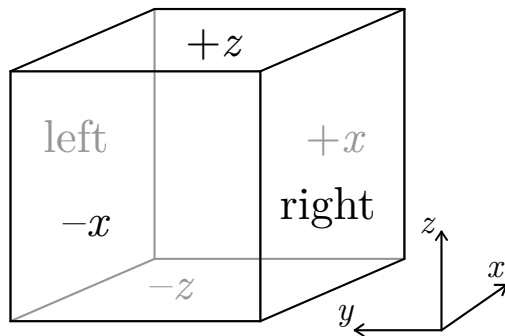


Figure 2.4: Orientation for the $T^2 \times I$ 3d 3-fermion model. The $\pm z$ sides are identified and the $\pm x$ sides are identified. The “left” and “right” boundaries at $y = 1$ and $y = 0$ respectively both have the topology of a torus. Both boundaries support two logical qubits.

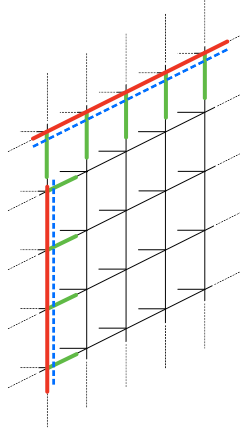


Figure 2.5: The deconfined boundary string operators are truncated versions of the bulk string operators. The dashed blue line is once again \mathcal{C}' , but now there are no “over” decorations. The green lines are the “under” decorations.

space by taking the core out of a solid donut. Then the two boundaries are the inner and outer boundary. Both boundaries have the topology of a plain old 2-torus.

If the topological order exists on the boundary, there must be logical operators supported only on boundary qubits. For the right boundary these are the deconfined string operators

$$S_{\mathcal{C}}^e = \prod_{j \in \text{under}} \tau_j^x \sigma_j^x \prod_{i \in \mathcal{C}} \sigma_i^z, \quad (2.5)$$

$$S_{\mathcal{C}}^m = \prod_{j \in \text{under}} \tau_j^x \prod_{i \in \mathcal{C}} \tau_i^z, \quad (2.6)$$

where \mathcal{C} is now a line on the boundary. These are just truncated versions of the bulk operators. Only the “under” legs get decorated because the “over” legs have been removed from the lattice.

These operators create excitations at the endpoints of \mathcal{C} but do not create flux along their length. In fact, if we compare to Fig. 2.2, we see that the faces where the confining flux would exist have been removed from the lattice. We can think of the flux as having been removed at the boundary by the decorations. Fig. 2.5 shows these decorations.

Since there is no flux left, both types of string operators create deconfined anyons. Thus we have topological order. If \mathcal{C} is a noncontractible closed loop on the boundary, then the corresponding

string operators are nontrivial operators on the ground space.

We will refer to a deconfined boundary string operator that wraps the vertical direction as S_{vert} and one that wraps the horizontal direction as S_{horiz} . It is easy to check that

$$\{S_{\text{vert}}^e, S_{\text{horiz}}^m\} = \{S_{\text{horiz}}^e, S_{\text{vert}}^m\} = 0 \quad (2.7)$$

while all other pairs commute. Thus we could encode the logical operators as $Z_1 = S_{\text{vert}}^e$, $X_1 = S_{\text{horiz}}^m$, $Z_2 = S_{\text{vert}}^m$, and $X_2 = S_{\text{horiz}}^e$, or any unitary transformation of that encoding. Similar string operators exist on the left boundary.

We previously mentioned the membrane operators in the model are the same as those in the 3d toric code. The membrane operators also appear as logical operators for the boundary topological order, with the caveat that they act nontrivially on both boundaries. For example there is

$$R_{\text{horiz}}^\sigma = \prod_{i \in \mathcal{M}^*} \sigma_i^x, \quad (2.8)$$

which consists of σ^x operators on every edge in a horizontal dual membrane \mathcal{M}^* . On the right boundary this acts as X_1 , while it will also have a logical action on the left boundary.

The bath is able to transport deconfined point particles across the a system at any temperature above zero. This is the case in both the 2d and 3d toric code. In our case, all logical operators can be applied by transporting a deconfined point excitation across a boundary. 3D3F cannot store any information, even classical, at nonzero temperature. The same is true of confined Walker-Wang models in general. The topological order behaves the same as a 2d topological phase placed on the boundary of a trivial 3d bulk phase. We can however couple the boundary and the bulk using a higher-form symmetry as described below.

2.2.2 Enforcing a 1-form symmetry

Here we define p -form symmetries, which for $p > 0$ are called higher-form symmetries. A p -form symmetry consists of symmetry operators each associated with a closed $(d - p)$ -dimensional submanifold of our space. The simplest examples, 0-form symmetries, are just ordinary global symmetries. They act on closed d -dimensional submanifolds, so they have to act on the whole space.

It may be unintuitive to think about symmetry operators that act on lower dimensional submanifolds. But toric codes actually provide convenient settings to think about them. In the 3d toric code, arbitrary products of vertex operators form (dual) membrane operators. These operators commute with the Hamiltonian, so they form a symmetry. They are defined on $(2 = d - 1)$ -dimensional submanifolds, so they form a 1-form symmetry.

We can write this symmetry group as $G = \langle A_v \rangle$, which means that G is the group generated by all the A_v operators. The face terms form a 2-form symmetry $G' = \langle B_f \rangle$, but we are not concerned with that here.

Since the vertex terms were not affected when we twisted our toric codes together, the 3d 3-fermion model inherits the same 1-form symmetry. In particular, the symmetry group is

$$G = \langle A_v^\sigma \rangle \times \langle A_v^\tau \rangle, \quad (2.9)$$

the group generated by both types of vertex terms.

Recall that we wanted to get rid of point-like excitations on the boundary. We can do this by initializing the system in a state $|\psi\rangle$ that satisfies $g|\psi\rangle = |\psi\rangle$ for every g in G . This includes the ground state and any state reached from the ground state by acting with open membrane operators. We then require that the dynamics obey the symmetry, so that no point particles are created. We will refer to this process as enforcing the symmetry G .

When we couple the system to a bath we can enforce G by ensuring that all of the bath couplings commute with every element in G . This procedure is equivalent to giving A_v^σ and A_v^τ infinite coupling constants. Enforcing the symmetry also prevents any open string operators. The

symmetry still allows closed strings and open or closed membranes.

Enforcing the symmetry G ensures that every state in a local decomposition performed by the bath will respect the symmetry G . We will refer to this type of decomposition as a symmetric local decomposition [112].

Because the symmetry allows open membranes, any logical membrane operator can be decomposed into a series of local operations that do not break the symmetry. Logical string operators, on the other hand, must include open strings in their local decompositions. This means that while logical string operators can be applied in the presence of the symmetry (because they are closed), they cannot be applied transversally without breaking the symmetry.

The “problem” operators in the 3d 3-fermion model are the deconfined boundary string operators. Since the deconfined strings only exist on the boundary, it is tempting to only enforce the symmetry on the boundary. However, we can then create a string operator that lies mostly on the boundary but whose endpoints are in the bulk. Then the symmetry is only violated in the bulk, but the energy barrier is small.

If we enforce the symmetry in the bulk, then configurations that look like boundary anyons must be accompanied by bulk flux. Consider a closed string that intersects the boundary but is not entirely included in the boundary. Then on the boundary this looks like an open string that would create point excitations at its endpoints. However, at these “endpoints” the string instead goes into the bulk, where it is now confined and creates flux.

In this sense the 1-form symmetry couples bulk excitations to boundary excitations. This perspective will become most clear when we couple a 2d toric code to a paramagnet bulk in Sec. 2.3.

If the 1-form symmetry is enforced to a distance W from the boundary, a nontrivial logical operator can be symmetrically decomposed into a series of strings whose endpoints are at least a distance W from the boundary. In the following subsection we will define the symmetric energy barrier as the amount of energy the bath must provide in order to perform a logical operation. For the partially symmetry-protected 3d 3-fermion model it is $\Delta \sim W$.

2.2.3 Diverging symmetric energy barrier

Since we assume the bath couples to the system locally, it can only apply a logical operator by decomposing it into a series of operators that differ by local operations. These operators generically create excitations in the system. Informally, the energy barrier is the energy of these excitations. We define the energy barrier more formally following Ref. [112].

First assume the bath couples to the system through local Pauli operators. Let $\bar{\ell}$ be a (nontrivial) logical operator. Define the local decomposition of $\bar{\ell}$ as a series of operators $\mathcal{D}(\bar{\ell}) = \{\ell^{(k)} | k = 1, \dots, N\}$, where $\ell^{(1)} = I$ and $\ell^{(N)} = \bar{\ell}$. Furthermore, $\ell^{(k)}$ and $\ell^{(k+1)}$ differ only by a local (constant-range) set of Pauli operators. Since every Pauli operator either commutes or anti-commutes with each stabilizer, each of the $\ell^{(k)}$ anticommutes with a finite number of stabilizers and commutes with the rest.

If $|\psi_0\rangle$ is a ground state of the Hamiltonian, then $\ell^{(k)} |\psi_0\rangle$ is an eigenstate with energy $E^{(k)}$.

Define the energy barrier for this particular local decomposition as

$$\Delta_{\mathcal{D}(\bar{\ell})} = \max_k (E^{(k)} - E_0), \quad (2.10)$$

where E_0 is the ground state energy. Then the energy barrier for the system is

$$\Delta = \min_{\bar{\ell}, \mathcal{D}(\bar{\ell})} \Delta_{\mathcal{D}(\bar{\ell})}, \quad (2.11)$$

where the minimization is taken over all local decompositions of all logical operators. Thus the system energy barrier Δ can be thought of as the minimum amount of energy that the bath must supply to perform a nontrivial logical operation.

We now turn our focus to the $L \times L \times L$ 3d 3-fermion model, with the 1-form symmetry enforced within distance W of the boundary as in Fig. 3.6. We want to show that the energy barrier for a boundary string operator is of order W . For concreteness let the string be S_{vert}^e , but similar constructions exist for the other strings.

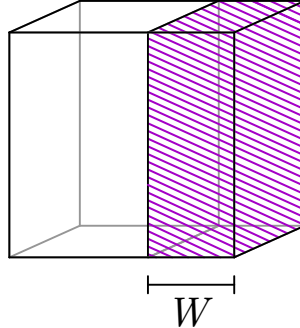


Figure 2.6: The 1-form symmetry will be enforced within a distance W from the right boundary.

In order to symmetrically decompose the operator, we just need to make sure the string never has an endpoint in the protected region. We start with a small loop near the boundary, as in Fig. 2.7. Any part of the loop on the boundary will create no flux, while any part of the loop in the bulk will create flux.

It is possible to move the string operator using local sets of Pauli operators since if \mathcal{C} and \mathcal{C}' only differ in a single region, then $S_{\mathcal{C}}^e$ and $S_{\mathcal{C}'}^e$ only differ in the same region. We use this method to pull the edge of the loop into the unprotected region so that we are allowed to open it, breaking the 1-form symmetry. At this point (Fig. 2.7 ii) we have a deconfined string operator on the boundary and two confined string operators reaching into the bulk. The excitations are two point excitations with energy cost ~ 2 and two flux tubes with energy cost $\sim 2W$.

We now move the confined strings in the vertical direction until they annihilate, leaving behind a deconfined logical string operator on the boundary. As $W \rightarrow \infty$ the largest energy cost comes from the flux tubes, so the symmetric energy barrier is $\Delta \sim W$.

As long as we ensure that W grows without bound as we take the thermodynamic limit, this shows that 1-form symmetry protection can endow the 3d 3-fermion model with a diverging energy barrier. Furthermore, Ref. [112] shows that in this type of model, a diverging energy barrier is sufficient to ensure self-correction.

Note that this means that W need not scale as any particular function of L . We could take the thermodynamic limit in such a way that $W/L \rightarrow 0$ as long as both grow without bound, for

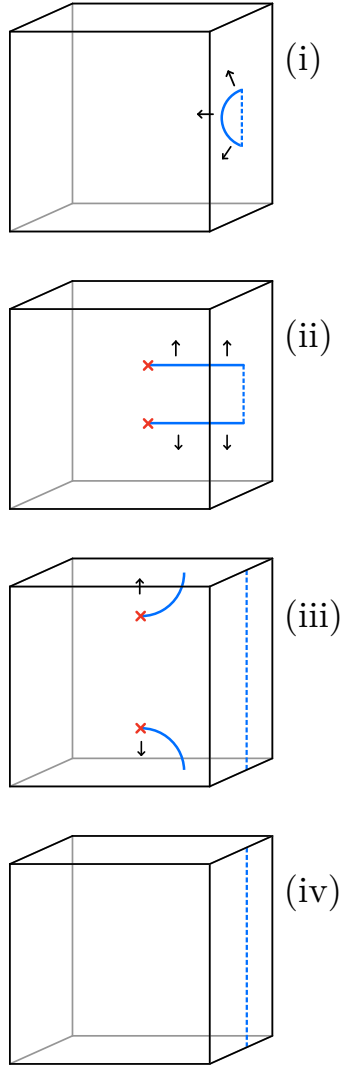


Figure 2.7: Symmetric decomposition of a boundary string operator. Dashed blue lines represent deconfined boundary strings and solid blue lines represent bulk strings with flux. Red asterisks are point excitations. (i) Start with a small loop near the boundary and expand it away from the boundary. (ii) Open the loop when it is outside the symmetry-protected region. (iii) Move the bulk anyons and flux vertically, stretching the boundary deconfined string. (iv) Annihilate the bulk excitations, leaving behind a boundary deconfined logical string operator. Compare to Fig. 12 in Ref. [112].

example by taking $W \sim \log L$. Then the symmetry would be enforced in a measure zero sub-volume in the thermodynamic limit. In this sense the quantum memory only requires that the symmetry be enforced near the boundary, not in the whole bulk. This is our first signal that we are not relying on the existence of an SPT phase.

We could have let the two non-contractible directions have lengths L_1 and L_2 and not required $L_1, L_2 > W$. In that case the energy barrier scales as $\Delta \sim \min\{L_1, L_2, W\}$, reproducing the above scaling when $W > L_1, L_2$. This scaling is reminiscent of the behavior in Ref. [112]. If the vertical direction is smaller than W , then it is more energy efficient to first make the loop very large in the vertical direction until it splits into a nontrivial boundary loop and a nontrivial bulk loop, as in Fig. 12 of [112]. The bulk loop can then be moved to the unprotected region, broken, and removed.

Before moving on we will mention what happens if we enforce the symmetry everywhere in the bulk, as in the R&B proposal [112]. In that case, any logical operator with a symmetric local decomposition must have a nontrivial logical action on both boundaries. Comparing to Fig. 2.7, the closed string may never open, so it has to end up as a nontrivial loop on the left boundary.

We previously said that membrane operators had to have logical actions on both boundaries. In confined Walker-Wang models, for any closed string operator there is some dual membrane operator with the same action on the ground space. This is because arbitrary products of face operators B_f^σ and B_f^τ create open dual membranes with string operators around their perimeters.

Under a certain encoding of logical qubits 3 and 4 in the left boundary, the logical operators that can be locally decomposed are

$$\begin{aligned} X_1 X_3 &= R_{\text{horiz}}^\sigma, & Z_1 Z_3 &= R_{\text{vert}}^\tau \\ X_2 X_4 &= R_{\text{horiz}}^\tau, & Z_2 Z_4 &= R_{\text{vert}}^\sigma. \end{aligned} \tag{2.12}$$

Note that these operators can generate any Pauli on a given qubit, but they are constrained to commute with each other. This is analogous to the 3d toric code, where 1-form symmetry-protection means that only membrane operators can be symmetrically decomposed.

The 3d 3-fermion model is a confined Walker-Wang model. All models in this family have confined anyons in the bulk and deconfined anyons on the boundary. Thus, all these models have trivial bulks with 2d topological order on the boundary. For any confined Walker-Wang model it should be possible to follow the above procedure of enforcing the 1-form symmetry within a distance W of the boundary to achieve a energy barrier that scales as $\Delta \sim W$.

To close this section, we should connect to the 3D cluster state model of Raussendorf, Bravyi and Harrington, the RBH model, which was the original setting for the R&B proposal [112]. Like the confined Walker-Wang models, this model is trivial in the bulk and can have boundary conditions that create topological order. When defined on the topology $T^2 \times I$ with the symmetry enforced within a distance W of one boundary, the RBH model protects two qubits at that boundary at nonzero temperature.

2.3 Paramagnetic bulk

In the previous section we saw how enforcing a 1-form symmetry on an SPT system could give rise to self correction. We also saw that the symmetry need not be enforced in the whole bulk, which leads one to wonder if the SPT nature of the bulk was really necessary. Here we present a construction inspired by Sec. III.G of [112], in which the symmetry provides self-correction, using a non-interacting paramagnet for the bulk Hamiltonian. Since trivial paramagnets are by definition not in an SPT phase, this makes clear that the self-correction seen in these models is not an SPT effect, but rather follows purely from the 1-form symmetry.

Consider qubits placed on faces and edges of a cubic lattice. As before, let the lattice have topology $T^2 \times I$. On the boundaries, only put qubits on edges. For simplicity we will refer to the sets of bulk cubes, faces, edges, and vertices as Q, F, E and V , respectively. We will refer to the sets of boundary faces edges and vertices as $\partial F, \partial E$, and ∂V , respectively.

The Hamiltonian in the bulk is

$$H_{\text{para}} = - \sum_{f \in F} X_f - \sum_{e \in E} X_e, \quad (2.13)$$

acting on all face and edge qubits. The boundary Hamiltonian is just a toric code,

$$H_{\text{TC}} = - \sum_{v \in \partial V} A_v^\partial - \sum_{f \in \partial F} B_f^\partial, \quad (2.14)$$

where A_f^∂ and B_f^∂ are the normal 2d toric code terms, acting only on the boundary edge qubits.

Recall there are no boundary face qubits.

The symmetry operators in the bulk are simply

$$A_v = \prod_{e \in \partial^{\dagger} v} X_e, \quad A_c = \prod_{f \in \partial c} X_c, \quad (2.15)$$

with one operator for each vertex and each cube. These clearly commute with the bulk Hamiltonian.

We will give explicit definitions of the boundary symmetry operators but they are rather complicated so they are depicted in Fig. 2.8.

On the boundary vertices, the symmetry operators are

$$A'_v = \prod_{e \in \partial^{\dagger} v} X_e, \quad (2.16)$$

which is a five-body operator because v is on the boundary. For any cube whose boundary contains a boundary face, the symmetry operator is

$$A'_q = \prod_{e \in \partial f^{(0)}} Z_e \prod_{f \in \partial q} X_f, \quad (2.17)$$

where $f^{(0)}$ is the unique face in ∂q on the boundary lattice. Recall the boundary faces have no qubits on them so A'_q contains 5 X -type operators. In addition, it is dressed by a 4-body Z -type

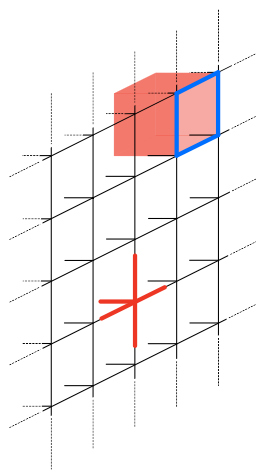


Figure 2.8: Symmetry operators at the boundary of the lattice. The A'_v operator (lower left) consists of five X_e terms, while the A'_q operator (upper right) has five X_f terms and four Z_e terms on the boundary. Restricting these terms to the boundary edges results in the terms in the boundary toric code Hamiltonian.

term on boundary qubits. See Fig. 2.8 for illustrations.

The group generated by A_q , A_v , A'_q , and A'_v is a 1-form symmetry because elements of the group act on codimension-1 objects. Elements generated by A_v and A'_v consist of X operators on sets of edges forming dual membranes. These dual membranes may terminate at the lattice boundary. Elements generated by A_q and A'_q consist of X operators acting on sets of faces forming direct membranes. A membrane \mathcal{M} may terminate at the lattice boundary if it is decorated by Z operators on the edges that make up $\partial\mathcal{M}$. This decoration comes from the decoration in Eqn. 2.17.

Unsurprisingly, the topological order lives in the 2-dimensional toric code at the lattice boundary. The logical operators are, as always, either direct strings of Z operators or dual strings of X operators.

Neither of these strings can be symmetrically decomposed using open boundary strings, the way they would be decomposed in a 2d toric code. Open Z -strings anticommute with A_v operators at their endpoints. This can be fixed by pairing with a string of Z operators through the bulk. Similarly, open dual X -strings anticommute with A_q operators at their endpoints and must be paired with dual Z -strings through the bulk. See Fig. 2.9 for these local symmetric decompositions.

Direct and dual Z -strings in the bulk commute with the 1-form symmetry because they intersect every cube or vertex term twice. However, they have linear energy cost because they anticommute with the paramagnet Hamiltonian. We can once again call them fluxes. The 1-form symmetries enforce that the fluxes can only end on the endpoints of open line operators on the toric code boundary or in regions where the symmetry is not enforced.

We find ourselves in a position similar to the 3d 3-fermion model, where boundary anyons are confined by flux strings in the bulk. Thus, we can decompose logical operators using the steps in Fig. 2.7. Once again we find that the topologically nontrivial operators that can be symmetrically decomposed into strings that intersect the boundary but end deep in the bulk. Bulk strings are linearly confined, so the symmetric energy barrier for this system diverges.

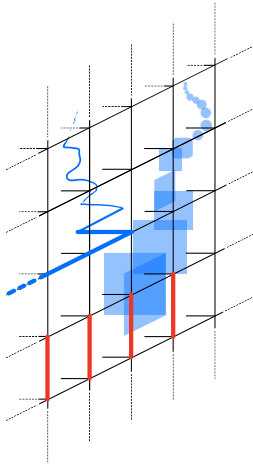


Figure 2.9: In order to decompose the boundary logical operators in the presence of the 1-form symmetry, we need to connect boundary strings to bulk strings. The Z -type boundary string can simply be connected to a Z -type bulk string defined on edges, so that the entire string has no endpoints. The X -type boundary string anti-commutes with two A'_q operators at its endpoints. These can also be seen as the endpoints of a bulk dual Z -string, so a combination of a boundary dual X -string on edges and a bulk Z -string on faces commutes with the symmetry. In both cases the bulk string creates excitations, and is linearly confined.

2.4 Discussion

The purpose of this paper have been to relate the R&B construction to other existing models and to determine what aspects of the construction are most important for achieving self-correction. We showed that enforcing the 1-form symmetry in any confined abelian Walker-Wang model results in self-correction. Ref. [112] conjectured that this might be possible, and indeed it is. In the process we discovered that it suffices to enforce the symmetry in a measure zero sub-volume of the system. This then led us to conjecture that it might be possible to achieve self correction with a paramagnetic bulk, and indeed, we were able to demonstrate this by explicit construction. This strongly suggests that it is the 1-form symmetry that does the heavy lifting, and any ‘exotic’ nature of the bulk is optional.

The approaches we have discussed achieve self-correction by giving anyons effective long-range interactions, by tying them to confined bulk flux strings. Thus they could be compared to earlier literature that also tried to utilize long-range interactions to achieve self correction [7, 21, 47, 56, 57, 99, 100, 137]. Those attempts were limited by requirements for unbounded operator strength and/or instability to perturbation [15, 75]. If we enforce the 1-form symmetry by endowing certain terms in the Hamiltonian with infinite coupling constants, then the R&B proposal (and our extensions thereof) suffer from the same limitations.

Since we do not use any exotic bulk properties, we should ask if we can improve the construction by using a more interesting bulk. A key direction for future work is whether 1-form symmetry can naturally emerge in the dynamics of some quantum system. In this context, R&B conjectured that the 3d gauge color code [10] (gcc) might realize an emergent 1-form symmetry (including at non-zero temperature). However, the proof or disproof of this conjecture remains an open problem [72], as does identification of other potential platforms for emergent 1-form symmetry at non-zero temperature. An alternative direction to pursue might be to seek quantum computational architectures where 1-form symmetry may be natively enforced, for instance through single shot error correction [11, 114].

The appeal of the 3d gauge color code is that the flux tubes do not end in the bulk. The reason for the 1-form symmetry in the bulk in the R&B proposal and in this paper was to prevent the flux tubes from terminating, so the 3d gcc would not need this constraint. The 3d toric code is a useful point of comparison for the 3d gcc. Like the 3d gcc, the 3d toric code has flux tubes that do not terminate in the bulk. If it were possible to couple the endpoints of these flux tubes to boundary anyons this may result in some nonzero-temperature stability, even without higher-form symmetry enforcement. The difficulty of understanding emergent higher-form symmetry can also be seen in the 3d toric code, which has an emergent 1-form symmetry at $T = 0$ but not at nonzero temperatures.

We could consider enforcing a 1-form symmetry in the bulk of a pure 3d toric code, with no boundary anyons. This prevents the creation of point excitations, so the stringlike operators cannot be locally decomposed. In the case of the 3d toric code this does promote the code to be self-correcting. The cost is that some logical operators now have no symmetric local decomposition.

Lastly, we wonder what ingredients can be added to these models to improve the finite temperature behavior. Possibilities could include a mix of 3-dimensional and 2-dimensional topological order or boundaries between different phases instead of boundaries with the vacuum. It might be useful to use the process of welding [85], which is known to create a code with a power-law energy barrier at $T = 0$. Furthermore, fracton phases (see [92] for a review) give access to new kinds of bulk order that could be also useful in this quest. We leave these explorations to future work.

Chapter 3

Boundary Memory

Recent work has shown that a self-correcting memory can exist in 3 spatial dimensions, provided it is protected by a 1-form symmetry. Requiring that a system's dynamics obey this type of symmetry is equivalent to enforcing a macroscopic number of symmetry terms throughout the bulk. In this paper, we show how to replace the explicit 1-form symmetry in the bulk with an emergent 1-form symmetry. Although the symmetry still has to be explicitly enforced on the boundary, this only requires $\mathcal{O}(L^2)$ terms instead of $\mathcal{O}(L^3)$ terms. We then reinterpret this boundary as a symmetry-protected topological defect in a bulk topological order. Defects can have interesting memory properties even in the absence of symmetry.

3.1 Introduction

Systems that can store quantum information for an extended period of time while interacting with a noisy environment will be integral components in any scalable implementation of quantum computation. Two important classes of such systems are *fault-tolerant* quantum memories and *self-correcting* quantum memories. From the perspective of condensed matter physics, fault-tolerant quantum memories can store quantum information indefinitely while evolving at zero temperature in the thermodynamic limit, even in the presence of small perturbations. The paradigmatic example is the two-space-dimensional (2d) toric code [70], which is *topologically ordered*. Topologically ordered systems [135] can generically provide fault tolerance by storing quantum information in their space of degenerate ground states. On the other hand, self-correcting quantum memories must

be able to store quantum information indefinitely even at some nonzero temperatures, again in the thermodynamic limit. While the 4d toric code [25] is self-correcting, there are no known examples in three dimensions. The 4d toric code remains topologically ordered in the temperature range in which it is self-correcting [51], but there is no general mathematical result on the connection between self-correction and finite-temperature topological order [112]. The existence of robust self-correction in 3d remains an open question.

The hunt for self-correction in systems with generic dynamics has generated interesting physics even where it hasn't achieved its central goal. In 2d, the introduction of exactly-solvable models has shed light on the classification of topological phases. In 3d, a direct search over a space of models [45] did not result in self-correction [102, 122], but did kick off the study of fractons [92, 104, 132].

In a parallel line of development, progress has been made by coupling toric codes to 2d [47] or 3d [100] bosons. In the presence of diverging couplings (for the 2d bosons) or fine-tuned dynamics (for both), the bosonic systems can restore self-correction to the toric code. Generic perturbations destabilize the memory properties [75].

A more recent model from Roberts and Bartlett [112] achieves a similar result by coupling to a bulk lattice spin model, with the advantage that bulk local Hilbert spaces are finite-dimensional. The model still requires fine-tuned dynamics, but encodes the fine-tuning in a *higher-form symmetry*. Higher-form symmetries [33, 73, 93] are local symmetries that are not gauge symmetries, in that states related by a symmetry transformation are not identified as physically equivalent. The locality of the symmetry means that requiring the dynamics to respect the symmetry is a very strong constraint. For the model in Ref. [112], the dynamics must respect a number of constraints that scales with the volume of the system. We will refer to the model as the Roberts-Bartlett model.

In this paper, we show that the bulk higher-form symmetry need not be enforced. Instead, we only need to enforce the symmetry on the boundary. First, in Sec. 3.2 we review the physics of the existing models of quantum memories. Along the way, we look for insight into what role the higher-form symmetry plays in self-correction in the Roberts-Bartlett model. Then, in Sec. 3.3 we construct

a new model that only requires a higher-form symmetry to be enforced on the boundary. The new model has a topologically ordered bulk, so there is an emergent bulk higher-form symmetry [136], which need not be enforced. We discuss the physical interpretation of the new model as a topological defect in Sec. 3.4. Finally, we ponder some possible future directions in Sec. 3.5.

3.2 Background

Here we will review the physics that will be useful in motivating and understanding the model presented in the next section. First we will focus on various quantum memories and behavior at temperatures above zero. That material is reviewed thoroughly in Ref. [15]. We next define higher-form symmetries, leaning on the toric code for interpretation. Then, we motivate the power of higher-form symmetries for quantum memories and introduce the Roberts-Bartlett model.

3.2.1 Quantum memories and nonzero temperature

Quantum memories store quantum information for an extended period of time by using special protected states. We call the states logical states, and the operators that act within the space of logical states are logical operators. The error model that acts on the quantum memory can not apply logical operators, possibly up to some probability cutoff or timescale. In this sense quantum memories are a generalization of quantum error-correcting codes, which are in turn a generalization of classical error correcting codes.

In this paper we will focus on Hamiltonian lattice models, where the logical states are ground states of the system. The first such system that was studied as a quantum memory was the toric code [70]. This is a 2d lattice model, with qubits living on the edges of the lattice. The Hamiltonian is

$$H_{\text{TC}} = - \sum_v A_v - \sum_f B_f, \quad (3.1)$$

$$A_v = \prod_{e \in \partial^\dagger v} X_e, \quad B_f = \prod_{e \in \partial f} Z_e,$$

where ∂f is the four edges in the boundary of the face f , and $\partial^\dagger v$ is the four edges that form a “star”: the dual boundary of the vertex v . We use X and Z to denote the Pauli matrices σ^x and σ^z , respectively.

All A_v and B_f terms commute with each other. The only time this is not obvious is when the vertex v is on the boundary of the face f . In that case, A_v and B_f share two edges and the signs from commuting two X operators past two Z operators cancel, so the full terms commute. Since all terms in the Hamiltonian can be simultaneously satisfied, the model is exactly solvable. Ground states are +1 eigenstates of all A_v and B_f operators. Carefully counting the degrees of freedom and the ground state constraints shows that, while the constraints locally use up all the degrees of freedom, there are some global degrees of freedom that are not constrained, giving degenerate ground states. The ground state degeneracy depends on the topology of the manifold on which the lattice is placed.

The spectrum of the toric code contains anyons, or topologically charged excitations. The topological charge means that the anyons have nontrivial Aharonov-Bohm phases with respect to each other. Incomplete logical operators create and remove anyons at their endpoints, or transport anyons. Complete logical operators (defined on topologically nontrivial closed strings) tunnel anyons across the system in non-contractible loops. Even when perturbations are introduced to (3.1), the tunneling amplitude is exponentially small in system size. As a result, the system can evolve under its own dynamics for a time τ without losing the stored information. As long as the system is at absolute zero temperature, the memory time τ diverges in the thermodynamic limit, up to some critical perturbation strength [25]. As we said before, this is the defining feature of fault-tolerant quantum memories.

The toric code and related systems possess topological order [135], a type of order with no local order parameter. Instead, the different ground states can only be distinguished by order parameters that are topologically nontrivial. In fact, the order parameters are the previously-mentioned logical operators. Due to the absence of local order parameters, the topological order is robust to small perturbations. By this we mean that the distinct ground states remain degenerate, up to corrections

that are exponentially small in system size. Clearly, the fault-tolerant nature of the quantum memory is intimately related to the existence of topological order in the ground state, or at $T = 0$.

At any nonzero temperature, the 2d toric code is not topologically ordered [51]. Heuristically, this is because at any $T > 0$, the anyons exist at some finite density. As the system reaches thermodynamic equilibrium, these anyons wander along paths than can be large compared to the system size, connecting the different ground states. The result is that there is only a single equilibrium thermal state, and it does not possess topological order. This suggests that the 2d toric code can not store quantum information indefinitely at $T > 0$, but the lack of topological order is an equilibrium property, while any quantum memory properties must be dynamical.

We will discuss the dynamics of quantum systems evolving at nonzero temperatures following the conventions of Ref. [112]. To model the evolution of a system with Hamiltonian H_{sys} at some nonzero temperature, we evolve with the full Hamiltonian

$$H_{\text{full}} = H_{\text{sys}} + H_{\text{bath}} + \lambda \sum_{\alpha} S_{\alpha} \otimes B_{\alpha}, \quad (3.2)$$

where H_{bath} is the bath Hamiltonian. The index α runs over local operators on the system S_{α} with some corresponding operators on the bath B_{α} .

When a thermal bath disorders a memory, it does so by applying a logical operator. From Eqn. 3.2, this happens when some product of S_{α} form a logical operator. Thus, the bath can only apply logical operators transversally, or as a series of local operators, each of which is an incomplete logical operator. Incomplete logical operators always anticommute with some terms in the Hamiltonian, so the transveral application of a logical operator must overcome some energy barrier.

It turns out that the 2d toric code cannot store quantum information indefinitely at $T > 0$ without active correction [25]. As with the topological order, the problem is that the point-like anyons exist at finite density at finite temperature, and can wander across the system.

The 4d toric code [25] is analogous to (3.1) but in 4 dimensions with qubits on faces, A_e terms

on edges, and B_c terms on cubes. It evades the issues with finite densities of anyons because the logical operators live on membranes that stretch across the whole system. The topologically-charged excitations, which now live on the boundaries of incomplete logical membranes, are loop-like. A finite temperature bath can create loop excitations of any finite size, but larger loops are suppressed by having larger energy. As the system size L increases, the time that we have to wait for the bath to create L -sized loops increases without bound. In fact, the system prefers to shrink any loops that do exist in order to lower the energy. A system that is able to correct errors generated by the bath in this sense is self-correcting.

In the thermodynamic limit, the bath never creates loops that are as large as the system, so quantum information can be stored indefinitely. In addition, the 4d toric code does remain topologically ordered for nonzero temperatures up to a critical temperature T_c . Above T_c the 4d toric code is also no longer self-correcting. Thus, self-correction appears to be related to topological order at $T > 0$ in the same sense that fault tolerance is related to topological order at $T = 0$. The 4d toric code is self-correcting and possesses topological order below T_c . Sadly, our world only has 3 spatial dimensions, so we would like to reproduce this behavior in a 3d system.

A feature that distinguishes the 4d toric code from the 2d toric code is that it has an unbounded energy barrier: applying any logical operation through a series of local operation requires traversing a high-energy state, whose energy continues to increase for larger system sizes. The energy of such a state is called the energy barrier of the logical operator. One might be tempted to draw the conclusion that an unbounded energy barrier is sufficient for self-correction. This seems reasonable because operations that cost a divergent energy Δ should only occur on timescales $\tau \sim \exp(\beta\Delta)$, which is called the Arrhenius law. Any string-like logical operator will have a bounded energy barrier because, once the endpoints of the string are well-separated, each endpoint becomes a point-like excitation with constant energy. Thus, the search for models with unbounded energy barriers reduces to a search for models free from string-like logical operators.

In fact, while it is possible to construct 3d systems where all energy barriers are unbounded [45, 85], even these systems do not perform self-correction [122]. As in the 2d toric code, the problem

can be traced to the existence of topologically-charged point-like excitations [102]. At nonzero temperature, these excitations exist at finite density. Then, on a very heuristic level, the bath only needs to transport each topological excitation a finite distance to its nearest neighbor. Since the timescale for these partial logical operators is finite, the bath can perform logical operations in a finite time.

The conclusion to draw here is that unbounded energy barriers are necessary but not sufficient for self-correction. On the other hand, local thermal baths cannot apply membrane-like operators in any finite time, in the thermodynamic limit below some critical temperature [25, 112], so we expect a memory wherein all logical operators are membrane-like will be self-correcting. As an example, the logical operators in the 4d toric code are all membrane-like.

Instead of looking for a quantum memory that is self-correcting under its own dynamics, we can imagine coupling a toric code to another system in such a way that the latter endows the former with long-range interactions, confining the anyons. For simplicity, assume the coupled system consists of bosons. The 2d version of this proposal is the toric-boson model [47]. The toric-boson model requires couplings between anyons and bosons to have a divergent energy scale. Furthermore, the dynamics of the bosons must be fine-tuned so they do not develop a gap. The 3d version [100] drops the requirement of divergent energy scales, but still needs fine-tuned dynamics [75]. A further difficulty of the generalized toric-boson models is that the boson parts have infinite local Hilbert space dimensions, which is not as useful for quantum computing applications [15]. In Sec. 3.2.3 we will see how the Roberts-Bartlett model reproduces similar physics with finite local Hilbert space dimension.

3.2.2 Higher-form symmetries

Before getting to the Roberts-Bartlett model, let us define higher form symmetries. These generalized global symmetries compactly encode the dynamical constraints required for that model.

In the continuum, an ordinary global symmetry is a group of operators that act on the entire d -dimensional space of some theory. As a generalization of global symmetries, p -form symmetries

act on closed, $(d - p)$ -dimensional submanifolds of space [33, 73]. In this classification, ordinary global symmetries can be called 0-form symmetries. Unlike gauge symmetries, which are just redundancies in some description of a theory, higher-form global symmetries are physical symmetries that transform between distinct states. They can give rise to symmetry-protected topological phases [33] and symmetry-broken phases [33, 73, 136], like ordinary global symmetries.

On a lattice, the definition of the higher-form symmetry needs to be clarified. The proper way to do this is in the language of cellular homology [107]. We will instead proceed by example.

It is easy to find higher-form symmetries in topological phases. In fact, spontaneous breaking of higher-form symmetries leads to topological order [33, 136]. As an example, the 2d toric code with no perturbations has an X -type and a Z -type 1-form symmetry, partially generated by the vertex and face terms, respectively.

An arbitrary product of face terms $B_f = \prod_{e \in f} Z_e$ for some set F of faces gives a symmetry operator $W_C = \prod_{e \in C} Z_e$.¹ The path $C = \partial F$ is a (possibly disconnected) closed path on the lattice. It is closed in the sense that it does not have any endpoints. Since C is the boundary of a collection of faces, these symmetry operators are topologically trivial, meaning they do not wrap around the system. We will call these operators the local part of the symmetry, even though the operators may be large.

There are also topologically nontrivial symmetry operators that do wrap around the system. These are the logical operators in the toric code, which are also closed. We will say they are the topological part of the symmetry. Both types of operators act on $(1 = d - 1)$ -dimensional paths, so they jointly generate the Z -type 1-form symmetry. A similar story exists for the X -type 1-form symmetry, with symmetry operators $T_{C'} = \prod_{e \in C'} X_e$ where C' is a path on the dual lattice.

In the 3d toric code with qubits on edges [19], the terms $B_f = \prod_{e \in f} Z_e$ still act on the four edges around a face, while the terms $A_v = \prod_{e \in \partial^\dagger v} X_e$ now act on the six edges around a vertex. The face terms still generate 1-dimensional symmetry lines. This means that they are part of a 2-form

¹The notation is meant to reflect that this operator becomes a Wilson operator if we interpret the toric code as a model for a \mathbb{Z}_2 gauge theory.

symmetry now. The vertex terms generate membrane-type operators, which are 2-dimensional objects and therefore part of the 1-form symmetry. These membranes are closed in the sense that they do not have any boundaries.

The higher-form symmetries just described are different than the continuum higher-form symmetries usually considered in the high energy literature [107, 118]. To understand the difference, recall that the toric code is a model for \mathbb{Z}_2 gauge theory. If we were really studying gauge theory, we would identify any states related by a gauge transformation as the same physical state. In the toric code, this means requiring that $A_v = 1$ hold as an operator equation for all v . Thus, the entire local part of the X -type 1-form symmetry acts trivially on the physical Hilbert space. Only the topological part of the X -type 1-form symmetry acts nontrivially. Furthermore, any two operators that are topologically equivalent (in the same homology class) are equivalent as operators on the physical Hilbert space.

The two ways of defining higher-form symmetries are called faithful and topological, respectively [107]. Faithful higher-form symmetries are more natural in lattice models when we do not want to restrict the Hilbert space, and in non-relativistic models. Topological higher-form symmetries are more natural in gauge theories and relativistic theories [118]. In this paper we will discuss faithful higher-form symmetries in order to preserve the tensor-product structure of the global Hilbert space.

When we say that we will enforce a symmetry, we mean that we require that the operators S_α that appear in (3.2) must commute with the generators of the symmetry. Any local operator that fails to commute with a topological generator also fails to commute with a local generator, so it is enough to require that all the S_α commute with the local part of the symmetry.

3.2.3 Self-correction with a 1-form symmetry

Now that we have defined higher-form symmetries, we can ask the following question: “Is it possible to construct a self-correcting quantum memory if we allow ourselves to enforce a 1-form symmetry?” At first, this might seem like an interesting question. Ordinary (0-form) SPT phases are not stable at finite temperature because thermal effects can violate the symmetry locally. On

the other hand, 1-form symmetry-protected phases are stable at nonzero temperature, essentially because the symmetry imposes stronger constraints [114].

We can quickly see that the answer is trivially “yes”. As an example, take the 2d toric code and require that the dynamics respect all vertex and face terms. In that case, the only allowed operators are products of stabilizers or complete logical operators. If we restrict our bath to only be able to apply operators of bounded size, the bath cannot apply any logical operators. Previously, we could have said that the 1-form symmetries were enforced energetically, in the sense that anyons (which break the symmetry) were suppressed by the gap. Now, we can say the symmetry is enforced explicitly rather than energetically.

Similarly, we can consider the 3d toric code with the vertex terms (which generate a 1-form symmetry) enforced, but not the face terms (which would generate a 2-form symmetry). Once again, the string logical operators can not be applied transversally. The interesting difference is that while the membrane operators can be applied transversally without breaking the symmetry, the memory time still grows without bound. This is because of the previous argument that thermal baths cannot apply membrane operators in the thermodynamic limit [19, 25].

A more interesting question to ask is: “Is it possible to construct a self-correcting quantum memory that permits the transversal application of logical Pauli operators, if we allow ourselves to enforce a 1-form symmetry?” Neither the 2d or 3d toric codes with 1-form symmetry enforced answer this question. Instead, the Roberts-Bartlett model shows that the answer is “yes” [112], constructing a model that consists of the 3d cluster state Hamiltonian of Raussendorf, Bravyi, and Harrington (RBH) [110], with 2d toric code boundary conditions. When the 1-form symmetry is enforced in the bulk, the boundary logical degrees of freedom do not evolve in time, even at nonzero temperature.

We should note that the Roberts-Bartlett model does not allow for the transversal application of arbitrary (non-Pauli) logical operators. In fact, the same is true of the 4d toric code (which is self-correcting at $T > 0$ without any enforced symmetry). There is a model that supports arbitrary transversal logical operations in 7 spatial dimensions, but no such model in fewer dimensions is

known [9].

The explicit construction of the Roberts-Bartlett model is rather involved, so we leave the details to the original literature [112]. Here, we will only review the models at the effective level. The RBH Hamiltonian is not topologically ordered, but is SPT-ordered under a 1-form symmetry [114]. Furthermore, this SPT order is stable at nonzero temperatures. Ordinary (0-form) SPT order does not survive to nonzero temperatures [114].

The logical information in the Roberts-Barlett model resides on the boundary toric code qubits. As always, anyons live at the ends of partial logical operators. In the Roberts-Bartlett model, the anyons are connected to extended excitations (flux strings) that extend into the bulk and have linear energy cost. The 1-form symmetry then ensures that these bulk flux strings cannot end, except on another anyon on the boundary. [112].

Once the anyons are connected to the bulk flux, they are confined, and cannot traverse the system through thermal effects. In 2d, confinement ruins topological order because if the anyons leave energetic flux behind, then the full operator cannot be a logical operator (because it does not commute with the Hamiltonian). Instead, the Roberts-Bartlett model uses the third space dimension to remove the energetic flux. Although specific details of this procedure depend on the explicit construction, Fig. 3.1 shows the removal on the effective level.

Reference [112] also shows that once the anyons are confined by flux strings with linear energy cost, the memory time of the model will grow without bound in the thermodynamic limit. This is different from fracton models, where a diverging (but sub-linear) energy barrier does not lead to a diverging memory time [122].

The Roberts-Bartlett construction can be extended to any Walker-Wang model [66, 133]. In fact, the RBH Hamiltonian (the bulk of the Roberts-Bartlett model) is equivalent to the Walker-Wang model with the toric code braided fusion category as input, after moving some qubits to faces [113]. Furthermore, the Roberts-Bartlett construction can be extended to a model with a trivial bulk, [125] at the cost of enforcing a 1-form symmetry with an action at the boundary that is not on-site [136].

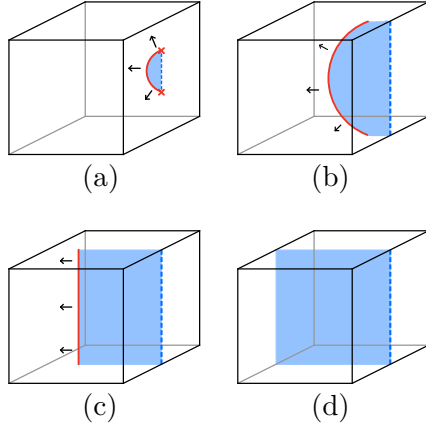


Figure 3.1: Decomposition of a logical operator. The top and bottom of the cube are identified and the front and back of the cube are identified. In the RBH model and in the symmetry-protected boundary memory introduced in this paper, anyons on the boundary are attached to flux in the bulk. Red crosses represent anyons, red lines are bulk flux, and blue lines are logical operators on the boundary. The blue shaded region is a membrane operator, which is necessary for the symmetry-protected boundary memory but not for the RBH model. Compare to Fig. 12 of [112] and Fig. 7 of [125].

We can gain a new perspective on the Roberts-Bartlett model by examining the precise role of the 1-form symmetry in protecting the memory. As emphasized in Ref. [112], the 1-form symmetry in the bulk prevents the flux-like excitations from ending. On the boundary, the 1-form symmetry requires that any boundary anyons live on the endpoints of bulk fluxes. Both roles are essential in this family of models. If boundary anyons did not need to be attached to bulk excitations, they would be deconfined. If the bulk fluxes were allowed to end, then boundary anyons could be attached to finite-length bulk fluxes, again leading to deconfinement.

Reference [112] already pointed out that topologically-ordered models like the 3d toric code can have an emergent 1-form symmetry, so that there are loop excitations that cannot end in the bulk. The contribution of the current paper is to demonstrate that we can use this emergent symmetry to replace the enforced symmetry in the bulk. However, we have not found a way for the emergent symmetry to attach the anyons to the bulk flux. Instead, we will need to enforce a 1-form symmetry on the boundary. This means that we can achieve self-correction while enforcing an $\mathcal{O}(L^2)$ number of stabilizers, rather than an $\mathcal{O}(L^3)$ number.

3.3 Restricting to a boundary symmetry

In this section we will introduce our new model that uses an emergent 1-form symmetry in the bulk rather than directly enforcing a bulk symmetry. As the model consists of a memory on a boundary protected by a symmetry, we will call it the symmetry-protected boundary memory. We will first define the Hamiltonian and then describe the logical operators. We will then explain why a subspace of the logical codespace forms a memory that is stable at finite temperature.

3.3.1 Hamiltonian and logical operators

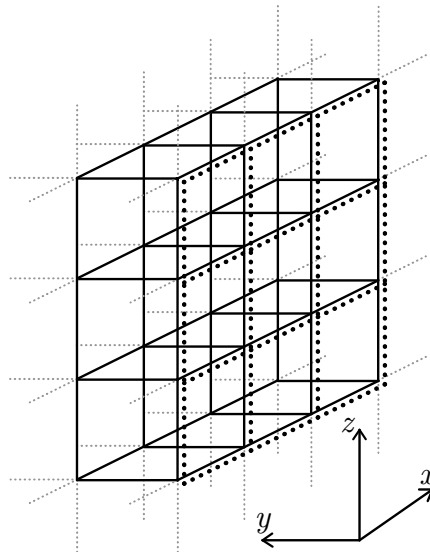


Figure 3.2: We can view the Hilbert space of the model as living on a cubic lattice. In the bulk, qubits live on faces and edges. The boundary faces have no qubits. The boundary edges have two qubits each, one of which is a bulk (e) degree of freedom (solid line) and one of which is a boundary (b) degree of freedom (dotted line). The lattice is periodic in the x and z directions and has boundaries at $y = 0$ and $y = L$. This figure shows the “right” boundary at $y = 0$, where we will put our 2d toric code. The boundary at $y = L$ is gapped with no additional topological order.

In the absence of the symmetry, the symmetry-protected boundary memory is a tensor product of two 3d toric codes with a 2d toric code on their boundary. It lives on a cubic lattice with boundary. The Hilbert space is as in Fig. 3.2, with qubits on edges and faces and a second qubit on each boundary edge. Thus, we have enough qubits to define two copies of the 3d toric code and one copy

of the 2d toric code. The full Hamiltonian will be

$$H = H^{(e)} + H^{(f)} + H^{(b)}, \quad (3.3)$$

with each term defined below. We will use a lattice that is periodic in the z and x directions, so that the global structure is a thickened torus, $T^2 \times I$. There are two boundaries, each a 2d torus, with the 2d toric code on the $y = 0$ boundary as shown in Fig. 3.2. The other boundary (at $y = L$) will have similar boundary conditions on the (e) and (f) qubits, but without the extra boundary degrees of freedom.

The first term in H ,

$$H^{(e)} = - \sum_v A_v^{(e)} - \sum_f B_f^{(e)}, \quad (3.4)$$

is a bulk 3d toric code Hamiltonian acting on edge degrees of freedom. The individual stabilizers,

$$A_v^{(e)} = \prod_{e \in \partial^\dagger v} X_e^{(e)}, \quad B_f^{(e)} = \prod_{e \in \partial f} Z_e^{(e)} \quad (3.5)$$

are shown in Fig. 3.3. The logical operators in this sector are direct lines of $Z^{(e)}$ operators and dual membranes² of $X^{(e)}$ operators. At endpoints of $Z^{(e)}$ lines we have $e^{(e)}$ anyons and on the boundaries of $X^{(e)}$ membranes we have $m^{(e)}$ flux. The boundary conditions at $\pm y$ are “smooth”, so that the $m^{(e)}$ flux is condensed (meaning the flux can be removed at the boundary) and $e^{(e)}$ anyons are confined. Equivalently, $X^{(e)}$ membranes can terminate on the boundaries but $Z^{(e)}$ lines cannot.

The other bulk Hamiltonian is

$$H^{(f)} = - \sum_c A_c^{(f)} - \sum_e B_e^{(f)}, \quad (3.6)$$

²A dual membrane is a membrane on the dual lattice. The dual lattice is the result of exchanging vertices with cubes and interchanging edges with faces.

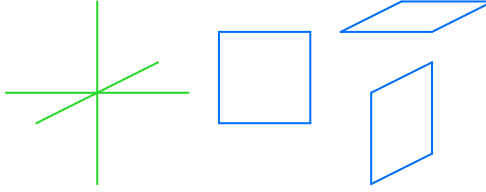


Figure 3.3: Stabilizers for the 3d toric code on edges. Green edges are $X^{(e)}$ operators and blue edges are $Z^{(e)}$ operators.

which acts on face qubits. The terms are

$$A_c^{(f)} = \prod_{f \in \partial c} Z_f^{(f)}, \quad B_e^{(f)} = \prod_{f \in \partial^{\dagger} e} Z_f^{(f)}, \quad (3.7)$$

as shown in Fig. 3.4. They are equivalent to the edge terms after swapping edges with faces, swapping cubes with vertices, and swapping X with Z . The logical operators in this sector are dual lines of $X^{(f)}$ operators and direct membranes of $Z^{(f)}$ operators. Here, the excitations are point-like $m^{(f)}$ anyons on the ends of $X^{(f)}$ dual lines and extended $e^{(f)}$ flux at the boundaries of $Z^{(f)}$ membranes. Note that we are using a convention for the (f) degrees of freedom where the electric excitations are extended and the magnetic excitations are point-like. The boundary conditions are such that the $m^{(f)}$ flux is condensed, which is now called the “rough” boundary conditions.

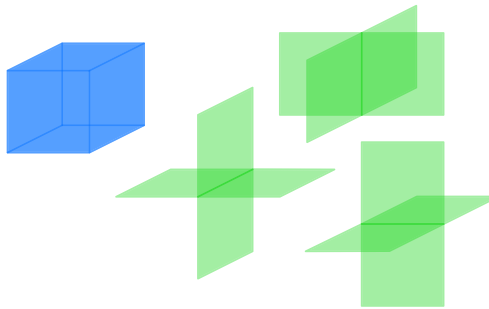


Figure 3.4: Stabilizers for the 3d toric code on faces. Green faces are $X^{(f)}$ operators and blue faces are $Z^{(f)}$ operators.

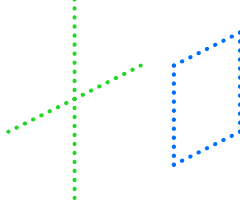


Figure 3.5: Stabilizers for the 2d toric code on the boundary. Green dotted lines are $X^{(b)}$ operators and blue dotted lines are $Z^{(b)}$ operators.

On the extra set of boundary qubits we will define a 2d toric code,

$$\begin{aligned} H^{(b)} &= - \sum_v A_v^{(b)} - \sum_f B_f^{(b)}, \\ A_v^{(b)} &= \prod_{e \in \partial v} X_e^{(b)}, \quad B_f^{(b)} = \prod_{e \in \partial f} Z_e^{(b)}, \end{aligned} \tag{3.8}$$

where the sums and products are only taken over boundary faces, edges, and vertices. These terms are shown in Fig. 3.5. Here, the logical operators are direct lines of $Z^{(b)}$ and dual lines of $X^{(b)}$. The excitations are $e^{(b)}$ anyons and $m^{(b)}$ anyons.

For simplicity let us only describe a subset of the logical qubits, and therefore a subset of the logical operators. Let $\bar{Z}^{(e)}$ correspond to a vertical line of $Z^{(e)}$ operators in the bulk and $\bar{X}^{(e)}$ to a horizontal dual membrane of $X^{(e)}$ operators (which must intersect both boundaries). For the face code let $\bar{Z}^{(f)}$ be a vertical membrane of $Z^{(f)}$ operators and $\bar{X}^{(f)}$ a horizontal dual line through the bulk of $X^{(f)}$ operators. On the boundary we have $\bar{Z}^{(b)}$ a vertical line of $Z^{(b)}$ operators and $\bar{X}^{(b)}$ a horizontal dual line of $X^{(b)}$ operators. There are another 3 logical qubits whose logical operators are related by a global rotation, but we can safely ignore these as their description is the same.

All three of these qubits are fault tolerant. This corresponds to the existence of topological order at $T = 0$ [70]. At nonzero temperature, a local thermal bath can apply the operators $\bar{Z}^{(e)}$, $\bar{X}^{(f)}$, $\bar{Z}^{(b)}$, and $\bar{X}^{(b)}$, essentially because they have a constant energy barrier. Thus the edge and face logical qubits can serve as classical, but not quantum, memories [19], while the boundary logical qubit can store no information.

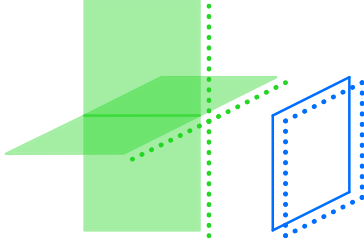


Figure 3.6: The terms we enforce are $\mathcal{A}_v = A_v^{(b)} A_{e^{(0)}}^{(f)}$ (left) and $\mathcal{B}_f = B_f^{(e)} B_f^{(b)}$ (right). Since the symmetry operators are products of stabilizers, the ground space is not affected. Instead, some excitations are forbidden, so that boundary logical operators can only be applied in tandem with bulk membrane operators.

3.3.2 Enforcing the symmetry

The last ingredient is the 1-form symmetry that we will choose to enforce. The symmetry acts on the boundary, in the sense that it acts only on (b) qubits, and those (e) and (f) qubits that are adjacent to the boundary. For v a boundary vertex and f a boundary face, the generators of the local part of the symmetry,

$$\mathcal{A}_v = A_v^{(b)} A_{e^{(0)}}^{(f)}, \quad \mathcal{B}_f = B_f^{(b)} B_f^{(e)}, \quad (3.9)$$

are products of stabilizers in Hamiltonians. The edge $e^{(0)}$ is the unique non-boundary edge such that $v \in \partial e^{(0)}$. The terms are illustrated in Fig. 3.6. The generators of the topological part of the symmetry are products of logical operators, such as $\bar{Z}^{(e)} \bar{Z}^{(b)}$. The local and topological generators locally look the same.

When the symmetry is enforced, $e^{(b)}$ anyons are required to coincide with endpoints of $e^{(f)}$ flux and $m^{(b)}$ anyons are required to coincide with endpoints of $m^{(e)}$ flux, all of which occur only on the lattice boundary. This means that the operators $\bar{Z}^{(b)}$, $\bar{Z}^{(f)}$, $\bar{X}^{(b)}$, and $\bar{X}^{(e)}$ all can no longer be applied transversally. For the boundary operators this is because the boundary anyons are prohibited. This is demonstrated for $\bar{Z}^{(e)}$ in Fig. 3.7. For the two membrane operators, open membranes (incomplete logical operators) are permitted in the bulk but are not allowed to intersect the boundary. The bulk line operators $\bar{Z}^{(e)}$ and $\bar{X}^{(f)}$ can still be applied transversally because they

need not intersect the boundary.

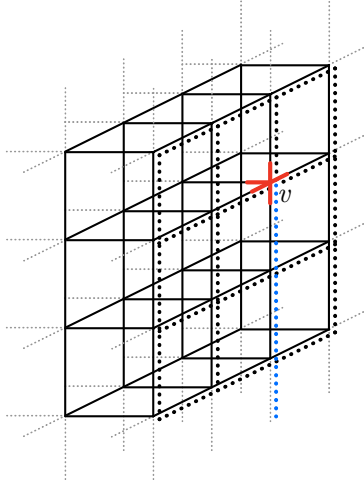


Figure 3.7: Blue dotted lines represent $Z^{(e)}$ operators, a partial application of the logical operator $\bar{Z}^{(e)}$. At the highlighted vertex, the partial logical operator anticommutes with $A_v^{(b)}$ and \mathcal{A}_v . Anticommutation with $A_v^{(b)}$ only leads to an energy penalty, but anticommutation with \mathcal{A}_v means that this operator is forbidden by the 1-form symmetry. A similar argument applies to any partial $\bar{Z}^{(e)}$ operator.

The only way to transversally act on the boundary logical qubit is through the composite logical operators $\bar{X}^{(e)}\bar{X}^{(b)}$ and $\bar{Z}^{(f)}\bar{Z}^{(b)}$. Figure 3.8 demonstrates the partial application of $\bar{Z}^{(f)}\bar{Z}^{(b)}$. Since both composite operators include a membrane part, the composite operators are linearly confined. The upshot is that all logical operators that can transversally act on the boundary logical qubit are linearly confined. We should note that while we need the bulk topological order to supply the bulk flux, we do not store any information in the bulk.

Since both boundary logical operators are linearly confined, a local bath cannot apply them in finite time in the thermodynamic limit [112]. This means that the current model achieves the same memory properties as the Roberts-Bartlett model, while only requiring that a symmetry be enforced at the boundary. No symmetry terms need to be enforced in the bulk.

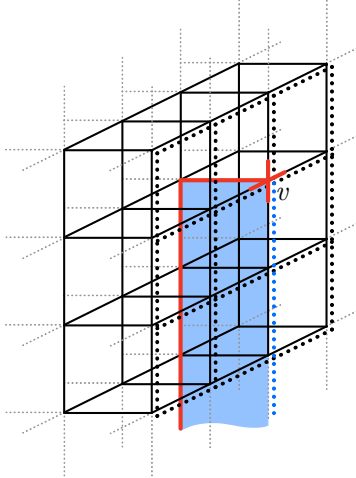


Figure 3.8: Blue dotted lines represent $Z^{(e)}$ operators and blue faces are $Z^{(f)}$ operators. This operator anticommutes with $A_v^{(b)}$ at the highlighted vertex and $B_e^{(f)}$ at every highlighted edge, which leads to a large energy penalty. The addition of the $Z^{(f)}$ operators means it now commutes with A_v , so it is a permitted operator. We should view this as a partial application of the composite logical operator $\bar{Z}^{(f)}\bar{Z}^{(b)}$.

3.4 Interpretation

We can gain some insight into the behavior of this model by analyzing it on the effective level, instead of focusing on the specific lattice realization. There, the simplest language to use is that of defects in 3d topological orders. So far, we have been orienting the model so that the 2d toric code sits on the boundary of the system. Since the edge and face bulk degrees of freedom are noninteracting, we can alternatively unfold [69] the two bulks and view the 2d toric code as a boundary or *defect* between two spatially separated 3d toric codes. Reference [1] explains defects in depth, furthermore using networks of defects (and defects of defects, etc.) to construct fracton phases. Here, we will only need to discuss 2d defects in 3d topological orders.

We will describe defects as the result of a process in which we confine and condense composite objects at a 2d surface in a 3d topological order. Condensation of composite objects can be useful in constructing many models, including Michnicki's welded code [85, 122] and fractons [82, 107, 131]. When a condensed composite $a_1 \dots a_n$ has nontrivial mutual statistics with another anyon a' , the anyon a' becomes confined. Similarly, when the same composite is condensed on a boundary, a'

becomes confined on that boundary, meaning it cannot be annihilated at and cannot pass through that boundary.

Let us say that a flux string is deconfined on a certain boundary if it can end on that boundary, and confined if it can not. Under this definition, in the 3d toric code (defined on edges), flux strings are confined at the rough boundary and deconfined at the smooth boundary. Furthermore, the e anyons are confined at the smooth boundary and condensed on the rough boundary. If we take a smooth boundary and condense e anyons, the flux strings become confined and we end up with a rough boundary. This generalizes the previous notion of condensation leading to confinement. If we start with a rough boundary and condense m flux near the boundary, the e anyons become confined on that boundary.

Now recall from Sec. 3.2.3 that a 2d toric code with both 1-form symmetries enforced is trivially self-correcting because it has no dynamics. We can view enforcing the 1-form symmetry as confining the m and e anyons “by hand,” or without any condensation procedure.

We can also construct the symmetry-protected boundary memory using by-hand confinement. As in Fig. 3.9, we have a 3d toric code labeled by (e) , a 2d toric code in the center labeled by (b) , and another 3d toric code on the left labeled by (f) . The labels are chosen to match the labels in Sec. 3.3, but we no longer need to refer to edges and faces. On the boundary, we confine the $e^{(b)}$ and $m^{(b)}$ anyons and the $m^{(e)}$ and $e^{(f)}$ fluxes, in such a way that the composite objects $m^{(e)}m^{(b)}$ and $e^{(b)}e^{(f)}$ are deconfined. When we say that a composite of a boundary anyon and a bulk flux are deconfined, we mean that the flux may end on the boundary, but only if its endpoint coincides with the corresponding anyon. Similarly, the boundary anyons my move freely only when attached to bulk flux.

The bulk fluxes give the boundary anyons dynamics, so the anyons are (linearly) energetically confined, instead of exactly confined like in the trivial 2d toric code example. As in Sec. 3.3, the boundary anyon confinement means that the bath cannot apply logical operators, even though the operators can be transversally applied. Just like in Sec. 3.3, though, these boundary conditions need the presence of the 1-form symmetry in order to be stable to perturbations. We can view this as

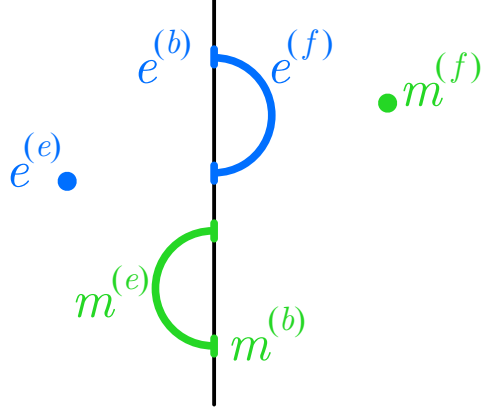


Figure 3.9: The setup for the symmetry-protected boundary memory has $e^{(e)}$ and $m^{(f)}$ anyons and $m^{(e)}$ and $e^{(f)}$ flux in the two bulks, and $e^{(b)}$ and $m^{(b)}$ anyons on the defect. For the microscopic realization in Sec. 3.3, the green excitations are created from Z -type errors while the blue excitations are created from X -type errors. The confinement procedure ensures that $e^{(b)}$ anyons coincide with endpoints of $e^{(f)}$ flux and $m^{(b)}$ anyons coincide with endpoints of $m^{(e)}$ flux.

saying that by-hand confinement without condensation is fine-tuned.

Note that, for example, the confinement of $m^{(e)}$ and $m^{(b)}$ but not $m^{(e)}m^{(b)}$ is the confinement pattern that would result from condensing the composite $e^{(e)}e^{(b)}$. In fact, we can follow that condensation procedure on the microscopic lattice by considering the Hamiltonian (3.3) as a perturbation to the condensing Hamiltonian

$$H_{\text{cond}} = -J_x \sum_e X_e^{(e)} X_e^{(b)}, \quad (3.10)$$

where the sum is taken over boundary edges, in the large J_x limit. Then we get the symmetry term \mathcal{B}_f in (3.9) at some order in perturbation theory, which confines $m^{(e)}$ and $m^{(b)}$ but not $m^{(e)}m^{(b)}$. Unfortunately, fully building the symmetry-protected boundary memory from condensation would also require condensing $m^{(b)}m^{(f)}$, which is not possible because condensed composites cannot have mutual statistics.

Before concluding, let us briefly mention an interesting related model, which can be constructed from a 2d \mathbb{Z}_4 topologically-ordered defect in a 3d \mathbb{Z}_2 topologically-ordered bulk. The boundary topological order contains anyons $e^{(b)}$, $e^{2(b)}$, $e^{3(b)}$, $m^{(b)}$, $m^{2(b)}$, and $m^{3(b)}$, along with their products.

All are abelian, and the $e^{(b)}$ and $m^{(b)}$ anyons have mutual statistics i . The bulks are as before.

On the defect, condense the composite objects $e^{(e)}e^{2(b)}$ and $m^{2(b)}m^{(f)}$. This condensation is consistent because $e^{2(b)}$ and $m^{2(b)}$ have trivial mutual statistics. The procedure also removes all topological order from the defect. The anyons $e^{2(b)}$ and $m^{2(b)}$ are still deconfined, but are respectively equivalent to the $e^{(e)}$ and $m^{(f)}$ bulk anyons. Furthermore, the $m^{(e)}$ flux string is allowed to terminate on the boundary, but only in the presence of a $m^{(b)}$ anyon which is otherwise confined. A similar story exists for the $e^{(f)}$ flux and $e^{(b)}$ anyon.

The resulting model is stable to any small perturbation and does not require any symmetry-protection. We can construct a microscopic model, as in Sec. 3.3, by putting qubits on bulk edges and faces, and 4-level qudits on boundary edges. The 4-level qudits have Pauli-like operators obeying

$$X_e^{(b)}Z_e^{(b)} = iZ_e^{(b)}X_e^{(b)}, \quad (X_e^{(b)})^4 = (Z_e^{(b)})^4 = 1, \quad (3.11)$$

while the bulk face and edge qubits have ordinary 2-level Pauli operators. The Hamiltonian consists of the ordinary bulk toric code Hamiltonian, with the boundary Hamiltonian

$$\begin{aligned} H_{\text{bdy}} &= -\sum_v \mathcal{A}_v - \sum_f \mathcal{B}_f - \sum_v A_v^{(b)} - \sum_f B_f^{(b)} + \text{h.c.}, \\ \mathcal{A}_v &= \prod_{e \in \partial^\dagger v} X_e^{(b)} X_{f^{(0)}}^{(f)}, \quad \mathcal{B}_f = \prod_{e \in \partial f} Z_e^{(b)} Z_e^{(e)}, \\ A_v^{(b)} &= \prod_{e \in \partial^\dagger v} (X_e^{(b)})^2, \quad B_f^{(b)} = \prod_{e \in \partial f} (Z_e^{(b)})^2, \end{aligned} \quad (3.12)$$

where $f^{(0)}$ is the unique non-boundary face in $\partial^\dagger e$ and, analogous to in Ref. [70], each edge and plaquette must be assigned an orientation. The sums are over boundary vertices and faces, and the second two terms are just the squares of the first two terms. The terms are shown in Fig. 3.10 using the “folded” conventions from Sec. 3.3.

This \mathbb{Z}_4 defect model is not self-correcting. At nonzero temperature it can only store a number of probabilistic bits, just like decoupled 3d toric codes [19]. Instead, it is interesting because

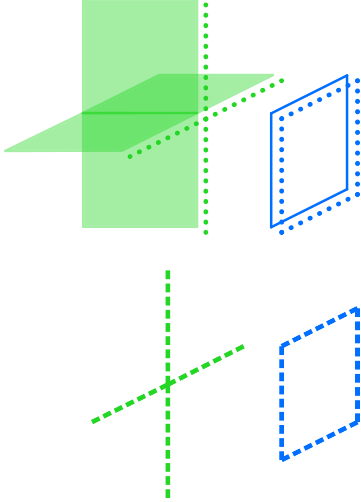


Figure 3.10: The boundary Hamiltonian terms in (3.12). The top row shows \mathcal{A}_v and \mathcal{B}_f , where green faces are $X^{(f)}$, green dotted lines are $X^{(b)}$, blue solid lines are $Z^{(e)}$, and blue dotted lines are $Z^{(b)}$. The bottom row shows $\mathcal{A}_v^{(b)}$ and $\mathcal{B}_f^{(b)}$, where green dashed lines are now $(X_e^{(b)})^2$ and blue dashed lines are $(Z_e^{(b)})^2$. The top two terms square to the bottom two, respectively.

membrane operators in the two bulks fail to commute, due to the fact that the bulk fluxes must terminate in anyons on the defect and the respective anyons have nontrivial mutual statistics. The presence of membrane operators that fail to commute seems to be a necessary (although clearly not sufficient) ingredient for self-correction [25, 112]. The \mathbb{Z}_4 defect model appears to be the first model in three or fewer dimensions with this property.

3.5 Conclusions

The symmetry-protected boundary memory is useful in two ways. First, it improves upon the Roberts-Bartlett model by only requiring that $\mathcal{O}(L^2)$ symmetry generators be enforced, rather than $\mathcal{O}(L^3)$. In that sense it is a continuation of the work in Ref. [125], which showed that self-correction is possible with a number of enforced terms that is asymptotically smaller than L^3 but greater than L^2 .

The second contribution of the present model is to emphasize that, in the Roberts-Bartlett model, the 1-form symmetry serves two distinct purposes. Namely, it ensures that the flux strings

do not end in the bulk *and* requires that boundary anyons and flux string endpoints coincide. Here, we show that the first contribution can be supplied by bulk topological order. Even at nonzero temperature, the flux strings of the 3d toric code cannot end. This is connected to the fact that discrete 1-form symmetries can be spontaneously broken (and therefore emergent [136]) at non-zero temperature in 3d.

On the other hand, we have not yet found a way to require that boundary anyons and flux string endpoints coincide without explicitly enforcing the 1-form symmetry at the boundary. Finding a way to make this requirement emergent, rather than explicit, would certainly be exciting.

It might also be interesting to extend the constructions in this paper to more general boundaries and bulks. For example, generalizations of the symmetry-protected boundary memory should be able to realize more general G -crossed braided tensor categories [5]. Relatives of the \mathbb{Z}_4 defect model could have more interesting string-nets on the boundary, and other exotic phases in the bulk.

Finally, the finite-temperature behavior of topological defects may warrant further exploration. It may be the case that they have no memory properties beyond those of the topologically-ordered bulks, but the existence of noncommuting membrane operators in 3d seems intriguing.

Chapter 4

Single-shot quantum memory

We construct a new subsystem code in three dimensions that exhibits single-shot error correction in a user-friendly and transparent way. As this code is a subsystem version of coupled toric codes, we call it the intertwined toric code (ITC). Although previous codes share the property of single-shot error correction, the ITC is distinguished by its physically motivated origin, geometrically straightforward logical operators and errors, and a simple phase diagram. The code arises from 3d stabilizer toric codes in a way that emphasizes the physical origin of the single-shot property. In particular, starting with two copies of the 3d toric code, we add check operators that provide for the confinement of pointlike excitations without condensing the loop excitations. Geometrically, the bare and dressed logical operators in the ITC derive from logical operators in the underlying toric codes, creating a clear relationship between errors and measurement outcomes. The syndromes of the ITC resemble the syndromes of the single-shot code by Kubica and Vasmer, allowing us to use their decoding schemes. We also extract the phase diagram corresponding to ITC and show that it contains the phases found in the Kubica-Vasmer code. Finally, we suggest various connections to Walker-Wang models and measurement-based quantum computation.

4.1 Introduction

Single-shot quantum error-correcting codes provide for a streamlined error-correction protocol, in which a single round of imperfect measurements suffices to correct errors [11]. The two-dimensional (2d) toric code [70] does not realize this property because the pointlike excitations cannot be reliably

located in a single round of faulty measurements [25]. On the other hand, the excitations in the 4d toric code are all extended excitations, allowing for single-shot error correction [25]. The toric codes are all stabilizer codes, meaning that all operators in the code commute. In stabilizer codes, single-shot error correction is closely related to self correction, suggesting that any single-shot stabilizer code is, in fact, self-correcting. No single-shot stabilizer codes have been found below 4d.

On the other hand, single-shot *subsystem* codes do exist in 3d. Subsystem codes generalize stabilizer codes by having a check group, which does not commute, and a stabilizer group, which does commute. The gauge color code (GCC) [10] was the first 3d subsystem code shown to be single-shot [11]. Despite the code's remarkable properties, its complicated construction meant that no other examples were found until seven years later, by Kubica and Vasmer [71]. Even in the Kubica-Vasmer code (KVC), the essential physical properties that provide for the success of single-shot error correction remain elusive.

Here, we construct a new single-shot quantum error-correcting code in three dimensions, which we call the intertwined toric code (ITC). This new code displays three main advantages: a transparent physical motivation and interpretation, geometrically simple logical operators, and a straightforward derivation of its phase diagram. Physically, the ITC draws inspiration from the 3d toric code. Its check group consists of the toric code operators supplemented by single-site check operators. As a result, the ITC stabilizers detect the pointlike excitations and the check operators detect the operators that make those excitations, depicted graphically in Fig. 4.1a. This clarifies that, physically, the ITC confines the pointlike excitations without condensing the extended excitations—which is not possible in stabilizer codes.

Measuring a different set of generators in the check group leads to check syndromes reminiscent of the KVC. In particular, the effective pictures of the syndromes in this second basis of the ITC contain two flavors of violated stabilizers connected by four flavors of check operators (whereas the GCC has eight stabilizers and 24 check operators). We illustrate one sector of this presentation of the ITC in Fig. 4.1b. In this setting, the advantage of the ITC is the geometric simplicity of its logical operators: Membrane operators are defined on membranes and dual membranes on the

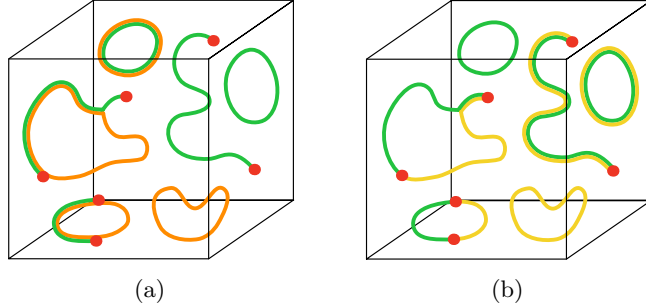


Figure 4.1: Characteristic measurement outcomes in the ITC. (a) In the underlying toric code, green lines are truncated stringlike logical operators and orange lines are extended excitations. In the ITC, these objects are put on equal footing as lines of violated check operators as in (4.7). In both the toric code and the ITC, the red dots are violated stabilizers. (b) With the alternative basis of check operators in (4.20), measurement outcomes consist of two colors of extended objects. These cannot end except on violated stabilizers, which must be the simultaneous endpoints of one line of each color.

lattice, and stringlike operators are defined on paths and dual paths on the lattice. Furthermore, it is easy to find a partial logical operator that creates any given measurement outcome, as described at the end of Sec. 4.3.1.

Readers with a background in condensed matter may view subsystem codes as corresponding to families of Hamiltonians, with multiple gapped phases of matter separated by phase transitions. Such analyses exist for the GCC [72] and the KVC [77]. The ITC phase diagram is particularly easy to extract, and we find all of the phases of the KVC along with one additional phase. This relationship is characteristic of two subsystem codes related by the procedure of gauge fixing, suggesting that the KVC may be a gauge-fixed version of the ITC.

As an aside, the subsystem code literature uses the term “gauge operator” and “gauge group” instead of “check operator” and “check group.” To avoid confusion with the condensed-matter literature, where error-correcting codes often have interpretation in terms of gauge theories, we avoid using the word “gauge operator” herein. Instead, we refer to the relevant operators as “check operators” in the subsystem code, because one “checks” the value of these operators during the error-correction procedure [52].

The remainder of this paper is organized as follows. In Sec. 4.2 we intertwine two toric codes,

find a logical qubit, and describe the logical operators. We use a different set of check operators within the ITC in Sec. 4.3 to explore the possible measurement outcomes and outline the single-shot error correction procedure. In Sec. 4.4, we describe the phase diagram and explore connections of the various phases to previous literature. We conclude in Sec. 4.5 with some exploratory connections to other constructions and with a discussion of some open questions.

4.2 Intertwining toric codes

To provide readers with some background, we start with a brief review of subsystem codes in Sec. 4.2.1. Then, to define the ITC, we define the check group and stabilizer group on a cubic lattice with periodic boundary conditions in Sec. 4.2.2. Like the GCC and the KVC, the ITC does not encode any logical qubits on closed manifolds. To encode logical qubits we define boundary conditions in Sec. 6.3.2. The boundary conditions furnish the ITC with logical qubits, and we describe the logical operators on those qubits in Sec. 4.2.4.

4.2.1 Brief review of subsystem codes

Recall that a stabilizer code consists of a stabilizer group \mathcal{S} , which is a commuting subgroup of the Pauli group that does not contain the global phase operator $-\mathbb{1}$. Elements of \mathcal{S} are called stabilizers. A state is a code state if it satisfies all of the stabilizers, which means that it is a $+1$ eigenstate of those operators. Logical operators are elements of the centralizer of \mathcal{S} , $\mathcal{Z}(\mathcal{S})$, which is the group of all Pauli operators that commute with \mathcal{S} . These operators map code states to code states. Of course, every stabilizer is in $\mathcal{Z}(\mathcal{S})$, but these are trivial logical operators. The nontrivial logical operators are elements of $\mathcal{Z}(\mathcal{S})/\mathcal{S}$. Qubit errors are operators that do not commute with \mathcal{S} , and therefore take a code state out of the code space. A state not in the code space violates some stabilizers, meaning it is a -1 eigenstate of those stabilizers. A syndrome is the set of violated stabilizers in a given state, and an error causes a syndrome when it anticommutes with that set of stabilizers.

Subsystem codes [101] provide more flexibility than stabilizer codes by including a check

group \mathcal{G} in addition to a stabilizer group. The check group does not need to commute and may contain global phase operators. Heuristically, we think of the stabilizer group as the center of \mathcal{G} , which is $\mathcal{Z}(\mathcal{G}) \cap \mathcal{G}$, or the group made up of operators in \mathcal{G} that commute with all operators in \mathcal{G} . However, this may contain pure phases, so the stabilizer group of a subsystem code is

$$\mathcal{S} = (\mathcal{Z}(\mathcal{G}) \cap \mathcal{G})/i, \quad (4.1)$$

the center of \mathcal{G} with pure phases removed. Since $\mathcal{S} \subset \mathcal{G}$, each stabilizer is a product of check operators, allowing one to measure check operators in order to infer the value of stabilizers.

Code states cannot satisfy all of the check operators because \mathcal{G} does not commute. Instead, like in a stabilizer code, code states satisfy all of the stabilizers. Within the code space there are logical degrees of freedom (“logical qubits”) and other degrees of freedom (“check qubits”). The check operators act on the check qubits. Logical operators still must commute with all stabilizers, but come in two flavors depending on the degrees of freedom on which they act. Bare logical operators act only on the logical qubits while dressed logical operators act on the check qubits as well. Bare logical operators must commute with all check operators, making them elements of $\mathcal{Z}(\mathcal{G})$. Dressed logical operators need only commute with the stabilizers, making them elements of $\mathcal{Z}(\mathcal{S})$. Automatically, $\mathcal{G} \subset \mathcal{Z}(\mathcal{S})$ and $\mathcal{S} \subset \mathcal{Z}(\mathcal{G})$, so that the nontrivial bare and dressed logical operators are elements of $\mathcal{Z}(\mathcal{G})/\mathcal{S}$ and $\mathcal{Z}(\mathcal{S})/\mathcal{G}$, respectively.

The error-correction procedure consists of measuring the check operators, so the measurement outcome is the set of violated check operators. From a measurement outcome one can infer the stabilizer syndrome (the set of violated stabilizers). Code states have trivial stabilizer syndromes but still must have nontrivial measurement outcomes. An operator that anticommutes with some check operators changes the measurement outcome, while an operator that anticommutes with some stabilizers causes a syndrome. In this language, dressed logical operators create trivial stabilizer syndromes but change the measurement outcome, while bare logical operators create trivial stabilizer and do not change the measurement outcome.

Subsystem codes provide a number of advantages over stabilizer codes. As in this paper, subsystem codes may be single-shot in 3d, while no known examples of such stabilizer codes exist. Subsystem codes also allow for “gauge fixing” [101] a procedure we explore in Sec. 4.4. They may allow for measuring smaller operators; for example, the subsystem toric code in Ref. [13] has check operators that only act on three qubits. Some further information on subsystem codes may be found in Ref. [27], which studies anyon theories in 2d subsystem codes, and Ref. [10].

4.2.2 In the bulk

To define the ITC, start with two copies of the 3d *stabilizer* toric code, defined on a periodic cubic lattice. With qubits on edges e and faces f , define A operators

$$A_v = \prod_{e \in \partial^+ v} X_e = \begin{array}{c} \text{green} \\ \diagup \quad \diagdown \\ \text{green} \end{array}, \quad (4.2)$$

$$A_c = \prod_{f \in \partial c} Z_f = \begin{array}{c} \text{blue} \\ \text{cube} \end{array}, \quad (4.3)$$

for every vertex v and cube c . Green and blue denote X and Z operators, respectively, and solid lines and shaded squares represent operators on edge qubits and face qubits, respectively. In addition, define B operators

$$B_f = \prod_{e \in \partial f} Z_e = \begin{array}{c} \text{blue} \\ \text{shaded square} \end{array}, \quad (4.4)$$

$$B_e = \prod_{f \in \partial^+ e} X_f = \begin{array}{c} \text{green} \\ \text{shaded cross} \end{array}, \quad (4.5)$$

and rotations thereof. The operator ∂ is the boundary operator, so ∂f is the four edges around a face f and ∂c is the six faces around a cube c . The operator ∂^\dagger is the dual boundary, so $\partial^\dagger e$ is the four faces around an edge e and $\partial^\dagger v$ is the six edges around a vertex v . These operators are dual, meaning that, for example, $f \in \partial^\dagger e \leftrightarrow e \in \partial f$

The stabilizers A_v and B_f together define the ordinary presentation of the 3d toric code, while A_c and B_e are related to them by interchanging edges with faces, cubes with vertices, and X operators with Z operators. The stabilizer group

$$\mathcal{S}_{\text{2TC}} = \langle A_v, B_f, A_c, B_e \rangle, \quad (4.6)$$

which is the group generated by the terms inside the angled brackets, therefore defines two noninteracting 3d toric codes. Violations of the A stabilizers are isolated excitations, while violations of the B stabilizers must form closed strings. Thus, the excitations of this stabilizer code include two species of extended excitations and two species of pointlike excitations.

We now build the subsystem ITC from the stabilizer code \mathcal{S}_{2TC} by including the single-site operators X_e and Z_f on all edges and faces as check operators. The B_e and B_f operators anticommute with Z_f and X_e , respectively, and are themselves demoted to check operators. The resulting ITC check group

$$\mathcal{G}_{\text{ITC}} = \langle X_e, Z_f, B_e, B_f \rangle, \quad (4.7)$$

includes anticommuting operators, and therefore also contains $-\mathbb{1}$. The A operators still commute with all the check operators, so they define the stabilizer group

$$\mathcal{S}_{\text{ITC}} = \mathcal{Z}(\mathcal{G}_{\text{ITC}}) \cap \mathcal{G}_{\text{ITC}} = \langle A_v, A_c \rangle. \quad (4.8)$$

This construction shows that the ITC results from starting with the stabilizer toric code and “confining” the pointlike excitations by including the single-site check operators X_e and Z_f .

This confinement procedure is worth discussing. In the realm of stabilizer codes, the only way to confine the pointlike excitations is to condense the extended excitations. Instead, subsystem codes allow for confinement without condensation. In the language of Ref. [27] we are “gauging out” the extended excitations of the underlying toric codes, leaving the pointlike excitations as the only gapped excitations. This procedure is the essential process that allows for a physical interpretation of single-shot error correction in the ITC. The extended excitations do proliferate, but they remain detectable.

Note that \mathcal{G}_{ITC} (4.7) is invariant under the \mathbb{Z}_2 symmetry

$$U_{CX} = \prod_{\langle ef \rangle} CX_{ef}, \quad (4.9)$$

where $\langle ef \rangle$ are nearest neighbors and $CX_{ij} X_i CX_{ij} = X_i X_j$. The symmetry U_{CX} maps $X_e \leftrightarrow X_e B_e$ and $Z_f \leftrightarrow Z_f B_f$, while leaving the A and B operators unchanged.

With periodic boundary conditions, there are also nonlocal stabilizers [27] in the ITC. First, note that arbitrary products of stabilizers look like membrane operators from the underlying stabilizer toric codes. Contractible membranes may be constructed this way. However, noncontractible membranes still commute with all the check operators and can be written as products of check operators. These operators are stabilizers by definition, but cannot be generated by the local stabilizers in (4.8). Thus, for every noncontractible membrane we may have to define a nonlocal X_e -type stabilizer and nonlocal Z_f -type stabilizer.

On the three-torus (or any other manifold without boundary, regardless of genus) there are no logical qubits. In an $L \times L \times L$ lattice, there are $3L^3$ edges and $3L^3$ faces. This means there are $N = 6L^3$ physical qubits and $3L^3$ of the X_e (and Z_f) operators. There are L^3 distinct A_v (and A_c) stabilizers, but only $L^3 - 1$ are independent due to the relation $\prod_v A_v = \mathbb{1}$ ($\prod_c A_c = \mathbb{1}$). There are also 6 nonlocal stabilizers. Similarly, there are $3L^3$ distinct B_e (and B_f) operators, but $L^3 + 2$

relations between them [19], for $2L^3 - 2$ independent B_e (and B_f) operators. Altogether, there are

$$K = N - \frac{1}{2} (\log_2 |\mathcal{G}| + \log_2 |\mathcal{S}|) = 0 \quad (4.10)$$

logical qubits on the three-torus. We can create logical qubits by defining suitable boundary conditions.

4.2.3 Constructing boundaries

To define a logical qubit, let our cubic lattice have the topology $T^2 \times I$, a cube with periodic boundary conditions in two directions. Suppose that the lattice is periodic in the front/back direction and the top/bottom direction. The boundary consists of two disjoint tori; on the right torus we impose the intertwined boundary conditions and on the left torus the trivial boundary conditions. In the Appendix we construct the e - and m -condensed boundaries, giving rise to the ITC on a cube with no periodic boundary conditions.

The trivial (left) boundary follows simply from truncating our lattice in such a way that the boundary edges host qubits and boundary faces do not. We keep all the single-body X_e and Z_f check operators, along with any B_e and B_f check operators that remain four-body. For a vertex v and a boundary cube c on the trivial boundary, this results in the stabilizers

$$A_v = \begin{array}{c} \text{green lines} \\ \text{at vertex } v \end{array}, \quad A_c = \begin{array}{c} \text{blue cube} \\ \text{at boundary } c \end{array} \quad (4.11)$$

each of which acts on five qubits. Note that we can use these to construct membrane operators that span the periodic directions, so that there are no independent nonlocal stabilizers given these boundary conditions.

To construct the intertwined (right) boundary, truncate the lattice in the same way, with qubits on boundary edges but not faces. On every boundary edge we replace the single-site X_e

check with the operators

$$K_e = X_e X_{f(e)} = \begin{array}{c} \text{green square} \\ | \\ \text{green parallelogram} \end{array}, \quad (4.12)$$

where $f(e)$ is the unique nonboundary face containing e in its boundary. The truncated A_v operators are still stabilizers, but the truncated A_c operators anticommute with some K_e operators. We can construct valid stabilizers by dressing each naive A_c with a B_f operator to create

$$A_v = \begin{array}{c} \text{green cross} \\ | \\ \text{green cross} \end{array}, \quad A_c = \begin{array}{c} \text{blue cube} \end{array} \quad (4.13)$$

for a vertex v and a cube c on the intertwined boundary.

The trivial and intertwined boundaries are related to each other by U_{CX} (4.9), in the sense that $K_e \leftrightarrow X_e$ under the symmetry. Thus, applying U_{CX} to the entire lattice simply swaps the two boundaries.

With these boundary conditions, the ITC encodes $K = 2$ logical qubits. The counting of both the check operators and the constraints is easiest on a lattice with length L in the periodic directions and length $L + 1$ in the other direction. There are $3L^3 + 2L^2$ qubits on edges and $3L^3 - L^2$ qubits on faces, for a total of $N = 6L^3 + L^2$ physical qubits. There are L^2 of the K_e operators on the intertwined boundary, leaving $3L^3 + L^2$ edges to host X_e operators, while all $3L^3 - L^2$ faces have Z_f operators. We find $L^3 + L^2 - 1$ independent A_v operators and $L^3 - 1$ independent A_c operators. There are $3L^3 + L^2$ total B_f operators and $L^3 + 1$ relations between them, giving $2L^3 + L^2 - 1$ independent B_f operators. There are $3L^3 - 2L^2$ total B_e operators and $L^3 - L^2 + 1$ relations between them, leaving $2L^3 - L^2 - 1$ independent B_e operators. Thus, there are

$$K = N - \frac{1}{2} (\log_2 |\mathcal{G}| + \log_2 |\mathcal{S}|) = 2 \quad (4.14)$$

logical qubits. In the next subsection we construct bare and dressed logical operators for one of the logical qubits.

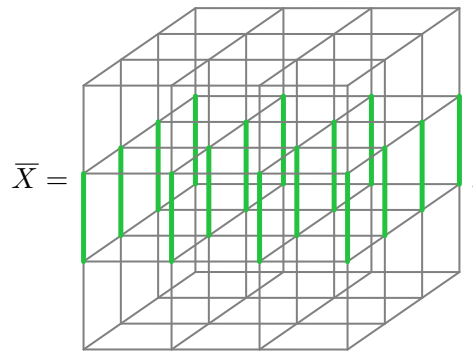
4.2.4 Logical operators

Recall that bare logical operators commute with all check operators (and therefore all stabilizers), while dressed logical operators commute with all stabilizers but not all check operators. In the bulk, we can construct membrane operators,

$$\bar{Z} = \prod_{f \in \mathcal{M}} Z_f, \quad \bar{X} = \prod_{e \in \mathcal{M}^*} X_e, \quad (4.15)$$

where \mathcal{M} and \mathcal{M}^* are a membrane and *dual* membrane, respectively. If these membranes are contractible, then the associated operators are products of local stabilizers and therefore trivial logical operators. If the membranes are closed but noncontractible, then the operators are (possibly nonlocal) stabilizers, as previously discussed. To define logical operators, the membranes must terminate on open boundaries.

At the trivial boundary, all bare logical operators may terminate without violating any check operators. At the intertwined boundary, the naive termination of \bar{X} commutes with all check operators, resulting in



$$\bar{X} = \text{[Diagram of vertical green lines in a 3D grid]}, \quad (4.16)$$

where, recall, the lattice is periodic in the top/bottom direction and the front/back direction. This operator is *not* a product of check operators (and therefore not a stabilizer) because the single-site

X_e operators on the intertwined boundary is not in the check group \mathcal{G}_{ITC} (4.12). However, the naive termination of \bar{Z} anticommutes with the check operators K_e for every edge e in $\mathcal{C} = \partial\mathcal{M} \cap \text{Int}$, the intersection of the membrane boundary with the intertwined boundary. We can fix this by dressing the \bar{Z} membrane operator with $\prod_{e \in \mathcal{C}} Z_e$, as in

$$\bar{Z} = \text{[Diagram of a 3D grid with a blue shaded plane and a vertical blue line, representing the dressed logical operator \bar{Z}].} , \quad (4.17)$$

which satisfies all the K_e check operators. It is straightforward to verify that \bar{X} and \bar{Z} anticommute, showing that they are the bare logical operators for one of the two logical qubits.

The logical operators for the other logical qubit locally look like \bar{X} and \bar{Z} , but are stretched in the opposite directions. If we name the new logical operators \bar{X}_2 and \bar{Z}_2 , then \bar{X}_2 is now periodic in the top/bottom direction and \bar{Z}_2 is periodic in the front/back direction. This confirms that the ITC with periodic boundary conditions in the top/bottom direction and the front/back direction encodes two logical qubits. In the Appendix we define the e -condensed (m -condensed) boundary, where only the logical Z operator (logical X operator) can terminate. We use these to define the ITC with only a single logical qubit.

The dressed logical operators are stringlike operators $\tilde{Z} = \prod_{e \in \mathcal{C}} Z_e$ and $\tilde{X} = \prod_{f \in \mathcal{C}^*} X_f$, where \mathcal{C} and \mathcal{C}^* are a noncontractible curve in the top/bottom direction and a noncontractible *dual* curve in the front/back direction, respectively. These operators anticommute with the bare logical operators \bar{X} and \bar{Z} , but commute with each other. This is possible because they act on the logical qubits *and* the nonlocal “check qubits,” as described previously.

In fact, the dressed logical operators are so named because they can be written as the bare logical operators dressed with (possibly many) check operators. For example the Z_f operators

in 4.17 are all check operators. Multiplying \bar{Z} by the individual Z_f operators removes them, leaving behind just the line of Z_e operators on the intertwined boundary. This is a dressed logical operator \tilde{Z} . We can obtain other dressed logical operators by multiplying \tilde{Z} by various B_f check operators, moving it into the bulk.

Whereas one of the logical operators in the 3d stabilizer toric code is inherently membranelike, the ITC possesses stringlike (dressed) logical operators for both sectors. Thus, we have traded some stability in one sector for extra stability in the other. In the next section, we will show how this stability results in detectability of partial logical operators.

4.3 Errors and error correction

Having defined the check operators, stabilizers, and logical operators, we are prepared to describe the results of both qubit errors and measurement errors. We focus on Z -type qubit errors and X -type measurement errors, as the description of the other types follows analogously. One option is to describe the measurement outcomes of the B operators and single-site check operators defined previously. This would result in measurement outcomes like those in Fig. 4.1a, with green for violated X_e and orange for violated B_e . Instead, here we use a basis of \mathcal{G}_{ITC} that more closely mirrors the KVC, allowing us to use their decoder. We are only going to choose a different set of generators for the check group, leaving the check group itself unchanged, along with the lattice, geometric boundary conditions, stabilizers, and logical operators. Thus, we really are analyzing the same ITC, just with a different presentation.

On the same lattice, with qubits on edges and faces, define the operators

$$K_e = X_e B_e = X_e \prod_{f \in \partial^{\dagger} e} X_f, \quad (4.18)$$

$$K_f = Z_f B_f = Z_f \prod_{e \in \partial f} Z_e, \quad (4.19)$$

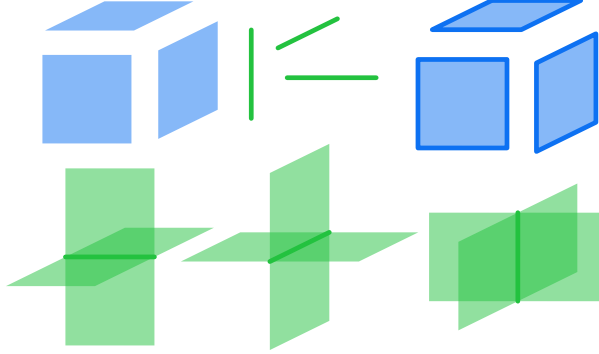


Figure 4.2: Check operators in an alternative presentation of the ITC. Green and blue represent X and Z operators respectively. Solid bars are edges, and shaded parallelograms are faces. On the top row we have the operators Z_f , X_e , and K_f , while on the bottom row we have the K_e check operators.

shown in Fig. 4.2. The check group

$$\mathcal{G}_{\text{ITC}} = \langle X_e, Z_f, K_e, K_f \rangle, \quad (4.20)$$

is the same as \mathcal{G}_{ITC} in (4.7). The stabilizers are still the vertex and cube stabilizer operators,

$$A_v = \prod_{e \in \partial v} X_e = \prod_{e \in \partial v} K_e, \quad (4.21)$$

$$A_c = \prod_{f \in \partial c} Z_f = \prod_{f \in \partial c} K_f, \quad (4.22)$$

from (4.8), as they had to be. The relations (4.21) and (4.22) between check operators provides redundancy that we lacked in the previous section. They allow us to detect measurement errors in addition to qubit errors, which improves the decoding procedure.

On the trivial boundary we have the same check operators as before. For a boundary face, the K_f operator truncates to a four-body operator equivalent to B_f . For a boundary edge, naive truncation of K_e leads to two body operators $X_e X_{f(e)}$ which we choose to discard. We instead keep X_e for each boundary edge, resulting in the same set of check operators as before and the same stabilizers as in (4.11).

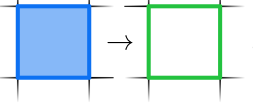
On the intertwined boundary, we make the other choice and keep the two-body operator $K_e = X_e X_{f(e)}$, justifying the name we previously gave this operator. Thus, we arrive at the same check operators and stabilizers as previously in (4.12) and (4.13).

In this section we describe the measurement outcomes of the KVC-inspired basis of measurements for the ITC. In Sec. 4.3.1 we explore the ideal measurement outcomes that result from applying local qubit errors, using linear maps defined in Ref. [71]. Then we apply some logical operators transversally (as a series of local errors) in Sec. 4.3.2 and see which check operators they violate along the way. In Sec. 4.3.3 we outline how to use the measurement outcomes to perform single-shot error correction, even in the presence of measurement errors.

4.3.1 Local errors

Recall that any code state satisfies all stabilizers but violates many check operators. To construct a generic code state, start in a state $|X_0\rangle$ that satisfies all stabilizers and all X -type check operators. This state exists, as all these operators commute. Then, create a generic code state by acting with Z -type check operators on $|X_0\rangle$. The resulting state is still a code state and satisfies all stabilizers, but violates some X -type check operators. More specifically, consider a Z -type check operator η and the linear map δ_M , which maps η to the set of check operators that anticommute with it. The nontrivial measurement outcome of X -type measurements on the state $\eta|X_0\rangle$ is $\delta_M\eta$.

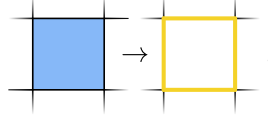
To illustrate this, let the Z -type check operator be $\eta = K_f$ so that the measurement outcome is $\delta_M\eta = \prod_{e \in \partial f} X_e$, four X_e operators around the face f . Graphically, this relationship is



$$\quad , \quad (4.23)$$

with η on the left and $\delta_M\eta$ on the right. Similarly, the Z_f check operator anticommutes with the

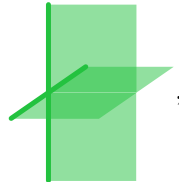
four K_e operators on edges around the face f . This relationship is



$$\text{blue square with yellow border} \rightarrow \text{yellow square with blue border}, \quad (4.24)$$

where yellow lines are violated K_e check operators. By stacking many check operators we can create the measurement outcome of a generic code state, which consists of many green and yellow lines, all of which must form closed loops.

For a vertex v on the trivial boundary (chosen to be on the left hand side) we have to measure the additional operator

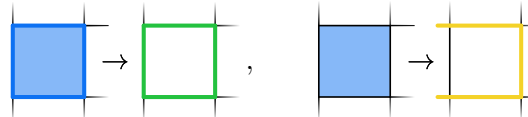


$$A_v^{2d, \text{ eff}} = \text{green cube with diagonal cut}, \quad (4.25)$$

which can be shown to be in the check group. This operator supplies redundancy in the definition of A_v for v on the trivial boundary.¹ In particular, the redundancy is

$$A_v = \prod_{e \in \partial^\dagger v} X_e = A_v^{2d, \text{ eff}} K_{e(v)}, \quad (4.26)$$

where $e(v)$ is the unique nonboundary edge in $\partial^\dagger v$. Let us draw violated $A_v^{2d, \text{ eff}}$ operators as short yellow lines sticking out of the lattice. Green lines still cannot end, but we can see from



$$\text{blue square with green border} \rightarrow \text{green square with blue border}, \quad \text{blue square with yellow border} \rightarrow \text{yellow square with blue border}, \quad (4.27)$$

that yellow lines can end if they extend to the left of the boundary.

¹Thank you to Yaodong Li for pointing out the necessity of measuring this operator.

On the intertwined boundary (on the right side) we must measure the redundant operator

$$A_v^{2d} = \begin{array}{c} \text{green line} \\ \diagup \quad \diagdown \\ \text{green line} \end{array}, \quad (4.28)$$

analogous to 4.25. The redundancy in stabilizer operators is

$$A_v = \prod_{e \in \partial^{\dagger} v} K_e = A_v^{2d} X_{e(v)}, \quad (4.29)$$

for a vertex v on the intertwined boundary. Let us draw violations of A_v^{2d} as green lines extending beyond the boundary. Measurement outcomes such as

$$\begin{array}{ccc} \text{blue square} & \rightarrow & \text{green square} \\ \text{---} & & \text{---} \end{array}, \quad \begin{array}{ccc} \text{blue square} & \rightarrow & \text{yellow square} \\ \text{---} & & \text{---} \end{array} \quad (4.30)$$

tell us that now green lines can end if they extend to the right of the boundary. To summarize, the violated check operators in any code state consist of closed green (X_e) and yellow (K_e) loops in the bulk. Yellow loops may end at the trivial boundary and green lines may end at the intertwined boundary.

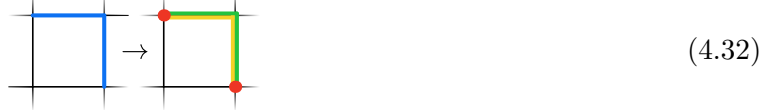
To leave the code space, act with an operator that anticommutes with some stabilizers. Any such operator, called an error, is not in the check group. We can extend the map δ_M to map an error ϵ to the check operators $\delta_M \epsilon$ that it anticommutes with. Another map, called ∂_S , maps an error to a stabilizer syndrome, the set of stabilizers it anticommutes with. We can represent both maps graphically, simultaneously. For example, in

$$\begin{array}{ccc} \text{blue square} & \rightarrow & \text{green line} \text{ (left)} \cap \text{yellow line} \text{ (right)} \\ \text{---} & & \text{---} \end{array}, \quad (4.31)$$

we have ϵ on the left and both $\delta_M \epsilon$ and $\partial_S \epsilon$ on the right. The Z -type error on the left anticommutes

with two X_e check operators (green), two K_e check operators (yellow), and two A_v stabilizers (red).

A different error,

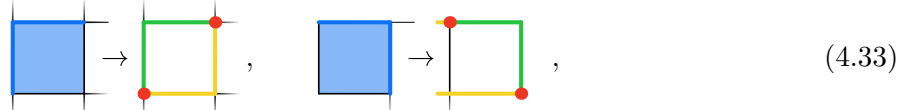


also maps to two X_e check operators, two K_e check operators, and two A_v stabilizers.

Composing similar errors creates generic syndromes and measurement outcomes, subject to some constraints called relations. The relations say that green lines and yellow lines can only end on red points, and red points must have an odd number of green lines and an odd number of yellow lines incident upon them. Phrased in terms of operators, the relation is that, for any vertex v , the number of violated K_e and X_e operators on the edges in $\partial^{\dagger}v$ must have the same parity. If that parity is odd then the stabilizer A_v is violated, and if the parity is odd then A_v is satisfied. These relations follow from (4.21) and (4.22). In other words, violated stabilizers are connected by violated check operators, so that they are no longer purely pointlike errors. In Sec. 4.3.3 we show how these connecting lines allow us to probabilistically determine the locations of the true qubit errors, even in the presence of measurement errors.

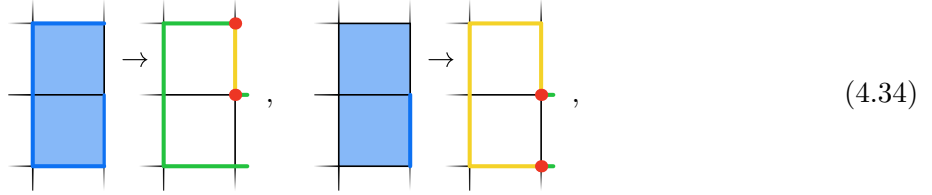
On the trivial boundary we know that yellow lines can end without violating stabilizers.

Errors cause measurement outcomes that look like



which show that violated stabilizers still need green and yellow lines attached to them, but yellow lines may end without a corresponding violated stabilizer to the left of the boundary. The intertwined

boundary instead allows configurations like



so that green lines can end without a corresponding violated stabilizer. To summarize, red dots (violated A_v syndromes) need to be connected to green and yellow lines. Yellow lines may end without a violated stabilizer at the trivial boundary and green lines may end without a violated stabilizer at the intertwined boundary.

In the coarse-grained description of the ITC, any Z -type error consists of sets of membranes of Z_f operators and strings of Z_e operators. A bare string of Z_e operators anticommutes with X_e and K_e check operators along its length. A bare membrane of Z_f operators anticommutes with K_e check operators around its boundary, and a Z_f membrane dressed with Z_e operators around its boundary anticommutes with X_e check operators around that boundary. Open Z_e strings violate A_v stabilizers at their endpoints. These rules allow us to invert the δ_M map and find a representative error that can cause any valid measurement outcome. For example, the measurement outcome represented graphically in Fig. 4.1b could be caused by the error shown in Fig. 4.4a.

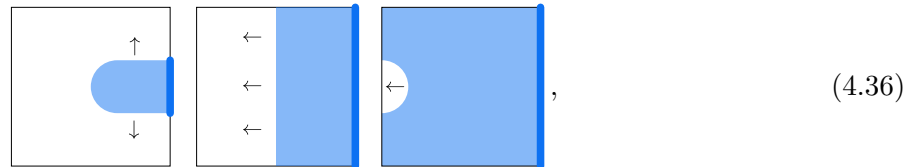
4.3.2 Transversal logical errors

Isolated errors are not so dangerous. Problems arise when errors conspire to mimic logical operators. For example, applying a string of Z_e errors is the same as applying a partial Z -type dressed logical operator. Applying a logical operator this way, as a series of local operators, is called a transversal decomposition of the logical operator. At any point in the decomposition, the partial logical operator results in violated A_v stabilizers at its endpoints. Thus, a transversal decomposition of the Z -type dressed logical operator transports violated A_v operators across the system, leaving behind violated X_e and K_e check operators.

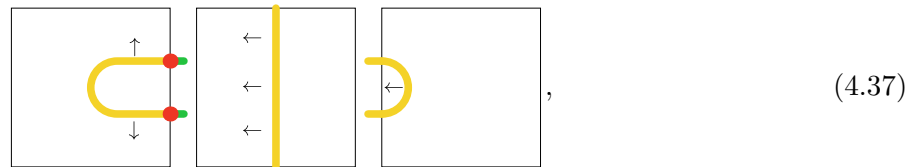
Recall the Z -type bare logical operator



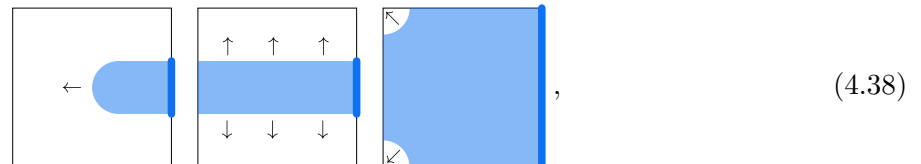
drawn as a slice through the entire lattice. The figure represents a coarse-grained version of the one in (4.17). We could apply this operator transversally in many different ways. We could truncate it from right to left,



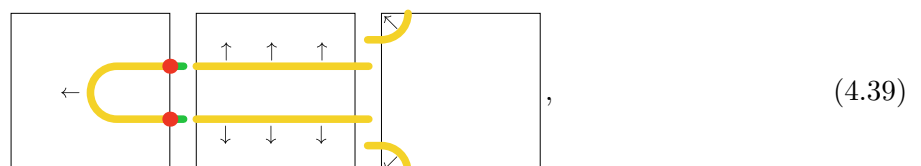
resulting in the measurement outcomes



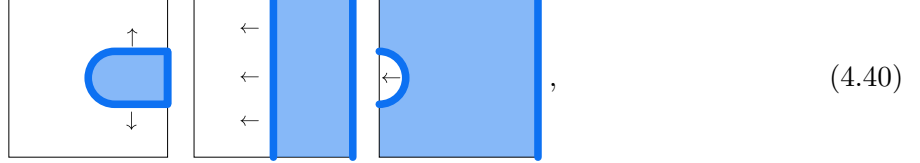
where the noncontractible strings of violated K_e check operators witnesses the partial logical operator. A geometrically different transversal decomposition of the bare logical operator,



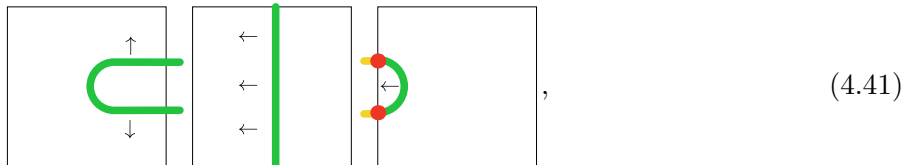
results in the measurement outcomes



where there are still noncontractible strings of violated K_e check operators, now stretching from one boundary to the other. A different transversal decomposition of \bar{Z} uses a different boundary,



resulting in the measurement outcomes



where the noncontractible strings now consist of violated X_e checks. Note that the violated stabilizers can appear on the left or right boundary, depending on the decomposition. Other decompositions can result in the violated stabilizers appearing anywhere in the bulk.

What is constant is that all decompositions involve transporting a pair of violated stabilizers vertically across the system and then removing the resulting violated check operators at the left and right boundary. Thus, either type of logical operator transports violated stabilizer across the system, and the difference is that dressed logical operators leave violated check operators behind while bare logical operators remove the violated check operators at the boundary.

4.3.3 Single-shot error correction

The point of any error-correction procedure is to prevent local errors from accumulating into logical errors. To that end, we want to detect and undo any partial logical operators. The simplest way is to find all violated stabilizers and pair them up to correct them while introducing the fewest residual errors. One way to do this in the stabilizer toric code is the minimal-weight perfect matching (MWPM) procedure [25].

The MWPM procedure successfully decodes the stabilizer toric code as long as measurements

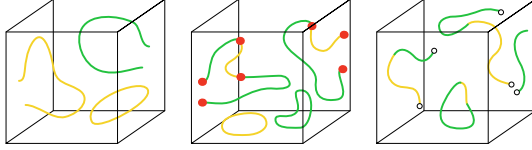


Figure 4.3: Syndromes in the KVC-inspired presentation of the ITC. On the left we have a syndrome for a code states with no qubit or measurement errors. The middle figure displays qubit errors, represented by red dots which are violated stabilizers, but no measurement errors. On the right we have measurement errors represented by empty circles which are violated relations.

are ideal. However, incorrect measurements, where the wrong measurement outcome is written down, completely ruin the MWPM procedure for pointlike stabilizers. The problem is that a small number of incorrect measurements can lead to a large number of residual errors.

Connecting violated stabilizers with violated check operators, as in the GCC, the KVC, and the ITC, helps to recover from measurement errors. In fact, the syndromes of the ITC look like the syndromes of the KVC, at least when coarse-grained as in Fig. 4.3. This allows us to use the single-shot version of the MWPM procedure introduced in Ref. [71].

The single-shot MWPM procedure consists of two steps, which we describe first heuristically and then in more mathematical detail. The first step deals with violations of the relations from Sec. 4.3.1, which are unpaired endpoints of the measurement outcomes. These violations, collectively called the relation syndrome, are aphysical and can only result from measurement error. For example, if the true measurement outcome is a closed line of violated X_e check operators, some false negatives along this line result in endpoints of the line. The relation syndromes are the white circles in Fig. 4.3. The first round of MWPM pairs up these violated relations, inferring the shortest strings of measurement errors that could have caused them.

After inferring the measurement errors, we are left with valid measurement outcomes, with their attendant stabilizer syndromes. Recall that violated stabilizers are vertices where X_e and K_e lines simultaneously end. These are marked with red dots in Fig. 4.3. The second round of MWPM pairs up the violated stabilizers, matching the stabilizers in a way that is robust to measurement errors. Finally, error correction proceeds by acting with operators that remove the

violated stabilizers.

To describe the process in more detail, the next part of this section unifies the entire error-correction procedure as a series of linear maps between vector spaces, closely following the discussion of single-shot error correction in Ref. [71]. We outline the important steps, highlighting the places where the ITC differs from the KVC.

We have been describing the ITC in terms of sets and groups: the set of qubits, the check group, the stabilizer group, the set of relations, etc. To formalize the decoding problem, we redefine these as vector spaces over \mathbb{F}_2 , the field with two elements. These spaces are the space of Z -type check operators C_G , the space of qubits C_Q , the space of X -type check operators C_M , the space of stabilizers C_S , and the space of relations C_R . For example, an element of C_S corresponds to an element of the stabilizer group, and an element of C_Q corresponds to a subset of the qubits. An “error” involves a Z -type qubit error $\epsilon \in C_Q$ and a measurement error $\mu \in C_M$, while a “syndrome” includes both the violated stabilizers $\sigma \in C_S$ and the violated relations in $\omega \in C_R$.

We already defined some linear maps between these spaces in Sec. 4.3.1: δ_M maps an error $\epsilon \in C_Q$ to the set of check operators $\delta_M \epsilon \in C_M$ that it anticomutes with, δ_S maps a measurement outcome $\zeta \in C_M$ to the inferred syndrome $\delta_S \zeta \in C_S$ and ∂_S maps an error ϵ to the syndrome $\partial_S \epsilon \in C_S$ that it causes. These maps obey

$$\partial_S = \delta_S \delta_R \quad (4.42)$$

by definition. We also define some new maps: ∂_Q maps a Z -type check operator $\gamma \in C_G$ to the set of qubits $\partial_Q \gamma \in C_Q$ on which it acts, and δ_R maps a measurement outcome ζ to its relation syndrome $\delta_R \zeta \in C_R$.

The above-defined maps must obey some constraints coming from the definition of subsystem codes. First, the constraint

$$\partial_S \partial_Q = 0 \quad (4.43)$$

says that the Z -type check operators commute with the X -type stabilizers. Second, the constraint

$$\delta_R \delta_M = 0 \quad (4.44)$$

says that physical errors do not cause relation syndromes. These constraints are all encoded in a commutative diagram taken directly from Ref. [71],

$$\begin{array}{ccccc}
& & X\text{-type check} & & \\
& & \text{measurements} & & \\
& & C_M & & \left(\begin{array}{c} \delta_S \\ \hline \delta_R \end{array} \right) \\
& & \left(\begin{array}{c|c} \delta_M & I \end{array} \right) & \nearrow & \\
C_G & \xrightarrow{\left(\begin{array}{c} \partial_Q \\ \hline 0 \end{array} \right)} & C_Q \oplus C_M & \xrightarrow{\left(\begin{array}{c|c} \partial_S & \delta_S \\ \hline 0 & \delta_R \end{array} \right)} & C_S \oplus C_R \\
Z\text{-type} & & \text{qubits and } X\text{-type} & & \text{stabilizers} \\
\text{check operators} & & \text{measurements} & & \text{and relations} \\
& & & & \\
& & & & (4.45)
\end{array}$$

where the block matrix structure of the maps follows from treating elements of the vector spaces as column vectors.

In the ITC, these spaces and maps decompose even further, simplifying the discussion. For example, the space of Z -type check operators is $C_G = C_{Zf} \oplus C_{Kf}$, the direct sum of the spaces of Z_f and K_f check operators. The space of qubits is $C_Q = C_E \oplus C_F$, the direct sum of the spaces of edge qubits and face qubits, with C_{Zf} , C_{Kf} , and C_F all isomorphic to the space of faces in the lattice. The space of X -type check operators decomposes into $C_M = C_{Xe} \oplus C_{Ke}$, the direct sum of the spaces of X_e and K_e check operators, with C_{Xe} , C_{Ke} , and C_E all isomorphic to the space of edges on the lattice. The space of stabilizers C_S and the space of relations C_R are both isomorphic to the space of vertices.

Each block of the block matrices in (4.45) also decomposes into a block structure. Furthermore, the individual components are simply the identity I and the geometric boundary operator ∂ in

the bulk, although these may have to be truncated or supplemented at either boundary. The first column of

$$\partial_Q = \left(\begin{array}{c|c} 0 & \partial \\ \hline I & I \end{array} \right) \quad (4.46)$$

says that the \mathcal{Z}_f check operator acts on a single face qubit, while the second column says that K_f acts on a single face qubit and the four edge qubits that surround it. Similarly, the first column of

$$\delta_M = \left(\begin{array}{c|c} I & 0 \\ \hline I & \partial \end{array} \right) \quad (4.47)$$

says that a Z_e error anticommutes with the X_e and K_e check operator on that edge, while the second column says that a Z_f error anticommutes with the four K_e check operators around that face. Equations (4.23) and (4.24) represent (4.47) graphically. The two maps

$$\delta_S = \left(\begin{array}{c|c} \partial & 0 \end{array} \right), \quad \delta_R = \left(\begin{array}{c|c} \partial & \partial \end{array} \right) \quad (4.48)$$

say that violated stabilizers are vertices with an odd number of violated X_e check operators around them, while violated relations are vertices with an odd total number of violated X_e and K_e check operators around them, respectively. The last map, $\partial_S = \left(\begin{array}{c|c} \partial & 0 \end{array} \right)$, maps a set of qubit errors directly to the stabilizers it violates.

The decompositions automatically satisfy the constraints $\partial_S = \delta_S \delta_M$, $\partial_S \partial_Q = 0$, and $\delta_R \delta_M = 0$. The point of including this whole decomposition is to show that the decoding maps in the ITC are nicely geometric, like the decoding maps in the stabilizer toric codes.

The decoding strategy takes two steps. As described previously, code states have nontrivial syndromes generated by $\gamma \in C_G$, a set of Z -type check operators. The initial γ and some errors

$\epsilon \oplus \mu \in C_Q \oplus C_M$ produce a measurement outcome

$$\zeta = \delta_M \epsilon + \mu + \delta_M \partial_Q \gamma \in C_M. \quad (4.49)$$

This measurement outcome violates a set of relations $\delta_R \zeta$, allowing us to infer a measurement error $\hat{\mu}$ with the same relation syndrome $\delta_R \hat{\mu} = \delta_R \zeta$. The resulting inferred stabilizer syndrome is $\delta_S(\zeta + \hat{\mu})$, allowing us to infer a qubit error $\hat{\epsilon}$ such that $\partial_S \hat{\epsilon} = \delta_S(\zeta + \hat{\mu})$. After correcting for the inferred error, the residual error is $\epsilon + \hat{\epsilon}$. If the decoding procedure succeeds perfectly, we have $\hat{\epsilon} = \epsilon + \partial_Q \gamma'$, where $\gamma' \in C_G$, so that the residual stabilizer syndrome is $\partial_S(\epsilon + \hat{\epsilon}) = \partial_S \partial_Q \gamma' = 0$. This is the doubled MWPM procedure from Ref. [71]. Even if the decoding procedure does not proceed perfectly, the residual stabilizer syndrome should be equivalent to one caused by a small number of qubit errors.

An advantage of the ITC is that both rounds of MWPM occur on the graph defined by the edges and vertices of the cubic lattice. In both cases, the violations appear on vertices and the inferred errors appear on edges. Similarly, for X -type qubit errors and Z -type measurement errors, the violations appear on cubes and the inferred errors appear on faces. This is geometrically dual to the previous cases. In all cases, the problems of finding $\hat{\mu}$ and $\hat{\epsilon}$ simply reduce to MWPM on the cubic lattice. At this point we can rely on the results from Ref. [71] to show that the ITC is indeed capable of single-shot error correction.

Moving beyond the analysis of Ref. [71], we can achieve maximal redundancy by measuring all six types of check operators: X_e , Z_f , K_e , K_f , B_e , and B_f . This set is overcomplete in the sense that to every edge there corresponds three check operators, with a nontrivial relation between them: $K_e X_e B_e = 1$. We can use the previous analysis to infer the relations for X -type check operators in the bulk. Every edge must be occupied by zero or two violated check operators. Lines of violated B_e check operators may not end, while K_e and X_e lines only end on violated stabilizers. Violated stabilizers must be simultaneous endpoints of K_e and X_e lines. These rules are illustrated in Fig. 4.4. On the trivial boundary, K_e and B_e lines may end without violated stabilizers, and violated stabilizers only need to be endpoints of X_e lines. On the intertwined boundary, X_e and B_e

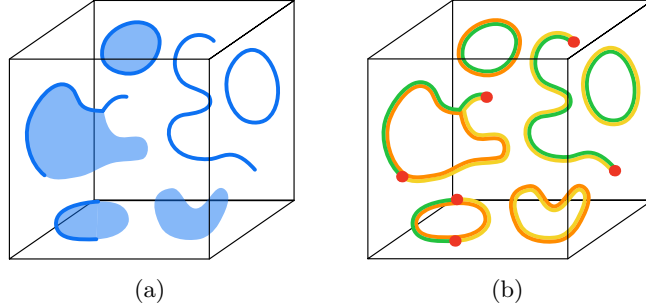


Figure 4.4: An error in the ITC and its overcomplete syndrome. (a) If shaded blue areas are Z_f errors and blue lines are Z_e errors, this is the error causing the syndromes shown in Fig. 4.1. (b) Measuring an overcomplete set of check operators leads to maximally redundant syndromes, where every line must be coincident with a line of another color. Note that removing yellow lines gives Fig. 4.1a while removing orange lines gives Fig. 4.1b.

lines may end without violated stabilizers, and violated stabilizers only need to be endpoints of K_e lines.

In this overcomplete version of the ITC, the nontrivial relation $K_e X_e B_e = 1$ for every edge e means that a string of measurement errors is detectable everywhere along its length, rather than just at its endpoints. This could possibly lead to a more accurate while still efficient decoder. Of course, measuring overcomplete sets of check operators can always increase the accuracy of a decoder. This realization is not new, but might help in understanding the ITC.

4.4 Phase Diagram of the ITC

So far, we have seen that the check group \mathcal{G}_{ITC} includes some terms that we might recognize from our favorite Hamiltonians. By construction, the B terms come from the 3d toric code Hamiltonian [19]. It is easy to see that the single-site terms form a paramagnet Hamiltonian. In addition, the K terms are equivalent to terms in the Raussendorf-Bravyi-Harrington (RBH) Hamiltonian [110] after a Hadamard transformation on face qubits, mapping $X_f \leftrightarrow Z_f$. In this section we show that these three Hamiltonians live in the phase diagram corresponding to the ITC subsystem code.

4.4.1 Gapped phases in the ITC

Recall that, from a stabilizer code with stabilizer group \mathcal{S} , we can construct a gapped Hamiltonian,

$$H_{\mathcal{S}} = - \sum_{S \in \mathcal{S}} J_S S, \quad (4.50)$$

by including all the stabilizers with negative coefficients $-J_S < 0$. The coefficients for operators with large support should be small. Because the stabilizers all commute, the relative strengths of the coefficients do not matter. Thus, the stabilizer code corresponds to a single phase of matter. We can try to build a Hamiltonian from a subsystem code analogously, by including all the stabilizers and check operators with coefficients. The most general such Hamiltonian is

$$H_{\mathcal{G}} = - \sum_{S \in \mathcal{S}} J_S S - \sum_{G \in \mathcal{G}} J_G G + \text{h.c.}, \quad (4.51)$$

where we should again be careful to bound the strength of the coefficients for operators with large support [27]. The stabilizer coefficients J_S should be negative, but the check group contains pure phases so there is no reason to impose negativity on the check coefficients J_G .

Since the check group is non-Abelian, the Hamiltonian $H_{\mathcal{G}}$ is frustrated and different choices of coefficients may give rise to different gapped phases. Thus, the subsystem code corresponds to a whole phase diagram with different phases and phase transitions. Phase diagrams have been studied for the GCC [72] and the KVC [77]. Additionally, subsystem codes can lead to novel constructions for 2d Abelian phases [27].

To simplify the analysis of the ITC Hamiltonian, define the Hamiltonian

$$\begin{aligned} H_{\text{ITC}} = & -J_{Av} \sum_v A_v - J_{Ac} \sum_c A_c \\ & - J_{Xe} \sum_e X_e - J_{Ke} \sum_e K_e - J_{Be} \sum_e B_e \\ & - J_{Zf} \sum_f Z_f - J_{Kf} \sum_f K_f - J_{Bf} \sum_f B_f, \end{aligned} \quad (4.52)$$

which has fewer tunable parameters. This simplification means that we might not find all of the phases in the full Hamiltonian (4.51), but we can still find several interesting phases. As the A_v and A_c terms commute with everything else, we can choose to set $J_{Av} = J_{Ac} = \infty$. This in turn is equivalent to enforcing a symmetry. In fact, A_v and A_c each generate a 1-form symmetry, so we realize we are studying 1-form symmetry-protected topological (SPT) phases.

To find some phases of H_{ITC} , tune to a limit where some J_G are much larger than others. If the largest terms all commute, the resulting Hamiltonian is exactly solvable. For example, if the coefficients of the single-site terms J_{Xe} and J_{Zf} are much larger than the rest of the check coefficients, then the effective Hamiltonian is the paramagnet Hamiltonian

$$H_{\text{Para}} = -J_{Xe} \sum_e X_e - J_{Zf} \sum_f Z_f, \quad (4.53)$$

with some small perturbations. Some other exactly-solvable Hamiltonians are

$$H_{\text{TCE}} = -J_{Av} \sum_v A_v - J_{Zf} \sum_f Z_f - J_{Bf} \sum_f B_f, \quad (4.54)$$

$$H_{\text{TCF}} = -J_{Ac} \sum_c A_c - J_{Xe} \sum_e X_e - J_{Be} \sum_e B_e, \quad (4.55)$$

which each represent a single copy of the toric code stacked with a paramagnet, and

$$\begin{aligned} H_{2\text{TC}} = & -J_{Av} \sum_v A_v - J_{Ac} \sum_c A_c \\ & - J_{Be} \sum_e B_e - J_{Bf} \sum_f B_f, \end{aligned} \quad (4.56)$$

which represents the two toric codes from (4.6). Some distinct choices result in the same phases.

For example, the Hamiltonian

$$H = -J_{Av} \sum_v A_v - J_{Zf} \sum_f Z_f - J_{Kf} \sum_f K_f, \quad (4.57)$$

belongs to the same phase as H_{TCE} because $Z_f K_f = B_f$.

Another useful limit is the RBH Hamiltonian

$$H_{\text{RBH}} = -J_{Ke} \sum_e K_e - J_{Kf} \sum_f K_f, \quad (4.58)$$

whose ground state is the 3d cluster state [110]. This Hamiltonian is in the trivial phase, but in a nontrivial SPT phase under the 1-form symmetry generated by A_v and A_c . Altogether, we find five phases in H_{ITC} , represented by the five named Hamiltonians above.

Some of the exactly-solvable Hamiltonians have previously been shown to lead to symmetry-protected self correction. These are H_{RBH} [112], H_{Para} [125], and $H_{2\text{TC}}$ [123]. In each case the protecting symmetry is (possibly a subset of) the 1-form symmetry generated by A_v and A_c . However, in all three cases the boundary conditions must be chosen differently to lead to symmetry-protected self correction rather than single-shot error correction. It is likely that the TCE and TCF phases would also support self correction with the right choice of boundary and 1-form symmetry. In addition, the RBH phase supports symmetry-protected topological order at nonzero temperatures [114], and the other phases likely do as well.

4.4.2 Topological order in each phase

Every phase that Ref. [77] finds in the phase diagram of the KVC has topological order somewhere, either in the bulk or on the boundary. In the ITC, the phases corresponding to H_{TCE} , H_{TCF} , and H_{2TC} are topologically ordered in the bulk. In the paramagnetic and RBH phases, the topological order instead must occur on the boundary. The symmetry and the bulk Hamiltonian together restrict the possible gapped boundaries, as is common in SPTs. For example, consider the paramagnetic phase. On the trivial boundary, we can include an X_e term for every boundary edge without causing problems, giving paramagnetic boundary conditions. On the intertwined boundary, however, such a term is not in \mathcal{G}_{ITC} and would anticommute with the stabilizers. Instead, we must include the terms

$$A_v^{\text{2d}} = \begin{array}{c} \text{green vertical line} \\ \diagup \quad \diagdown \\ \text{green horizontal line} \end{array}, \quad B_f^{\text{2d}} = \begin{array}{c} \text{blue square} \\ \text{with a diagonal cut} \end{array}, \quad (4.59)$$

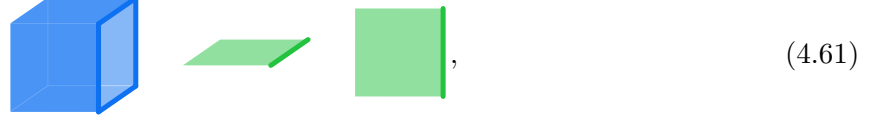
which make up a 2d toric code on this boundary. We can check that these terms are in \mathcal{G}_{ITC} . Similarly, in the RBH phase, we can include K_e for edges in the intertwined boundary, leading to no topological order there. The trivial boundary must instead have the terms

$$A_v^{\text{2d, eff}} = \begin{array}{c} \text{green square} \\ \diagup \quad \diagdown \\ \text{green horizontal line} \end{array}, \quad B_f^{\text{2d}} = \begin{array}{c} \text{blue square} \\ \text{with a diagonal cut} \end{array}, \quad (4.60)$$

which define an effective 2d toric code there. These terms are in \mathcal{G}_{ITC} and define the standard toric code boundary conditions of the RBH Hamiltonian.

In the TCE and 2TC phases the boundary conditions are just the “smooth” boundaries of the 3d toric codes, where membrane operators may terminate but stringlike operators may not. In the TCF phase this is still the case, but it is less clear on the intertwined boundary. If we include

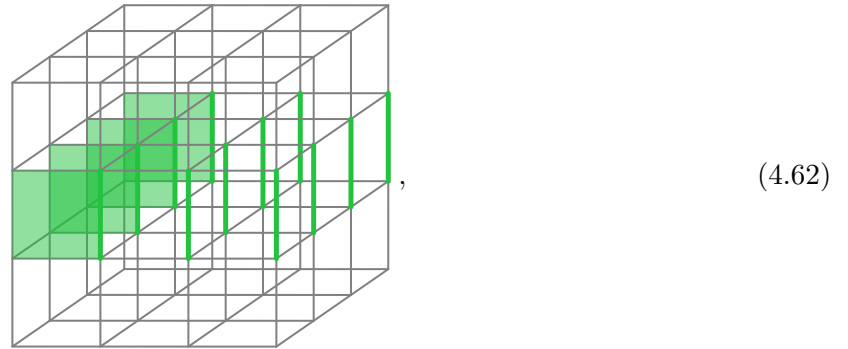
the K_e operators on the boundary edges, then the naive termination of A_c does not commute with these. Instead, we use the dressed termination of K_e from (4.12) and A_c from (4.13), so that the terms in the Hamiltonian are



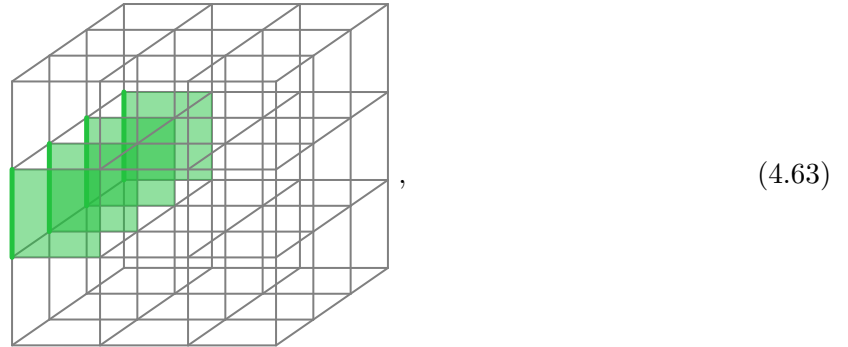
along with the terms in the bulk and on the trivial boundary. This new boundary looks funny, but is still a valid (smooth) termination of the 3d toric code on faces. It is related to the ordinary termination (on the trivial boundary) by the U_{CX} symmetry (4.9).

Reference [77] additionally shows that the bare logical operators in the subsystem code act as logical operators in every phase. In the ITC, this is particularly straightforward in the paramagnetic phase; \bar{X} (4.16) and \bar{Z} (4.17) consist of the boundary X -type logical operator dressed by X_e terms and the boundary Z -type logical operator dressed by Z_f terms, respectively. In the paramagnetic phase, the single-site X_e and Z_f terms are stabilizers, so \bar{X} and \bar{Z} remain logical operators.

In the RBH phase the relationship is not as obvious. To see that it still holds, consider a product of X -type K_e stabilizers,

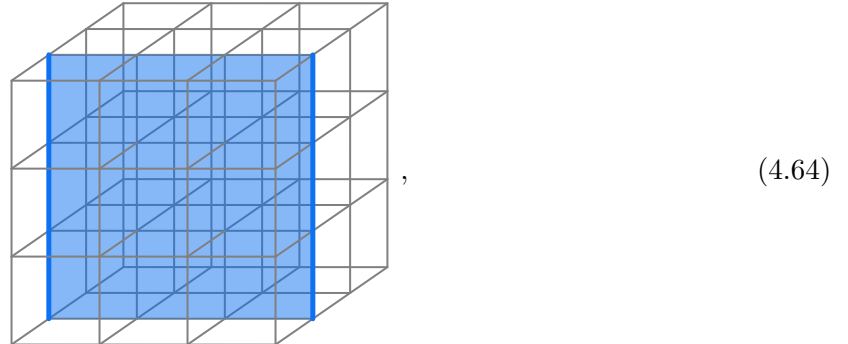


and an X logical operator on the boundary toric code,

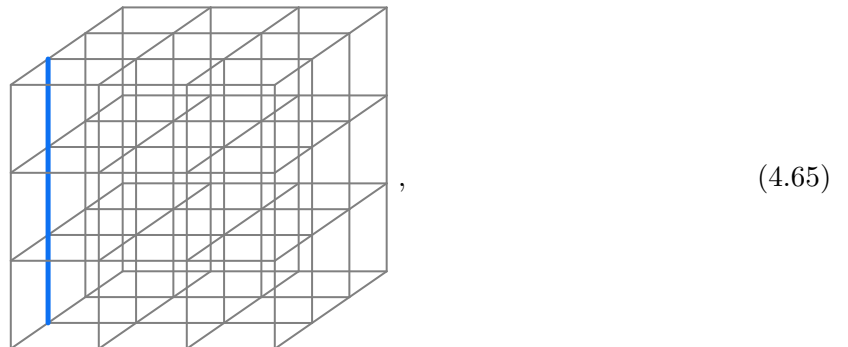


recalling that both figures are meant to be periodic in the front/back and top/bottom directions.

Multiplying these together does in fact give \bar{X} , as in (4.16). Similarly a product of Z -type K_f stabilizers,



and a Z logical operator,



multiplies \bar{Z} , as in (4.17).

In the TCE phase, \overline{X} is the membrane logical operator and \overline{Z} is the stringlike logical operator dressed with single-site Z_f stabilizers. In the TCF phase, \overline{Z} is the membrane logical operator, whose dressing is required as in (4.61). The single-site X_e operators in \overline{X} are all individual stabilizers except for those on the intertwined boundary. The latter can be multiplied by K_e on every edge to give the stringlike logical operator in the TCF phase. Since the 2TC phase just consists of the toric code on edges stacked with the toric code on faces, it is clear that \overline{X} acts only on one code while \overline{Z} acts on both. Thus, one of the logical qubits in the 2TC phase is privileged over the other. It would be interesting to find a more systematic understanding of the relationship between logical qubits in the parent subsystem code and logical qubits in individual gapped phases.

4.4.3 Constructing phase diagrams

So far, we have been analyzing individual phases via exactly-solvable Hamiltonians. By including noncommuting terms with comparable strength, we can instead build Hamiltonians with phase transitions. For example, the Hamiltonian

$$\begin{aligned} H = & - J_{Av} \sum_v A_v - J_{Zf} \sum_f Z_f \\ & - J_{Bf} \sum_f B_f - J_{Xe} \sum_e X_e \end{aligned} \tag{4.66}$$

describes 3d \mathbb{Z}_2 lattice gauge theory; the first two terms commute with everything and are always satisfied, but the second two terms compete. Within the space of states satisfying the first two terms, the second two terms are dual [32, 134], so that the phase transition happens at $J_{Bf} = J_{Xe}$ [23]. When $J_{Bf} > J_{Xe}$ the Hamiltonian is in the TCE phase, while when $J_{Bf} < J_{Xe}$ the Hamiltonian is in the paramagnetic phase, as shown in Fig. 4.5.

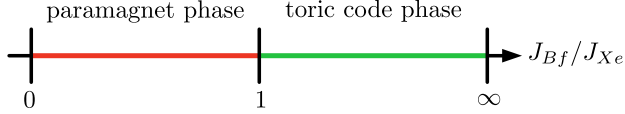


Figure 4.5: Phase diagram for the Hamiltonian in (4.66). Within the A_v - and Z_f -satisfying Hilbert space, the B_f and X_e terms are dual to each other, so that the phase transition occurs when the couple strengths are equal. The system enters the 3d toric code phase when J_{Bf} is large and enters the paramagnetic phase when J_{Xe} is larger.

Including more terms, as in

$$\begin{aligned} H = & - J_{Av} \sum_v A_v - J_{Ac} \sum_c A_c - J_{Zf} \sum_f Z_f \\ & - J_{Xe} \sum_e X_e - J_{Be} \sum_e B_e - J_{Bf} \sum_f B_f, \end{aligned} \quad (4.67)$$

results in a larger phase diagram. Note that each term acts only on edges or only on faces, so that we can analyze each sector separately. The phases and phase transitions are shown in Fig. 4.6. The phase transitions happen at $J_{Bf} = J_{Xe}$ and $J_{Be} = J_{Zf}$.

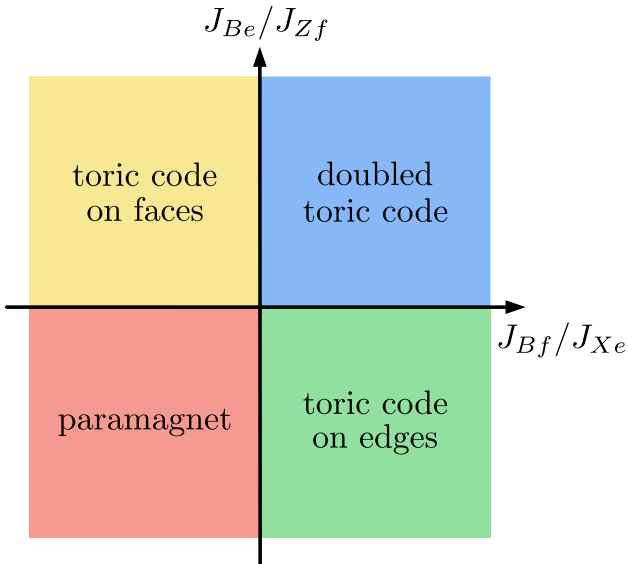


Figure 4.6: Phase diagram for the Hamiltonian in (4.67). The four phases—paramagnetic, toric code on edges, toric code on faces, and doubled toric code—have fixed points described by (4.53), (4.54), (4.55), and (4.56), respectively. The phase boundaries are vertical and horizontal lines because the edge qubits and face qubits are decoupled in the bulk.

Another useful Hamiltonian is

$$\begin{aligned} H = & -J_{Av} \sum_v A_v - J_{Ac} \sum_c A_c - J_{Zf} \sum_f Z_f \\ & - J_{Xe} \sum_e X_e - J_{Ke} \sum_e K_e - J_{Kf} \sum_f K_f, \end{aligned} \quad (4.68)$$

which is the same as (4.67) but with the B terms replaced with K terms. The edge and face qubits are coupled, so we cannot analyze the two sectors independently. However, we can still see that the relevant fixed-point Hamiltonians are H_{Para} , H_{TCE} , H_{TCF} , and H_{RBH} . Furthermore, we can find the locations of particular phase transitions. For example, by setting $J_{Ke} = 0$, we find the Hamiltonian for 3d \mathbb{Z}_2 lattice gauge theory (recall that $B_f = K_f$ within the space of states obeying $Z_f = 1$). This tells us that the transition between the paramagnetic and TCE phases happens at $J_{Kf} = J_{Xe}$ when $J_{Ke} = 0$. Similar analyses apply when any any single coupling vanishes. If we instead set $J_{Zf} = J_{Xe}$ and $J_{Kf} = J_{Ke}$ then the transition is the standard RBH to paramagnet transition, which happens when all coefficients are equal. The resulting phase diagram looks something like Fig. 4.7, where solid lines represent phase boundaries at known locations and the dashed lines represent interpolated phase boundaries. The full Hamiltonian H_{ITC} has a higher-dimensional phase diagram, with each of the five described phases appearing.

The analysis of the phase diagram suggests some possible connections to the KVC. Reference [77] shows that the KVC supports four phases: two 3d toric code phases and two trivial phases, where the trivial phases have 2d toric codes on opposite boundaries. In the ITC, the paramagnetic and RBH phases are both trivial in the bulk, in the sense that neither is topologically ordered. However, they cannot be continuously connected without closing the gap or breaking the symmetry, meaning that H_{RBH} is in an SPT phase. Thus, we say that they are not the same phase but that both are trivial. Note that they have their 2d toric codes on opposite boundaries, as is true of the two trivial phase in Ref. [77]. In this sense, H_{Para} , H_{RBH} , H_{TCE} , and H_{TCF} are all found in the KVC. These phases arrange into a phase diagram (Fig. 6 of Ref. [77]) that matches Fig. 4.7 in the

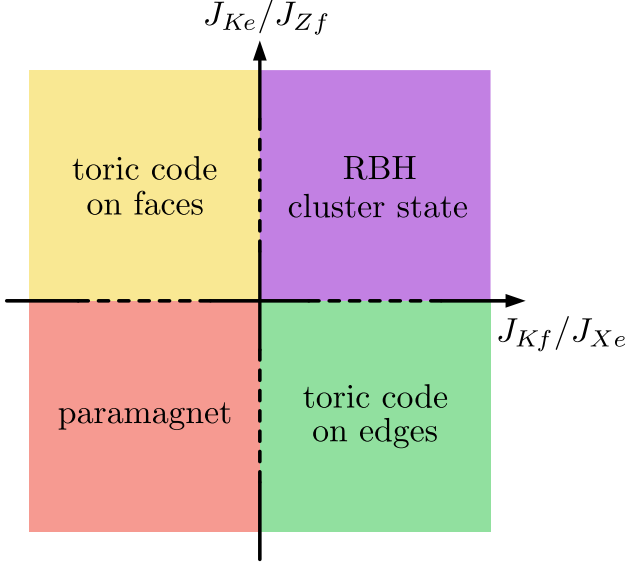


Figure 4.7: Phase diagram for the Hamiltonian in (4.68). The four phases—paramagnetic, toric code on edges, toric code on faces, and RBH cluster state—have fixed points described by (4.53), (4.54), (4.55), and (4.58), respectively. Unlike (4.68), the edge qubits and face qubits are coupled, so it is not clear that the phase boundaries should be straight lines. However, by taking 1d slices through the phase diagram we can show that the solid lines happen when various coefficients are equal. Compare to Fig. 6 of Ref. [77].

ITC.

However, the ITC also includes the doubled toric code phase ($H_{2\text{TC}}$). Reference [77] did not find such a phase in the KVC, but they did not exhaustively search the entire parameter space. If the KVC also contains a doubled toric code phase, then it would be possible that the KVC and ITC are related by some finite-depth unitary circuit, and that they are equivalent as subsystem codes.

If the KVC does not contain a doubled toric code phase, then the two codes could be related by a procedure called “partial gauge fixing.” Gauge fixing is a procedure that turns a subsystem code into a stabilizer code by choosing a maximal commuting subgroup of the check group and appending it to the stabilizer group. The resulting stabilizer code is a “gauge-fixed” version of the subsystem code [10, 97]. Each gauge-fixed stabilizer code generates a fully commuting Hamiltonian and corresponds to a particular gapped phase. In fact, each of the gapped, exactly solvable Hamiltonians studied in this section is a stabilizer Hamiltonian, and in each case the stabilizer code is a gauge-fixed version of the ITC. A subsystem code can also be partially gauge-fixed, resulting in a new subsystem

code with fewer gauge qubits and a smaller phase diagram. Thus, if the KVC does not support a doubled toric code phase, then it could be a gauge-fixed version of the ITC. This highlights the importance of the question of whether the KVC includes a doubled toric code phase. We leave this question to future work.

4.5 Remaining questions

In this paper we have introduced a new single-shot quantum error-correcting code, the intertwined toric code. The ITC possesses three main advantages. First, the ITC is physically motivated in that it descends directly from underlying toric codes and that the procedure that builds the ITC confines the problematic pointlike excitations of the toric codes. Second, the resulting code has geometrically simple logical operators and decoding procedures, both descending from the geometric simplicity of the toric codes. Third, the transparent nature of the check operators makes extracting the phase diagram for the ITC straightforward.

This work uncovers a number of promising avenues for future research. In Sec. 4.2 we constructed the ITC by adding single-site check operators to 3d toric codes, while in Sec. 4.3 we instead constructed it by adding single-site check operators to the RBH Hamiltonian. Both constructions suggest a generalization to arbitrary Walker-Wang models. The Walker-Wang construction [133] takes a 2d anyon theory as input and outputs a 3d lattice model. Using two transparent bosons as the input theory gives two copies of the toric code [66] while using the 2d toric code as input gives the RBH Hamiltonian [113]. In both cases, the vertex terms of the Walker-Wang model are equivalent to the stabilizers in the ITC. This suggests a procedure for turning a 2d anyon theory into a 3d subsystem code: Construct the Walker-Wang model corresponding to the anyon theory and then supplement with single-site check operators so that the vertex terms remain stabilizers but the face terms become check operators. Reference [14] defines another procedure for constructing 3d subsystem codes from 2d anyon theories. How are these two procedures related? Could the subsystem Walker-Wang construction shed light on the differences between the GCC and the codes constructed in Ref. [14]?

The RBH Hamiltonian also provides for fault-tolerant measurement-based quantum computation [109], wherein a 2d toric-code degree of freedom is teleported across a 3d lattice system. Initially, the bulk of the system is in the ground state of the RBH Hamiltonian and the 2d toric code is on the left boundary. After measuring single-qubit operators in the bulk, the toric code ends up on the right boundary. In the language of the ITC, this process consists of using check operators to move from the paramagnetic phase to the RBH phase. In fact, single-shot error-correction procedures in the KVC correspond to scheduled phase transitions as well [77]. What conclusions can be drawn from this connection between single-shot error correction and fault-tolerant measurement-based quantum computation?

One of the advantages of the KVC is that each check operator acts on at most three qubits. Is it possible to rewrite the ITC so that no check operator acts on more than three qubits? The presentation in Sec. 4.2 uses smaller check operators. Is it possible to perform single-shot error correction using measurements of these check operators? Heuristically, it seems possible because a single measurement error introduces a geometrically close pair of violated stabilizers, rather than a single isolated violated stabilizer (as in the 2d toric code). However, this claim would have to be checked.

The boundaries of the ITC (and the GCC and the KVC) hold outsized importance. As originally introduced in Sec. 4.2.2, the ITC with no boundaries encodes no logical qubits. However, the analysis of Sec. 4.3 shows that we can reliably detect syndromes and correct errors even without a boundary. Taken together, these statements show that reliable error correction, which follows from confinement in the ITC, is insufficient for single-shot error correction of a logical qubit. What, then, is the physical interpretation of the boundary? Furthermore, the bare logical operators commute in the bulk and only anticommute on the boundary. In the phase diagrams of Sec. 4.4, the boundaries “host” the topological order when there is no topological order in the bulk (in the paramagnetic and RBH phases). The boundaries also ruin self-correction in the sense that models exist that are self-correcting in the presence of generic perturbations in the bulk but only with symmetry-allowed perturbations on the boundary [123]. Clearly, the relationship between the bulk and the boundary

contains interesting unanswered questions.

Lastly, all known single-shot stabilizer codes are self-correcting (but only exist in 4d or higher). None of the phases that we found in the ITC phase diagram are self-correcting. Can the simplified construction of the ITC offer any progress towards a new subsystem code that does include a self-correcting phase in 3d?

Chapter 5

Multipole Superfluids

We examine the hydrodynamics of systems with spontaneously broken multipolar symmetries using a systematic effective field theory. We focus on the simplest non-trivial setting: a system with charge and dipole symmetry, but without momentum conservation. When no symmetries are broken, our formalism reproduces the quartic subdiffusion ($\omega \sim -ik^4$) characteristic of ‘fracton hydrodynamics’ with conserved dipole moment. Our formalism also captures spontaneous breaking of charge and/or dipole symmetry. When charge symmetry is spontaneously broken, the hydrodynamic modes are quadratically propagating and quartically relaxing ($\omega \sim \pm k^2 - ik^4$). When the dipole symmetry is spontaneously broken but the charge symmetry is preserved, then we find quadratically relaxing (diffusive) transverse modes, plus another mode which depending on parameters may be either purely diffusive ($\omega \sim -ik^2$) or quadratically propagating and quadratically relaxing ($\omega \sim \pm k^2 - ik^2$). Our work provides concrete predictions that may be tested in near-term cold atom experiments, and also lays out a general framework that may be applied to study systems with spontaneously broken multipolar symmetries.

5.1 Introduction

Multipolar symmetries are exciting widespread interest in modern condensed matter physics, quantum information, and quantum dynamics. They connect to exotic ‘fracton’ phases of quantum matter [39, 103] and can provide a new route to ergodicity breaking [67, 98, 117]. Multipolar symmetries can display partial or complete spontaneous symmetry breaking (SSB), through which

they can stabilize new kinds of phases [74]. Of particular interest, the approach to equilibrium in systems with multipolar symmetries is described by hydrodynamics in an infinite family of non-standard universality classes [59, 92], collectively termed ‘fracton hydrodynamics.’ This ‘fracton hydrodynamics’—which has been realized in ultracold atoms [43]—provides an exciting new frontier, the exploration of which has become an important topic of research in its own right [28, 36–38, 41, 44, 48, 58, 95, 106, 111, 116].

The *thermodynamics* of SSB of multipolar symmetries has been discussed in [63, 124], where analogs of the Mermin-Wagner and Imry-Ma theorems were established. Different patterns of SSB, either of the entire multipole group or of its subgroups, correspond to condensing either monopole charges or higher multipole charges. We will call such SSB phases ‘fracton superfluids.’ The hydrodynamics of conventional superfluids is a well studied subject [105]—here, the Goldstone boson of the broken symmetry becomes a hydrodynamic mode. However, given the surprises attendant in the hydrodynamics of systems with unbroken multipolar symmetries, one might anticipate new features in hydrodynamics of fracton superfluids. By analogy, we may term the hydrodynamics of such generalized superfluids ‘fracton superfluid hydrodynamics.’ Previous literature has studied fracton superfluids at zero temperature [74, 140]. Other work has shown that multipolar symmetries and translation symmetry together lead to exotic hydrodynamics in which one symmetry *must* be spontaneously broken [38], by certain definitions of SSB; see also [62].

In this Letter, we develop the theory of fracton superfluid hydrodynamics at nonzero temperatures. We do so in the simplest possible setting—a system with only charge and dipole symmetry, leaving generalization to arbitrary multipole groups and/or momentum conservation to future work. For such charge and dipole conserving systems, we develop a systematic effective field theory description which yields three phases, roughly organized as in Fig. 5.1. One phase corresponds to the ‘fracton hydrodynamics’ of [40] with no symmetries broken. Another phase, with the symmetry fully broken, has been called the ‘fractonic superfluid’ [140] or the ‘Bose-Einstein insulator’ [74]. We will call it the ‘charge condensate’. Finally, the ‘dipole condensate’, with the dipole symmetry spontaneously broken and the monopole symmetry unbroken, exhibits new hydrodynamics. The

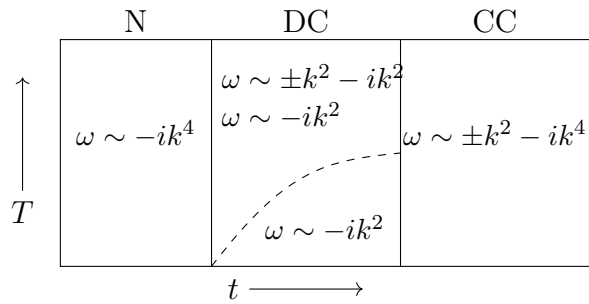


Figure 5.1: A rough organization of the three phases we find. The axes are temperature T and a generic hopping coefficient t that condenses dipole charges and monopole charges successively. The normal phase (N) displays subdiffusion while the charge condensate (CC) displays quadratically-propagating modes. The dipole condensate (DC) phase displays a crossover between only diffusive modes at small T and coexisting diffusive and propagating modes at large T .

two condensate phases are both fracton superfluids.

5.2 Effective action

We will use the recently-developed hydrodynamic effective field theory [24, 35, 46, 61, 81] to explore our hydrodynamic phases. To build the effective action for a system with charge and dipole conservation we will use the phase fields ϕ and ψ_i . The action should be invariant under global dipole transformations parametrized by arbitrary constants b and c_i , under which the fields transform as

$$\begin{aligned}\phi &\rightarrow \phi + b + x^k c_k, \\ \psi_i &\rightarrow \psi_i + c_i.\end{aligned}\tag{5.1}$$

The invariant objects are $\partial_t\phi$, $\partial_t\psi_i$, $\nabla_i\phi - \psi_i$, $\nabla_i\psi_j$, and $\nabla_i\nabla_j\phi$. Here ϕ is the ‘monopole’ field and ψ_i is the ‘dipole’ field, and the combination $\nabla_i\phi - \psi_i$ indicates that the motion of a monopole charge involves absorption (or emission) of a dipole. We notice that $\nabla_i\nabla_j\phi = \nabla_i(\nabla_j\phi - \psi_j) + \nabla_i\psi_j$, demonstrating that $\nabla_i\nabla_j\phi$ is a redundant degree of freedom.

Our most general Lagrangian is then

$$\mathcal{L} = \mathcal{L}(\partial_t\phi, \partial_t\psi_i, \nabla_i\phi - \psi_i, \nabla_i\psi_j).\tag{5.2}$$

From this, we can derive two Noether-like equations:

$$0 = \partial_t\rho + \nabla_i J_i,\tag{5.3}$$

$$0 = \partial_t\rho_i + J_i - \nabla_j J_{ij}\tag{5.4}$$

where we have defined

$$\begin{aligned}\rho &\equiv \frac{\partial \mathcal{L}}{\partial(\partial_t \phi)} & J_i &\equiv \frac{\partial \mathcal{L}}{\partial(\nabla_i \phi)} = -\frac{\partial \mathcal{L}}{\partial \psi_i} \\ \rho_i &\equiv \frac{\partial \mathcal{L}}{\partial(\partial_t \psi_i)} & J_{ij} &\equiv -\frac{\partial \mathcal{L}}{\partial(\nabla_j \psi_i)}\end{aligned}\tag{5.5}$$

as the densities and currents. We will call (5.3) the monopole continuity equation, and (5.4) the dipole continuity equation. To recognize (5.4) as dipole conservation, we can define the total dipole moment $d_i \equiv x_i \rho + \rho_i$ so that it obeys a continuity equation

$$0 = \partial_t d_i + \nabla_j J_{ij}^{(d)},\tag{5.6}$$

where $J_{ij}^{(d)} = x_i J_j - J_{ij}$.

In order to turn this into a hydrodynamic EFT, following [81], we must put the action on a doubled Schwinger-Keldysh contour, and define forward-propagating fields ϕ_1 and ψ_{i1} and backward-propagating fields ϕ_2 and ψ_{i2} on the two contours. In the hydrodynamic limit the forward and backward fields are close to equal so it easier to work with the “classical fields” $\phi = (\phi_1 + \phi_2)/2$, $\psi_i = (\psi_{i1} + \psi_{i2})/2$ and the “noise fields” $\Phi = \phi_1 - \phi_2$, $\Psi_i = \psi_{i1} - \psi_{i2}$.

The full hydrodynamic Lagrangian will have the form

$$\mathcal{L}_{\text{eff}} = \rho \partial_t \Phi + \rho_i \partial_t \Psi_i + J_i (\nabla_i \Phi - \Psi_i) - J_{ij} \nabla_j \Psi_i,\tag{5.7}$$

where the densities and currents may depend on ϕ , ψ_i , Φ , and Ψ_i . We have no terms with $\nabla_i \nabla_j \Phi$ for the same reason we have no terms involving $\nabla_i \nabla_j \phi$ in (5.2): such terms can be converted into the terms already present in (5.7). For details, see the Appendix.

The action $I[\phi, \Phi, \psi_i, \Psi_i] = \int d^3x dt \mathcal{L}_{\text{eff}}$ must be symmetric under

$$\begin{aligned} \phi &\rightarrow \phi + b + x^k c_k, & \psi_i &\rightarrow \psi_i + c_i, \\ \Phi &\rightarrow \Phi + b' + x^k c'_k, & \Psi_i &\rightarrow \Psi_i + c'_i, \end{aligned} \tag{5.8}$$

which are independent dipole transformations for the classical and noise fields. We can see that the hydrodynamic variables in (5.7) are the currents for the transformations of the noise fields.

Furthermore, the action must satisfy the EFT symmetries [81],

$$\begin{aligned} I^*[\phi, \Phi, \psi_i, \Psi_i] &= -I[\phi, -\Phi, \psi_i, -\Psi_i], \\ I[\phi, \Phi = 0, \psi_i, \Psi_i = 0] &= 0, \\ \text{Im } I[\phi, \Phi, \psi_i, \Psi_i] &\geq 0, \end{aligned} \tag{5.9}$$

which can be derived from the full Schwinger-Keldysh formalism. It also must satisfy the KMS symmetry

$$\begin{aligned} \phi(x, t) &\rightarrow -\phi(x, -t), \\ \Phi(x, t) &\rightarrow -\Phi(x, -t) - i\beta \partial_t \phi(x, -t), \\ \psi_i(x, t) &\rightarrow -\psi_i(x, -t), \\ \Psi_i(x, t) &\rightarrow -\Psi_i(x, -t) - i\beta \partial_t \psi_i(x, -t), \end{aligned} \tag{5.10}$$

which is a consequence of the fact that our hydrodynamic EFT describes relaxation toward an equilibrium thermal state $e^{-\beta H}$; similar ideas hold for more general steady state [44].

Lastly, we have the option of enforcing the “diagonal shift symmetries” [81]. These symmetries require that the action only depend on ϕ through $\partial_t \phi$, or only depend on ψ_i through $\partial_t \psi_i$. In ordinary fluids, the EFT in the presence of the diagonal shift symmetry describes the normal phase, while the EFT in the absence of the diagonal shift symmetry describes superfluidity. Thus,

condensed degrees of freedom need not obey the diagonal shift symmetry, while normal degrees of freedom must.

5.3 Hydrodynamic phases

We will approach the hydrodynamics by imposing the diagonal shift symmetries for each phase independently, and then finding the lowest-order action in that phase. To count scaling dimensions, we note that ψ_i must scale as $\nabla_i \phi$ in order to preserve the dipole symmetry. First, we will impose the diagonal shift symmetry on both ϕ and ψ_i . This should describe the normal phase, with no condensation. If we suppose that the dynamical scaling exponent is $z = 4$, the most general effective action consistent with the KMS and EFT symmetries is

$$\begin{aligned} \mathcal{L}_{\text{eff}} = & \chi \partial_t \phi \partial_t \Phi + [-\sigma \partial_t (\nabla_i \phi - \psi_i)] (\nabla_i \Phi - \Psi_i) \\ & - [B_1 \partial_t \nabla_i \nabla_j \phi + B_2 \partial_t \nabla_i \psi_j + B_3 \partial_t \nabla_j \psi_i] \nabla_j \Psi_i, \end{aligned} \quad (5.11)$$

to leading order. All coefficients must be positive, by a combination of the KMS and EFT symmetries and thermodynamic stability. We have named χ and σ in reference to ordinary systems. Although χ is the susceptibility, σ does not play the role of a measurable electrical conductivity.

The density and currents are, at leading order:

$$\begin{aligned} \rho &= \chi \partial_t \phi \\ \rho_i &= 0 \\ J_i &= -\sigma \nabla_i \partial_t \phi + \sigma \partial_t \psi_i \\ J_{ij} &= B_1 \nabla_i \nabla_j \partial_t \phi + B_2 \nabla_i \partial_t \psi_j + B_3 \nabla_j \partial_t \psi_i. \end{aligned} \quad (5.12)$$

Although ρ_i has nonzero contributions at higher order, we will not need to include them. The dipole

continuity equation reads

$$\begin{aligned} 0 = & -\sigma \nabla_i \partial_t \phi + \sigma \partial_t \psi_i - B_1 \nabla^2 \nabla_i \partial_t \phi \\ & - B_2 \nabla_i \nabla_j \partial_t \psi_j - B_3 \nabla^2 \partial_t \psi_i \end{aligned} \quad (5.13)$$

which imposes that $\partial_t \psi_i = \nabla_i \partial_t \phi$, plus higher-order corrections. The monopole continuity equation then reads

$$\begin{aligned} 0 = & \partial_t \rho - \partial_t \nabla_i \rho_i + \nabla_i \nabla_j J_{ij} \\ = & \chi \partial_t^2 \phi + (B_1 + B_2 + B_3) \nabla^4 \partial_t \phi + \dots , \end{aligned} \quad (5.14)$$

so that the dispersion is

$$\omega = -i \frac{B_1 + B_2 + B_3}{\chi} k^4, \quad (5.15)$$

which describes subdiffusion. This is consistent with previous results [40], and also with experiments on cold atomic gases with approximate dipole symmetry [43].

For the remaining phases we will presciently suppose $z = 2$. Then, the most general effective action consistent with the KMS and EFT symmetries, but without any diagonal shift symmetries imposed, is

$$\begin{aligned} \mathcal{L}_{\text{eff}} = & \chi \partial_t \phi \partial_t \Phi \\ & + [-\kappa_1^\phi (\nabla_i \phi - \psi_i) + \kappa_2^\phi \nabla^2 \nabla_i \phi + g_2 \nabla^2 \psi_i \\ & + g_3 \nabla_i \nabla_j \psi_j - \sigma \partial_t (\nabla_i \phi - \psi_i)] (\nabla_i \Phi - \Psi_i) \\ & - [\kappa^{\phi\psi} \nabla_i \nabla_j \phi + \kappa_1^\psi \nabla_i \psi_j + \kappa_2^\psi \nabla_j \psi_i] \nabla_j \Psi_i, \end{aligned} \quad (5.16)$$

to leading order. The κ coefficients act as generalized superfluid stiffnesses in the system. The symmetries require that all coefficients except g_2 , and g_3 are positive. Furthermore, $\kappa^{\phi\psi} = \kappa_2^\phi + g_2 + g_3$

by KMS (see Appendix). This action should describe the charge condensate. Under these conditions, all terms in the effective action are allowed and the density and currents are

$$\begin{aligned}\rho &= \chi \partial_t \phi \\ \rho_i &= 0 \\ J_i &= -\kappa_1^\phi \nabla_i \phi + \kappa_1^\phi \psi_i + \dots \\ J_{ij} &= \kappa^{\phi\psi} \nabla_i \nabla_j \phi + \kappa_1^\psi \nabla_i \psi_j + \kappa_2^\psi \nabla_j \psi_i,\end{aligned}\tag{5.17}$$

to leading order. The dipole continuity equation now imposes that $\psi_i = \nabla_i \phi$ plus higher-order corrections. The monopole continuity equation is

$$\begin{aligned}0 &= \partial_t \rho - \partial_t \nabla_i \rho_i + \nabla_i \nabla_j J_{ij} \\ &= \chi \partial_t^2 \phi + (\kappa^{\phi\psi} + \kappa_1^\psi + \kappa_2^\psi) \nabla^4 \phi + \dots,\end{aligned}\tag{5.18}$$

so that the dispersion is

$$\omega^2 = \frac{\kappa^{\phi\psi} + \kappa_1^\psi + \kappa_2^\psi}{\chi} k^4,\tag{5.19}$$

which describes a propagating mode with $\omega \sim k^2$. Going beyond leading order, including generic dissipative terms such as $\partial_t \nabla_i \psi_j \nabla_i \Psi_j$ in the action contributes a subleading $-ik^4$ to the dispersion.

The quadratic propagation matches previous expectations at $T = 0$ from a microscopic model [140], field theory [124], and a more generic model called the Dipolar Bose-Hubbard Model (DBHM) [74], so that the charge condensate behaves like a zero-temperature fluid. The effects of dissipation are subleading and do not modify the zero-temperature behavior at low wavevector. In Ref. [74], the authors show that the existence of only a single mode in the charge condensate phase of the DBHM is a result of a Higgs-like effect. The same effect appears in the hydrodynamics as the requirement that $\psi_i = \nabla_i \phi$.

Finally, we can try imposing the diagonal shift symmetry on ϕ but not ψ_i . This corresponds to the dipole condensate, where dipole symmetry is spontaneously broken but monopole symmetry is not. The diagonal shift symmetry on ϕ requires that κ_1^ϕ , κ_2^ϕ , and $\kappa^{\phi\psi}$ vanish, which in turn requires that $g_3 = -g_2$. The density and currents are

$$\begin{aligned}\rho &= \chi \partial_t \phi \\ \rho_i &= 0 \\ J_i &= g_2(\nabla^2 \psi_i - \nabla_i \nabla_j \psi_j) - \sigma \nabla_i \partial_t \phi + \sigma \partial_t \psi_i \\ J_{ij} &= \kappa_1^\psi \nabla_i \psi_j + \kappa_2^\psi \nabla_j \psi_i.\end{aligned}\tag{5.20}$$

The dipole continuity equation will no longer result in a constraint because now J_i and $\nabla_j J_{ij}$ are of the same order. Instead, we will have to simultaneously solve both equations.

The two continuity equations are

$$\begin{aligned}0 &= \chi \partial_t^2 \phi - \sigma \nabla^2 \partial_t \phi + \sigma \partial_t \nabla_i \psi_i, \\ 0 &= -\sigma \nabla_i \partial_t \phi + \sigma \partial_t \psi_i - (\kappa_2^\psi - g_2) \nabla^2 \psi_i \\ &\quad - (\kappa_1^\psi + g_2) \nabla_i \nabla_j \psi_j.\end{aligned}\tag{5.21}$$

We can simplify the analysis by splitting ψ_i into a transverse and longitudinal part $\psi_i = \psi_i^t + \psi_i^\ell$ where the longitudinal part is $\psi_i^\ell = k_i k_j / k^2 \psi_j$ and obeys $\nabla_i \psi_i^\ell = \nabla_i \psi_i$. The transverse part is $\psi_i^t = P_t \psi_i$ where $P_t = (\delta_{ij} - k_i k_j / k^2)$ is the transverse projector. Applying the transverse projector to the dipole continuity equation results in

$$0 = \sigma \partial_t \psi_i^t - (\kappa_2^\psi - g_2) \nabla^2 \psi_i^t,\tag{5.22}$$

with solution

$$\omega = -i\frac{\kappa_2^\psi - g_2}{\sigma} k^2, \quad (5.23)$$

which is an ordinary diffusive mode. Note that the value $\kappa_2^\psi - g_2$ is always positive (see Appendix). Furthermore, this dispersion represents two hydrodynamic modes, corresponding to the two transverse polarizations of ψ_i .

To access the longitudinal part we may take the divergence of the dipole continuity equation. The monopole continuity equation and the divergence of the dipole continuity equation together read

$$0 = \begin{bmatrix} \chi\partial_t - \sigma\nabla^2 & \sigma\partial_t \\ -\sigma\nabla^2 & \sigma\partial_t - \kappa^\psi\nabla^2 \end{bmatrix} \begin{pmatrix} \partial_t\phi \\ \nabla_j\psi_j \end{pmatrix}, \quad (5.24)$$

where $\kappa^\psi = \kappa_1^\psi + \kappa_2^\psi$, showing that ϕ and $\nabla_i\psi_i$ are coupled. Their joint dispersion relation is

$$0 = \omega^2 + i\frac{\kappa^\psi}{\sigma}\omega k^2 - \frac{\kappa^\psi}{\chi}k^4, \quad (5.25)$$

or

$$\omega = -i\frac{\kappa^\psi}{2\sigma}k^2 \pm \sqrt{\frac{-(\kappa^\psi)^2}{4\sigma^2} + \frac{\kappa^\psi}{\chi}k^2}, \quad (5.26)$$

which displays a crossover from pure diffusion to quadratic propagation, controlled by the dimensionless parameter $\kappa^\psi\chi/\sigma^2$. For $\kappa^\psi\chi \gg 4\sigma^2$, the dispersion approaches

$$\omega = -i\frac{\kappa^\psi}{\sigma}k^2, \quad \omega = -i\frac{\sigma}{\chi}k^2, \quad (5.27)$$

with two quadratically diffusing modes. In the opposite limit the dispersion approaches

$$\omega = -i \frac{\kappa^\psi}{2\sigma} k^2 \pm \sqrt{\frac{\kappa^\psi}{\chi} k^2}, \quad (5.28)$$

which is simultaneously quadratically propagating and quadratically diffusive. While we might have expected the dissipative coefficient σ to play a damping role, the large- σ regime is underdamped and the small- σ regime is overdamped.

5.4 Exploring the dipole condensate

Since the subdiffusion of the normal phase and quadratic propagation of the charge condensate already exist in the literature, we can focus on understanding the dipole condensate better. We can tune various parameters to be small, bringing us to limiting points of the phase diagram. The small parameters define a *quasihydrodynamic* timescale τ [42], which is parametrically long.

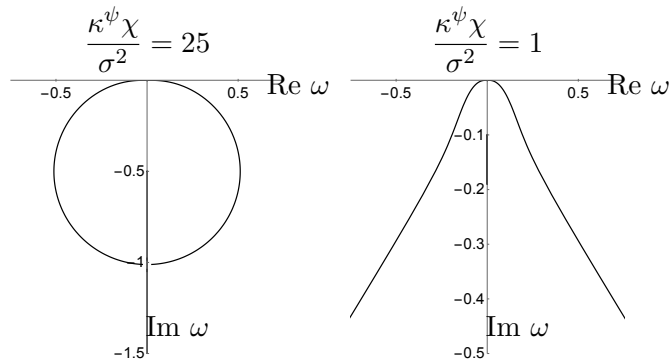


Figure 5.2: Parametric plot of the dispersion in the charge condensate but close to the dipole condensate. The left figure is plotted near the diffusive regime of the dipole condensate ($\kappa^\psi \chi / \sigma^2 = 25$) while the right figure is plotted near the propagating regime of the dipole condensate ($\kappa^\psi \chi / \sigma^2 = 1$). At small k both dispersions look like the charge condensate while at large k they look like their respective DC dispersions.

In particular, let us study the hydrodynamics in the charge condensate but near the transition to the dipole condensate. We allow terms that break the diagonal shift symmetry for ϕ , but require them to be small. This defines the quasihydrodynamic timescale $\tau = \sigma / \kappa_1^\phi$ (see Appendix for more details). Furthermore, we must choose the dimensionless parameter $\kappa^\psi \chi / \sigma^2$ to place us on either

side of the crossover in the dipole condensate. The resulting dispersion relation is shown in Fig. 5.2. For details, see the Appendix.

Another surprising facet of the phase is its quadratic propagation. At $T = 0$ in the DBHM, the dipole condensate consists of d modes (one for each space dimension), all propagating linearly [74, 124]. We can treat the hydrodynamic phase explored here as consisting of both the dipole condensate and a background normal (subdiffusive) fluid. Although the hydrodynamics EFT does not provide a mechanism for studying the behavior of the fluid as $T \rightarrow 0$, we can instead see that we can reproduce the $T = 0$ behavior in the nondissipative limit $\sigma \rightarrow 0$. The dispersion at small σ is in Fig. 5.3 (see Appendix for details). In contrast to the charge condensate, where dissipation had little effect on the physics, in the dipole condensate the mode propagation at low wavenumber is immediately modified in the presence of dissipation.

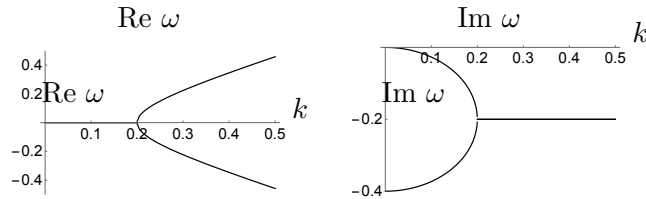


Figure 5.3: Real and imaginary parts of the dispersion in the dipole condensate phase close to the dissipationless limit. At small k the dispersion looks like the diffusive regime of the dipole condensate ($\omega \sim -ik^2$) while at large k it looks like the $T = 0$ limit of the dipole condensate ($\omega \sim \pm k$).

5.5 Discussion

Real and imaginary parts of the dispersion in the dipole condensate phase close to the dissipationless limit We have developed a systematic, effective field theory based treatment of hydrodynamics in systems with charge and dipole symmetry, allowing for the possibility of spontaneous symmetry breaking. In the absence of any SSB, we find quartic subdiffusion, consistent with [40]. With both charge and dipole symmetries broken, we find a quadratically propagating (and quartically subdiffusing) mode, consistent with [74]. We also introduced the phase where dipole symmetry is spontaneously broken but monopole symmetry is preserved, corresponding to a ‘dipole condensate.’

In this phase we find that there exist diffusive transverse modes, as well as longitudinal modes which depending on parameters can be either purely diffusive, or quadratically propagating and relaxing. This phase does not match any in the literature, and reflects intrinsically-nonzero-temperature effects.

Our results can be tested in ultracold atom experiments analogous to [43]. Further afield, they could be generalized to systems with momentum conservation and/or systems with more complex multipolar symmetries [16]. We leave such generalizations to future work.

Chapter 6

Robust shattering

We present a set of generalized quantum loop models which provably exhibit topologically stable ergodicity breaking. These results hold for both periodic and open boundary conditions, and derive from a one-form symmetry (notably not being restricted to sectors of extremal one-form charge). We identify simple models in which this one-form symmetry can be emergent, giving rise to the aforementioned ergodicity breaking as an exponentially long-lived prethermal phenomenon. We unveil a web of dualities that connects these models, in certain limits, to models that have previously been discussed in the literature. We also identify nonlocal conserved quantities in such models that correspond to a pattern of system-spanning domain walls, and which are robust to the addition of arbitrary k -local perturbations.

6.1 Introduction

When can many-body quantum systems fail to reach thermal equilibrium under their own dynamics, and thereby exhibit long-time behavior that lies fundamentally beyond equilibrium quantum statistical mechanics? The oldest answer to this question is “when they are integrable” [6]—integrable systems have extensively many explicit conservation laws, and do not thermalize to any conventional statistical mechanical ensemble. However, it is unclear to what extent (if at all) integrability is robust to generic perturbations, in the thermodynamic limit. A more recent answer is “when they are many-body localized” [3, 91]. Many-body localization by strong disorder involves extensively many emergent conservation laws, and does exhibit robustness to spatially

local perturbations, although the proof of robustness is limited to one-dimensional spin chains [60], and moreover is subtle and has been questioned [119]. Quantum many-body scars [20, 90, 121, 129] provide yet another example, without any conservation laws (but generically also without any notion of robustness). Still more recently, it was realized that the interplay of finitely many ‘multipolar’ conservation laws could break ergodicity [98], a result that was explained in terms of a shattering (aka fragmentation) of Hilbert space [67, 89, 117], whereby the unitary time evolution matrix block diagonalizes (within each symmetry sector) into exponentially many dynamically disconnected subsectors. This phenomenon has a simple proof of robustness [67] to arbitrary symmetric perturbations with strict spatial locality, and has stimulated a great deal of work into quantum dynamics with multipolar symmetries [16, 28, 36–38, 40, 41, 44, 48, 49, 58, 59, 68, 88, 95, 106, 108, 111, 116, 138, 139].

Very recently, a new route to ergodicity breaking was identified [126] which exhibits *topological* stability in two spatial dimensions. For the first time, the ergodicity breaking is robust to spatially *nonlocal* perturbations, with the only requirement being that of *k-locality*, i.e., that the perturbation should act on no more than k degrees of freedom (with $k/L \rightarrow 0$ in the thermodynamic limit, where L is linear system size). This argument relied on a one-form symmetry, with the results being exact in the presence of arbitrary one-form-symmetric k -local perturbations. It was also explained how the one-form symmetry could be ‘emergent’ in a simple model of spin-1/2 degrees of freedom, which we hereafter refer to as the CZ _{p} model, in which case the ergodicity breaking became prethermal, and robust to arbitrary k -local perturbations up to exponentially long timescales. However, the results of Ref. [126] relied on a *dense packing of system winding loops*, such that the ergodicity breaking only arose in sectors of extremal one-form symmetry charge, and was ‘all or nothing’ (i.e., either the one-form symmetry sector was shattered into fully frozen one-dimensional subblocks with no dynamics, or it was not fragmented at all). Moreover, the construction presented in Ref. [126] was limited to systems with periodic boundary conditions.

In this work, we drastically extend the results of Ref. [126] to a much broader class of quantum loop models, without the requirement of either dense packing or periodic boundary conditions.

We present a family of simple models with emergent one-form symmetry [22, 33, 73, 83, 94] (up to an exponentially long prethermal timescale). This family of models includes, as its simplest member, the CZ_p model of Ref. [126]. We show how this family of models generically exhibits ergodicity breaking with topological stability, and how the results may be extended to systems with open boundary conditions. Moreover, the broader family includes models in which the ergodicity breaking occurs in all symmetry sectors, and is not ‘all or nothing’ (i.e., symmetry sectors can block diagonalize into subblocks that are not one-dimensional). In this latter case, we identify certain nonlocal conserved quantities that robustly label the emergent subblocks. We also unveil a web of dualities that connects our results (in various limits) to higher-dimensional generalizations of several models previously considered in the literature, including the pair-flip model [18, 88], and which also make a connection with (quantum) square ice [78, 86, 120] and close-packed dimer models [29, 53, 54, 64, 65, 87, 115, 127].

The manuscript is structured as follows: We start with a review of the one-dimensional pair-flip model in Sec. 6.2. This discussion serves as a warm-up and emphasizes the aspects of the model that will be most useful in our two-dimensional generalization. Readers familiar with the physics of the one-dimensional pair-flip model can therefore skip to Sec. 6.3, where we introduce a two-dimensional model that displays the aforementioned topological fragmentation. Sec. 6.3.1 contains a summary of the two-dimensional model that is meant to be entirely self-contained, so that readers may understand all the physics of the topological fragmentation. The rest of that section is devoted to details of the model, including its boundaries, symmetries, robustness, and fragmentation. In Sec. 6.4 we provide connections to square ice, the CZ_p model [126] (via a Kramers-Wannier-like duality), and a three-dimensional generalization. Finally, we discuss some open questions in Sec. 6.5.

6.2 Warm-up: One-dimensional pair-flip dynamics

We start with a brief review of the dynamics of the one-dimensional (1D) pair-flip (PF) model [18, 88], which exhibits some properties that will be useful for understanding our generalized quantum loop models. Readers familiar with the pair-flip model may safely skip this section and

begin reading Sec. 6.3.

Consider a lattice composed of L spin- S degrees of freedom on the edges of a one-dimensional lattice. It will be convenient to work with the variable $m = 2S + 1$ in place of S ; each degree of freedom is then associated to an m -dimensional local Hilbert space. Let us introduce the following graphical representation of states,

$$|0\rangle \equiv |\bullet\rangle, |1\rangle \equiv |\circlearrowleft\rangle, |2\rangle \equiv |\circlearrowright\rangle, \quad (6.1)$$

where we have set $m = 3$ for convenience of illustrations.

Given projectors $\hat{\mathcal{P}}_e^\alpha = |\alpha\rangle\langle\alpha|_e$ that project the spin at edge e onto state α , we may define the symmetry charges

$$\hat{N}^\alpha = \sum_e (-1)^e \hat{\mathcal{P}}_e^\alpha, \quad \alpha = 0, \dots, m-1, \quad (6.2)$$

where $(-1)^e = 1$ if e is in the even sublattice and $(-1)^e = -1$ if e is in the odd sublattice. While it may appear that there are m different generators in (6.2), only $m-1$ of them are independent since the projectors obey $\sum_{\alpha=0}^{m-1} \hat{\mathcal{P}}_e^\alpha = \mathbb{1}$ on every edge. The $U(1)^{m-1}$ symmetry (6.2) breaks the m^L -dimensional Hilbert space into $\mathcal{O}(L^{m-1})$ symmetry sectors. However, as we will show, following the discussion in Ref. [88], nearest-neighbor, symmetry-respecting dynamics is not fully ergodic within these sectors.

The most generic nearest-neighbor dynamics consistent with (6.2) is as follows: If the spins on edges e and $e+1$ are both in state α , flip them both to state β , with $0 \leq \alpha, \beta \leq m-1$. These “active” pairs can be represented by pairing up the legs emanating from spins into “dimers.” For example,

$$|\bullet \bullet\rangle \rightarrow |\bullet-\bullet\rangle, \quad (6.3)$$

and with analogous notation for neighboring pairs of green and blue sites. Consider the following configurations:

$$|\bullet-\bullet \bullet-\bullet\rangle, \quad |\bullet-\bullet \bullet-\bullet\rangle. \quad (6.4)$$

The configuration on the left is evidently fully active. The configuration on the right is also fully active since the central active red pair can be permuted to green, allowing the green edge spins to become active. In this way, the two configurations are actually connected via local pair-flip moves. Indeed, since any contiguous region of $2n$ spins paired into n noncrossing dimers can be connected via local moves to the all red state (say), *any* configuration of n noncrossing dimers can be generated via pair-flip moves.

Suppose that the following procedure is performed: First, all neighboring pairs are grouped¹ according to Eq. (6.3). Next, all paired spins are removed from the string, and the pairing procedure is applied again to the remaining spins. This procedure is repeated until there remains a configuration of unpaired spins that cannot be paired up without introducing crossings between dimers.

Having completed this procedure, observe that unpaired spins are able to move past paired spin configurations.² The simplest example of this being

$$|\bullet \text{---} \bullet\rangle \leftrightarrow |\bullet \text{---} \bullet\rangle \leftrightarrow |\bullet \text{---} \bullet\rangle \leftrightarrow |\bullet \text{---} \bullet\rangle . \quad (6.5)$$

However, since the color of the unpaired spin remains fixed, the ternary string corresponding to the unpaired dots (i.e., having removed all intervening paired spins) is conserved. As an explicit example, under the procedure just described,

$$|\bullet \text{---} \bullet \text{---} \bullet \text{---} \bullet \text{---} \bullet \text{---} \bullet \text{---} \bullet\rangle \mapsto |\bullet \text{---} \bullet\rangle . \quad (6.6)$$

The reduced pattern shown on the right-hand side is conserved under pair-flip dynamics. Note that we are assuming open boundaries for the purposes of this discussion.

We call such a pattern of unpaired dots a *label*; spin configurations associated to different labels cannot be connected via pair-flip dynamics and therefore belong to dynamically disconnected

¹While this grouping is not unique, the nonuniqueness does not affect the label that the procedure produces.

²The hopping process however preserves the sublattice of the unpaired spin. This leads to additional conservation laws for periodic boundaries and even L , described in Appendix C.2.

sectors known as Krylov sectors [89]. If our system has an even (odd) number of spins then the label must have an even (odd) length, but can otherwise be any length between 0 and L . For open boundary conditions, the first color in the label is arbitrary and no color may match its neighbor, so there are $m(m - 1)^{j-1}$ labels of length j , except for the trivial label ($j = 0$) of which there is only one (and only exists if L is even). In all, this allows for

$$\sum_{n=0}^{\lceil L/2 \rceil - 1} m(m - 1)^{L-2n-1} + (1 \text{ if } L \text{ is even}) = \mathcal{O}[(m - 1)^L] \quad (6.7)$$

Krylov sectors. See Appendix C.2 for the sizes of the Krylov sectors, and for the slightly different counting of sectors in the presence of periodic boundaries. The exponential scaling of the number of Krylov sectors together with the polynomial scaling of the number of symmetry sectors means that the PF model must exhibit fragmentation [88]. In particular, Krylov sectors with labels of length L each consist of one fully frozen state with no allowed dynamics.

Furthermore, fragmentation exists in generic symmetry sectors. Any symmetry sector has a minimal length L_{\min} on which it exists. Take a representative spin pattern from that sector and an uncharged motif such as $|\color{red}\bullet\color{black} \color{green}\bullet\color{black} \color{blue}\bullet\color{black} \color{red}\bullet\color{black} \color{green}\bullet\color{black} \color{blue}\bullet\color{black}\rangle$. There are six motifs of size six (and no smaller motifs, as shown in Appendix C.2) but only four have a first spin that does not match the last spin of our chosen pattern. Then for systems of size $L_{\min} + 6n$, we have n slots into which we can independently place four compatible patterns, which gives a lower bound of $4^{(L-L_{\min})/6}$ different Krylov sectors within any fixed symmetry sector. A more detailed count of the number of Krylov sectors belonging to each symmetry sector is given in Appendix C.2, but the argument here is enough to show that fragmentation is present in generic symmetry sectors.

In the pair-flip model, and in most models in the literature, fragmentation depends strongly on strict locality. In our example, we can see this to be true by including next-nearest-neighbor dynamics. Any move that swaps the states of the spins on edges $e - 1$ and $e + 1$ is allowed by the symmetry (6.2). Under this dynamics, any two states within the same symmetry sector may be transformed into each other, regardless of their label as previously defined, completely melting the

fragmentation. In the next section we will introduce a two-dimensional (2D) model with similar fragmentation properties, but where arbitrary k -local terms ($k < 2L$) may be introduced while preserving the fragmentation—the extra dimension (and attendant one-form symmetry) endows the fragmentation with topological stability.

6.3 The quad-flip model

We now define the quad-flip model, a generalization of the PF model to 2D. Reference [88] shows that the simplest generalization of PF dynamics to 2D, using a 0-form symmetry, results in fragmentation that is not robust to generic local perturbations. Reference [126] shows that 1-form symmetries can lead to robust fragmentation. This motivates our generalization of the PF model to 2D using a 1-form symmetry.

6.3.1 Summary

We will first present a general overview of how generalized 2D loop models can exhibit robust Hilbert space fragmentation without reference to any particular Hamiltonian realization. Explicit local Hamiltonians that give rise to the desired loop models prethermally, and a more technical discussion of their conventional symmetries and nonlocal conserved quantities, are presented from Sec. 6.3.3 onwards.

Consider an $L \times L$ square lattice in two spatial dimensions with spin- S degrees of freedom on the edges of the lattice. As in Sec. 6.2, we introduce the variable $m = 2S + 1$ to parameterize the size of the local Hilbert space on each edge. The states on each edge are given the following graphical representation

$$|0\rangle \equiv |\bullet\rangle, |1\rangle \equiv |\circlearrowleft\rangle, |2\rangle \equiv |\circlearrowright\rangle, \dots \quad (6.1)$$

where we have set $m = 3$ for convenience of illustrations.

We can define a 1-form symmetry in 2D analogous to the symmetry from Sec. 6.2. In general, n -form symmetries consist of operators defined on $(d - n)$ -dimensional manifolds [22, 33, 73, 83, 94].

For any path \mathcal{C} on the lattice (with a definite starting edge), define the one-form symmetry charges

$$\hat{N}_{\mathcal{C}}^{\alpha} = \sum_{e_j \in \mathcal{C}} (-1)^j \hat{\mathcal{P}}_{e_j}^{\alpha}, \quad \alpha = 0, \dots, m-1, \quad (6.8)$$

where the edges $\{e_0, e_1, \dots\}$ in \mathcal{C} are ordered so that e_{j+1} follows e_j when following the path. Changing the numbering on the edges may send $\hat{N}_{\mathcal{C}}^{\alpha}$ to $-\hat{N}_{\mathcal{C}}^{\alpha}$, but will otherwise leave the operator unchanged. For any \mathcal{C} consisting of $|\mathcal{C}|$ edges, the operators are not all independent, obeying $\sum_{\alpha=0}^{m-1} \hat{N}_{\mathcal{C}}^{\alpha} = 0$ for $|\mathcal{C}|$ even or $\mathbb{1}$ for $|\mathcal{C}|$ odd. Any contractible path on the square lattice has $|\mathcal{C}|$ even.

Let us restrict to states that are source free³ so that $\hat{N}_{\partial\mathcal{R}}^{\alpha} = 0$ for any region \mathcal{R} of the lattice. In particular, the region may be chosen to be a single face, which only permits configurations of the form

$$\left| \begin{array}{c} \text{red dot} \\ \text{blue dot} \\ \text{green dot} \end{array} \right\rangle, \quad \left| \begin{array}{c} \text{red dot} \\ \text{blue dot} \\ \text{green dot} \end{array} \right\rangle, \quad \left| \begin{array}{c} \text{red dot} \\ \text{blue dot} \\ \text{green dot} \end{array} \right\rangle, \quad (6.9)$$

along with configurations related to these by interchanging colors. The graphical representation we have utilized makes it clear that spins of a given color must therefore form unbroken loops, and that loops of differing colors cannot intersect with one another. The allowed Hilbert space does not have a tensor-product structure, but is still exponential in system volume L^2 . Consequently, there is room for a properly extensive entropy, and it makes sense to talk about thermalization or lack thereof. In Sec. 6.3.3 we show the constrained Hilbert space dimension grows as $\sim W_m^{L^2}$, with $W_m \gtrsim \max[(2m-1)/m, \sqrt{m}]$, in contrast to the m^{2L^2} growth of the unconstrained Hilbert space.

The nontrivial operators are those defined on noncontractible paths. These operators measure the symmetry charges. We will explore the compatibility constraints between the charges, and therefore the number of symmetry sectors, in Sec. 6.3.4. For now it is enough to say that this symmetry breaks the constrained Hilbert space into $\mathcal{O}(L^{m-1})$ symmetry sectors, as in the pair-flip model. However, as in the pair-flip model, dynamics within the constrained Hilbert space is not fully ergodic within these sectors, and this time the ergodicity breaking is topologically robust.

³Violations of this constraint are sources in a U(1) lattice gauge theory interpretation of this model for $m = 2$. We continue to use this language analogously for $m > 2$. Within the source-free subspace the 1-form symmetry is topological [107] (a.k.a. relativistic [118]).

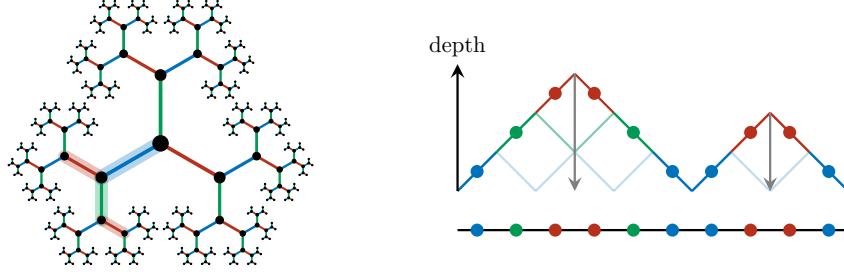


Figure 6.1: Left: Bethe lattice that can be used to define a height profile for the $m = 3$ loop model. Right: mapping of a one-dimensional cut of the square lattice to a colored Dyck path, where the height is determined by the depth of the corresponding position on the Bethe lattice. The corresponding edges have been highlighted on the Bethe lattice.

We now examine generic k -local dynamics compatible with the local constraint (6.9). On a given face of the lattice, a minimum of two spins must be flipped to preserve the constraint. These two spins must have the same color, otherwise the constraint will be violated via the introduction of a forbidden loop crossing:

$$\left| \begin{array}{c} \textcolor{red}{\bullet} \\ \textcolor{blue}{\bullet} \\ \textcolor{blue}{\bullet} \end{array} \right\rangle \xrightarrow{\checkmark} \left| \begin{array}{c} \textcolor{green}{\bullet} \\ \textcolor{blue}{\bullet} \\ \textcolor{blue}{\bullet} \end{array} \right\rangle, \quad \left| \begin{array}{c} \textcolor{red}{\bullet} \\ \textcolor{blue}{\bullet} \\ \textcolor{blue}{\bullet} \end{array} \right\rangle \xrightarrow{\times} \left| \begin{array}{c} \textcolor{red}{\bullet} \\ \textcolor{red}{\bullet} \\ \textcolor{red}{\bullet} \end{array} \right\rangle. \quad (6.10)$$

Applying the left-hand transition in (6.10) to the four faces around a vertex gives rise to the minimal update (i.e., acting on the fewest possible spins) to the system compatible with the constraint: the four spins on the edges surrounding a vertex can simultaneously be flipped only if their colors match:

$$\left| \begin{array}{ccccc} \textcolor{blue}{\bullet} & \textcolor{blue}{\bullet} & \textcolor{red}{\bullet} & \textcolor{blue}{\bullet} & \textcolor{blue}{\bullet} \\ \textcolor{blue}{\bullet} & \textcolor{red}{\bullet} & \textcolor{red}{\bullet} & \textcolor{blue}{\bullet} & \textcolor{blue}{\bullet} \\ \textcolor{red}{\bullet} & \textcolor{red}{\bullet} & \textcolor{red}{\bullet} & \textcolor{blue}{\bullet} & \textcolor{blue}{\bullet} \\ \textcolor{blue}{\bullet} & \textcolor{blue}{\bullet} & \textcolor{blue}{\bullet} & \textcolor{blue}{\bullet} & \textcolor{blue}{\bullet} \end{array} \right\rangle \xrightarrow{\checkmark} \left| \begin{array}{ccccc} \textcolor{blue}{\bullet} & \textcolor{blue}{\bullet} & \textcolor{green}{\bullet} & \textcolor{blue}{\bullet} & \textcolor{blue}{\bullet} \\ \textcolor{blue}{\bullet} & \textcolor{red}{\bullet} & \textcolor{red}{\bullet} & \textcolor{blue}{\bullet} & \textcolor{blue}{\bullet} \\ \textcolor{red}{\bullet} & \textcolor{red}{\bullet} & \textcolor{red}{\bullet} & \textcolor{blue}{\bullet} & \textcolor{blue}{\bullet} \\ \textcolor{blue}{\bullet} & \textcolor{blue}{\bullet} & \textcolor{blue}{\bullet} & \textcolor{blue}{\bullet} & \textcolor{blue}{\bullet} \end{array} \right\rangle, \quad (6.11)$$

This update thereby modifies the color of the smallest closed loop configurations in the system, which are “active” in the same sense as the active pairs in 1D. This minimal update is a natural two-dimensional extension of the pair-flip dynamics discussed in Sec. 6.2. Hence, we refer to such updates as *quad-flip* (QF) dynamics.

QF dynamics can also change the color of any contractible loop. In fact, any two source-free states that differ from each other inside a contractible loop of a single color can be connected via

a sequence of quad flips (6.11). To justify this statement, we map a given loop configuration to a height profile via the following mapping. We begin on a reference vertex of the square lattice, which corresponds to the root node of a Bethe lattice with coordination number m (see Fig. 6.1 for an illustration). Then consider moving along an (arbitrary) real space path. Moving to a neighboring vertex on the square lattice implies traversing an edge of a particular color; on the Bethe lattice, this corresponds to hopping along an edge of the same color. Any sequence of colors encountered as we move along the real space path thus maps onto a particular sequence of moves on the Bethe lattice (e.g., if we encounter two red edges in succession in real space, then we hop along the red bond on the Bethe lattice and then back along that same red bond). Moreover, the local constraint (6.9) implies that the position on the Bethe lattice is independent of local deformations of the real space path.⁴ A height profile can then be obtained using the (Hamming) distance to the root note on the Bethe lattice. This process is illustrated along a one-dimensional cut in Fig. 6.1. At a local maximum of the height field (depth $d > 1$), the height field must, by definition, decrease across all edges. Hence, at each such point, there exists a closed loop of a single color surrounding the local maximum. This loop can be flipped to be the same color as the loop at depth $d - 1$. This process can be repeated to connect *any* closed, noncrossing loop configuration contained within a contractible contour to a region of uniform color, so that the entire region becomes active. This also tells us that any local dynamics compatible with the 1-form symmetries can be reproduced by QF dynamics.

Once an active region wraps the system, it is surrounded by two noncontractible loops. There is no requirement that they are of the same color. See Fig. 6.2 for examples. If their colors differ, the colors of these winding loops cannot be modified via the previously described procedure. Instead, it may be necessary to simultaneously flip at least $2L$ spins to change the color of a noncontractible loop while remaining in the constrained subspace. Any noncontractible loop can still be deformed through the active regions arbitrarily, subject to the constraint (6.9).

⁴This statement is only true in general for paths that differ by a closed, contractible path. If the height field is not single-valued upon winding around the system, this indicates the presence of nonlocal conserved quantities, as we will discuss.

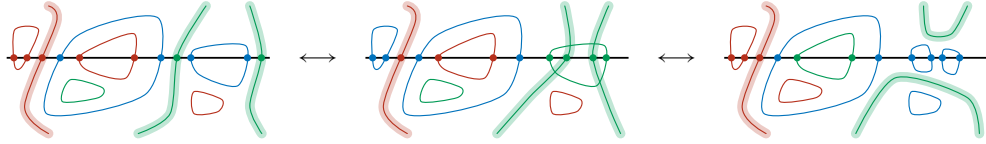


Figure 6.2: Schematic illustration of a valid configuration of noncrossing, contractible loops, and system-spanning loops (thick lines). Observe that a noncrossing dimer configuration is automatically created on the one-dimensional slice (black line) for contractible loops. Two adjacent noncontractible loops of the same color can be made contractible since loops of the same color are not forbidden from intersecting. In all configurations, only the red noncontractible loop contributes to the irreducible label.

Thus, QF dynamics naturally decomposes a 2D state into a collection of fluctuating closed loops that do not intersect, both contractible and noncontractible. The contractible loops can change color while the noncontractible loops cannot change color but can fluctuate past the contractible loops. Recall that in 1D the active pairs can change color while the unpaired spins cannot change color but can hop past the active pairs. This motivates a labeling procedure for QF dynamics similar to the procedure in 1D. First, choose a path that wraps the system once in the horizontal direction. Treat the pattern of spins along this path as a 1D system and use the procedure described in Sec. 6.2 to extract a label. This is the horizontal label, and there are $\mathcal{O}[(m - 1)^L]$ such labels, as in 1D. Fig. 6.2 illustrates this procedure (with the lattice not drawn). Furthermore, deforming the path only inserts or removes matching pairs into the spin pattern, which are removed when the pattern is converted into a label. This means that topologically equivalent paths will result in the same label. Now, choose a path that wraps the system once in the vertical direction and extract a vertical label. The vertical and horizontal labels must satisfy some compatibility, discussed in Sec. 6.3.4, but the fact that the number of Krylov sectors grows exponentially in L diagnoses fragmentation in the QF model.⁵

Finally, we can see that this fragmentation is *topologically robust*. The (exponentially numerous) irreducible labels for the Krylov sectors depend only on the sequence of *noncontractible* loops

⁵Reference [88] defines fragmentation in 2D as the existence of $\exp(L^2)$ Krylov sectors and classifies $\exp(L)$ Krylov sectors as a subsystem symmetry. The QF model does not possess a subsystem symmetry but still has $\exp(L)$ Krylov sectors in each symmetry sector. The presence of nonlocal conserved quantities in the QF model justifies our use of the term fragmentation.

(of nonrepeating color), and noncontractible loops can neither change color nor fluctuate past noncontractible loops of a different color, unless we act on $\mathcal{O}(L)$ degrees of freedom. Thus, any k -local dynamics, with $k/L \rightarrow 0$, cannot change the Krylov sector label.

6.3.2 Boundary conditions

Our discussion here will focus on open boundary conditions; discussion of periodic boundaries is relegated to Appendix C.2. It will be helpful to have two types of open boundaries: one type on which the symmetry operators may end and one on which they may not, similar in spirit to surface codes [12]. In addition to being more physically realizable, this will allow us to avoid the constraints between horizontal and vertical labels, so that the labeling system is more like the 1D version. The first boundary is the “smooth” boundary, with no edges sticking out. On this boundary we continue to define the symmetry to act on closed paths on the lattice that do not end. A source-free configuration of such a boundary may look like:


(6.12)

where all boundary faces are source free. Observe that loops are allowed to end on this boundary.

To obtain a system with nontrivial 1-form symmetry charges, we must find a boundary on which the symmetry operators can terminate. Ordinarily, this type of boundary, the “rough” boundary, has boundary edges sticking out of it. We find it more natural to define the rough boundary in the QF model to have every other boundary edge sticking out, so that all symmetry operators act on an even number of legs. Then, we define symmetry operators on paths \mathcal{C} that terminate on the boundary edges. Source-free configurations, with $\hat{N}_{\mathcal{C}}^{\alpha} = 0$, are

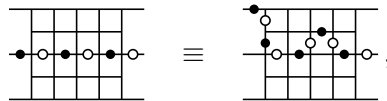

(6.13)

and configurations related to these by interchanging colors, as in (6.9). This preserves the graphical

constraint that loops of different colors may not intersect. An example configuration is



Note that loops cannot terminate on the rough boundary. Just as in the bulk, two symmetry operators that differ across a source-free region agree, so that the endpoints of a symmetry operator may be moved without changing its value:



where closed and open circles distinguish between the two sublattices. If, however, we tried to define symmetry operators that end on the smooth boundary there is no reason they should give the same symmetry charges, so symmetry operators that stretch from the left to the right boundary are noncontractible.

Having defined the operators that measure the symmetry charge in (6.8), we should also define the operators charged under the symmetry. These are operators that locally commute with the constraint but may fail to commute with the nontrivial symmetry operators. To write such operators we must first choose a closed path \mathcal{C}' on the dual lattice formed by placing vertices on the plaquette centers of the primary lattice. This path is required to turn at every vertex of the dual lattice. Then, the charged operators are

$$\hat{\mathcal{O}}_{\mathcal{C}'}^{\alpha\beta} = \prod_{i \in \mathcal{C}'} |\alpha\rangle\langle\beta|_i, \quad \alpha, \beta = 0, \dots, m-1, \quad \alpha \neq \beta, \quad (6.15)$$

which simultaneously projects onto dual paths where all edges are in the state $|\beta\rangle$ and then flips them all to $|\alpha\rangle$. These operators always commute with the constraint but act trivially if the edges in the chosen dual path are not all in the initial state $|\beta\rangle$. If \mathcal{C}' wraps the system in the vertical (horizontal) direction, it may change the value of $\hat{N}_{\mathcal{C}'}^{\alpha}$ if \mathcal{C} wraps the system in the horizontal (vertical)

direction.

In the bulk, the smallest possible charged operators correspond precisely to the quad flip (6.11).

As discussed in Sec. 6.3.1, any contractible charged operator can be decomposed into a series of quad flips. The charged operators are allowed to end on the smooth boundary, in the sense that this can be consistent with the symmetry. In particular, a charged operator that acts on the three edges around a vertex may flip those three edges if they match. For example, the three blue edges in (6.12) may be flipped to either green or red.

Near the rough boundary, vertices have either three or four edges sticking out from them. The four-edge vertices behave like bulk vertices and support QF moves. The three-vertex edges behave like those on the smooth boundary and support triple flips. For example, the three red edges in (6.14) may be flipped to either green or blue. Both of these scenarios correspond to closed loops that do not end on this boundary. In fact, no charged operators may end on the rough boundary.

A system with smooth boundaries on the top and bottom and rough boundaries on the left and right will have a nontrivial 1-form symmetry evaluated on horizontal system-spanning paths. The symmetry counts the number of nontrivial vertical system-spanning loops, whose endpoints can be shifted along the smooth top and bottom boundaries by the three-site flips at the smooth boundaries. Remember that loops cannot end on the rough (left and right) boundaries. Thus, our symmetry sectors for an $L \times L$ system are precisely those of the PF model on a length- L system, but with a 2D 1-form symmetry instead of a 1D 0-form symmetry.

6.3.3 Quad-flip model and robustness

We are now ready to write down a family of Hamiltonians that realize QF dynamics in a full tensor-product Hilbert space, where the hard constraint is made soft, i.e., it is enforced energetically. To this end, we introduce a natural “parent” Hamiltonian,

$$\hat{H} = J \sum_f \sum_{\alpha=0}^{m-1} \left(\hat{N}_{\partial f}^{\alpha} \right)^2 - g \sum_e \sum_{\alpha=0}^{m-1} \sum_{\beta=0}^{m-1} \xi_e^{\alpha\beta} |\alpha\rangle\langle\beta|_e , \quad (6.16)$$

where $J > 0$, $\hat{N}_{\partial f}^\alpha$ is defined in Eq. (6.8), the first sum is over the elementary faces f of the square lattice, and the second sum runs over all edges e . The dimensionless coefficients $\xi_e^{\alpha\beta}$ are of order one and serve to break all discrete symmetries. We will proceed by treating the second term perturbatively within the groundspace of the first.

The first term is positive semidefinite and is minimized by spin configurations satisfying $N_{\partial f}^\alpha = 0$ on all faces f (source-free configurations). As previously discussed, the source-free space has a $U(1)^{m-1}$ one form symmetry and grows as $W_m^{L^2}$. A Pauling estimate for W_m may be obtained as follows. The total Hilbert space has size m^{2L^2} , since spins live on edges of a square lattice. If we pick a reference plaquette and go around clockwise, we have m choices for the value of the first spin. The second spin can either match (one choice) in which case we have m choices for the remaining two spins (m^2 total), or it can be different ($m - 1$ choices), in which case the remaining two spins are fixed [so $m(m - 1)$ choices total]. Altogether this gives $2m^2 - m$ satisfying assignments out of m^4 , so a fraction $(2m - 1)/m^3$ of each plaquette Hilbert space satisfies the constraint. There are L^2 plaquettes in all, so (treating plaquettes as independent) a fraction $[(2m - 1)/m^3]^{L^2}$ of the total Hilbert space satisfies the constraints, yielding a constrained Hilbert space of size $[(2m - 1)/m^3]^{L^2} \times m^{2L^2} \sim [(2m - 1)/m]^{L^2}$. This yields an estimate $W_m \approx \frac{2m-1}{m}$. For $m = 2$, this estimate is within 3% of the exact value of $W_2 = (4/3)^{3/2} \simeq 1.54$, derived in Sec 6.4.1 from a mapping to square ice. On the other hand, for large m , this estimate undercounts the number of source-free states. Placing elementary length-four loops around every other vertex gives $W_m = \sqrt{m}$ in the large- m limit.⁶ The important point is that the subspace is exponential in system volume so there is room for a nonzero entropy density, and it makes sense to talk about thermalization or lack thereof.

The second term is the most general single-site Hamiltonian, and will generate generic longer-range terms within perturbation theory.⁷ Hermiticity requires that the matrix elements satisfy

⁶We thank Ethan Lake for this observation.

⁷Since the basic structure of our dynamics follows purely from 1-form symmetries (which are emergent within the groundspace of the first term), it follows that the basic results will be robust to inclusion of arbitrary k -body perturbations, without requirement of spatial locality, as long as $k/L \rightarrow 0$ in the thermodynamic limit.

$\xi_e^{\alpha\beta} = \bar{\xi}_e^{\beta\alpha}$. We can view the matrix elements as creation and annihilation operators for sources/sinks, breaking the 1-form symmetry and leading to nontrivial mixing of the classical ground states in the eigenstates of Eq. (6.16). However, we will now show that, even in the presence of the off-diagonal matrix elements, QF dynamics are preserved up to order system size in perturbation theory.

Let us consider the lowest-order dynamics produced by the off-diagonal matrix elements within the constrained space. This is given by the term

$$\hat{H}_{\text{QF}} = -\frac{g^4}{J^3} \sum_v \sum_{\alpha \neq \beta} \sum_{\beta=0}^{m-1} \xi_v^{\alpha\beta} \hat{A}_v^{\alpha\beta}, \quad \xi_v^{\alpha\beta} = \frac{5}{16} \prod_{e \in v} \xi_e^{\alpha\beta} \quad (6.17)$$

where $\hat{A}_v^{\alpha\beta} = \prod_{e \in v} |\alpha\rangle\langle\beta|_e$ flips the four spins around vertex v to state $|\alpha\rangle$ if they are all initially in state $|\beta\rangle$. We have omitted diagonal transitions, which lead to a trivial energy shift. Thus we recover QF dynamics, so we call (6.17) the QF Hamiltonian. The 5/16 prefactor comes from summing all 4! ways of flipping the spins around a vertex at fourth order in perturbation theory.

For vertices v_0 on the smooth boundary, the lowest-order terms come at third order in perturbation theory. They have the form

$$\hat{H}_{\text{QF}} = -\frac{g^3}{J^2} \sum_{v_0} \sum_{\alpha \neq \beta} \sum_{\beta=0}^{m-1} \xi_{v_0}^{\alpha\beta} \hat{A}_{v_0}^{\alpha\beta}, \quad \xi_{v_0}^{\alpha\beta} = \prod_{e \in v_0} \xi_e^{\alpha\beta} \quad (6.18)$$

and $\hat{A}_{v_0}^{\alpha\beta}$ now acts on only three spins. On the rough boundary, perturbation theory generates $\hat{A}_v^{\alpha\beta}$ terms on three-edge vertices at third order and on four-edge vertices at fourth order.

We should recognize the bulk and boundary terms as the minimal charged operators around every vertex. Thus, we have entirely recovered the dynamics we considered in Sec. 6.3.1. If we consider higher orders in perturbation theory, we will generate new terms, but they will be decomposable into series of quad flips, as shown in Sec. 6.3.1. The result is that the fragmentation remains exact at *any* order in perturbation theory, up to order system size. At $\mathcal{O}(L)$ in perturbation theory, however, we can flip the color of a noncontractible loop, changing the one-form symmetry charge and removing the Krylov structure associated with the irreducible labels.

Although perturbative dynamics will not melt the Krylov sectors, there may be nonperturbative effects that do. At times exponentially long in J/g the system is able to violate the source-free constraint and leave the groundspace of the classical Hamiltonian. Then, a noncontractible loop may break apart and retract. This exponentially long timescale is the prethermal timescale up to which the parent Hamiltonian realizes dynamics with an emergent one-form symmetry, and may be bounded using now standard techniques [2]. Imposing the source-free constraint exactly (instead of softly) amounts to setting the prethermal timescale for k -local dynamics to infinity, in the thermodynamic limit.

6.3.4 Fragmentation

We are now prepared to describe the fragmentation of the QF Hamiltonian in full detail. First, let us use the boundary conditions from Sec. 6.3.2, with smooth boundaries on the top and bottom and rough boundaries on the left and right. The groundspace has an emergent $U(1)^{m-1}$ one-form symmetry, defined on horizontal system-spanning paths. There are $\mathcal{O}(L)$ possible symmetry charges for each independent one-form symmetry, so overall there are $\mathcal{O}(L^{m-1})$ symmetry sectors taking the emergent one-form symmetry into account. The dynamics must, at minimum, be block diagonal by one-form symmetry sector. However, as we shall now show, each symmetry sector will further be fragmented into $\exp(L)$ dynamically disconnected subblocks.

The basic argument follows the discussion in Sec. 6.2 for the one-dimensional pair-flip model. Namely, we can take any horizontal system-spanning path on the lattice and consider the sequence of colors encountered along this effective one-dimensional system. We can then sequentially delete same-color neighbors until we are left with an irreducible one-dimensional sequence or ‘label’ of length $0 \leq \ell \leq L$ in which no two adjacent entries are the same color. It is straightforward to see that local deformations of the real-space path within the source-free subspace do not alter this irreducible label. For example, any system-spanning path terminating on the left and right boundaries of Fig. 6.3a returns the length $\ell = 2$ label $|\textcolor{teal}{\bullet} \textcolor{red}{\bullet}\rangle$. This irreducible label essentially enumerates the sequence of distinct vertical system-spanning loops of nonrepeating color. We

do not count adjacent loops of the same (i.e., repeating) color since these can locally reconnect and flip. In contrast to the one-dimensional PF model, in the two-dimensional QF model this irreducible label exhibits topological stability – the only way to change the irreducible label is to flip an entire system-spanning vertical loop, which requires acting on $\mathcal{O}(L)$ degrees of freedom. Thus, this irreducible label is conserved under any k -local dynamics (with $k/L \rightarrow 0$), and thus defines a topologically robust Krylov subsector.

The total number of symmetry sectors is $\mathcal{O}(L^{m-1})$, but, as discussed in Sec. 6.2, the total number of Krylov subsectors (now topologically robust) is $\mathcal{O}[(m-1)^L]$. This follows because labels can have length up to L [see Fig. 6.3b for an example of a state with a label of length $\ell = L$], and once the first entry in the label is fixed each subsequent entry has $(m-1)$ choices. Thus, there are only polynomially many distinct symmetry sectors, but there are exponentially many dynamically distinct Krylov subsectors. It follows that the dynamics must exhibit fragmentation, and cannot be fully ergodic. It further follows that for $m \geq 3$ fragmentation arises in *every* symmetry sector. This follows by analogy to Sec. 6.2 because for any given value of the symmetry charge, there is a minimal system size L_{\min} required to realize it. There exist ‘charge-neutral’ motifs with irreducible labels that can be ‘glued’ on, e.g., for $m = 3$ we can consider a sequence of vertical system-spanning loops of the form $| \bullet \bullet \bullet | \bullet \bullet \bullet \rangle$, or five other patterns obtained from this one by permuting colors. Of the six motifs, four have a first spin that does not match the last spin of our chosen pattern. Gluing such a motif onto the system of size L_{\min} does not change the symmetry charge but does multiply the number of Krylov subsectors by four. Such a process can then be iterated (bearing in mind that for $m = 3$ only four of the ‘charge-neutral, gluable motifs’ will have the property that the first loop of the motif does not have the same color as the last loop of the previous motif), giving a number of Krylov sectors that scales as at least $\sim 4^{(L-L_{\min})/6}$, for $m \geq 3$. Thus, the QF Hamiltonian (with $m \geq 3$) exhibits fragmentation in generic symmetry sectors, with the fragmentation furthermore exhibiting topological stability, being robust to arbitrary k -local perturbations as long as $k/L \rightarrow 0$ in the thermodynamic limit.

A special role is played by densely packed configurations, which generate labels of length L .

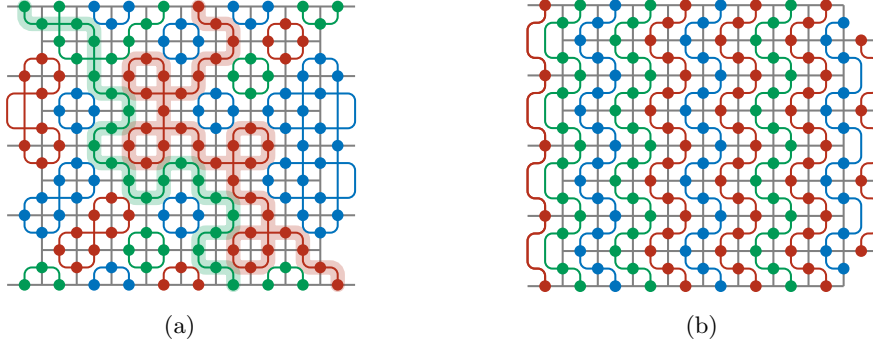


Figure 6.3: (a) A state belonging to the Krylov sector specified by the label $|\text{green dot red dot}\rangle$, which captures the presence of the green and red system-spanning loops (thick green and red lines, respectively). (b) A close-packed configuration of system-spanning loops that remains frozen under local dynamics. Note that the offset of the rough boundary differs on the left and right edges to accommodate a dense packing of loops.

As long as we stagger the rough boundary edges, as in Fig. 6.3, these configurations correspond to dense packings of noncontractible loops of nonrepeating color, and generate frozen states that have no dynamics under arbitrary k -local perturbations. For an example of a frozen state, see Fig. 6.3b. The number of such configurations depends strongly on both the local Hilbert space dimension m and on whether (and, if so, how) the lattice is terminated. With periodic boundary conditions, the pattern in Fig. 6.3b appearing in the top row can be shifted either left or right in each subsequent row, subject to the constraint that the pattern joins up around the periodic boundaries. With open boundary conditions, this freedom is not present, since the packing would cease to be dense at the left and right boundaries. For $m = 2$ there are an $\mathcal{O}(L^0)$ number of frozen configurations with open boundaries, although there are an $\exp(L)$ number of frozen configurations with periodic boundaries [126]. For $m \geq 3$, the number of frozen configurations grows exponentially with L even for open boundaries; there are m choices for color of the boundary loop, and $m - 1$ choices for each of the other loops. Hence, the number of frozen configurations is $\propto (m - 1)^L$. Exact (asymptotic) countings of the number of Krylov sectors and the number of frozen states are derived in Appendix C.2, for both open and periodic boundary conditions. With open boundaries we have $\mathcal{O}[(m - 1)^L]$ frozen states and $\mathcal{O}[(m - 1)^L]$ nonfrozen Krylov sectors for $m \geq 3$. With periodic

boundaries we have $\mathcal{O}[(m-1)^L]$ frozen states but only $\mathcal{O}[(m-1)^L/L]$ nonfrozen Krylov sectors for $m \geq 3$.

We can also define the commutant algebra [88] for the QF model. The operators in the algebra generalize the symmetry operators (6.8) and are entirely analogous to those in the PF model, which were found in Ref. [88]. With our choice of open boundary conditions, choose a horizontal system-spanning path $\mathcal{C} = \{e_0, e_1, \dots, e_K\}$ on the lattice, where $K \geq L$ is the length of the path. The nonlocal integrals of motion (IoMs) are

$$\widehat{N}^{\alpha_1 \alpha_2} = \sum_{j_1 < j_2} (-1)^{j_1 + j_2} \widehat{\mathcal{P}}_{j_1}^{\alpha_1} \widehat{\mathcal{P}}_{j_2}^{\alpha_2}, \quad \alpha_1 \neq \alpha_2, \quad 0 \leq \alpha_1, \alpha_2 \leq m-1$$

and the larger operators

$$\widehat{N}^{\alpha_1 \alpha_2 \dots \alpha_k} = \sum_{j_1 < j_2 < \dots < j_k} (-1)^{\sum_l j_l} \widehat{\mathcal{P}}_{j_1}^{\alpha_1} \widehat{\mathcal{P}}_{j_2}^{\alpha_2} \dots \widehat{\mathcal{P}}_{j_k}^{\alpha_k}, \quad (6.19)$$

with⁸ $0 \leq k \leq L$ and $\alpha_j \neq \alpha_{j+1}$. Within the source-free subspace the value of these operators does not depend on smooth variations of the choice of \mathcal{C} . As described in Ref. [88], in a system with L even (odd), the IoMs with k even (odd) are all linearly independent but the IoMs with k odd (even) can be written in terms of the former. Just as we can view the symmetry operators as distinguishing symmetry sectors which consist of collections of Krylov sectors, we can view the IoMs as distinguishing successively more fine-grained sectors.

6.4 Generalized no-crossing models

Having introduced the symmetries that give rise to QF dynamics and its numerous conserved patterns, we move to discussing related models that exhibit analogous phenomena. These include models to which the QF Hamiltonian reduces in certain limits, as well as various dualities of the model, and its extension to higher dimensions. This section is not ‘load bearing’ for our basic story,

⁸We could define similar operators for $k \leq K$, but these longer operators would contain redundant information.

and may be safely skipped by readers uninterested in connections to known models or dualities thereof.

To facilitate the presentation of the various dualities we discuss, it will be useful to define the following clock operators on each edge e , which act on the m -dimensional Hilbert space introduced in Eq. (6.1)

$$\hat{\mathcal{Z}} |\alpha\rangle = e^{2\pi i \alpha/m} |\alpha\rangle , \quad \hat{\mathcal{X}} |\alpha\rangle = |\alpha + 1\rangle , \quad (6.20)$$

so that $\hat{\mathcal{X}}$ and $\hat{\mathcal{Z}}$ are unitary and obey $\hat{\mathcal{Z}}\hat{\mathcal{X}} = e^{2\pi i/m} \hat{\mathcal{X}}\hat{\mathcal{Z}}$, which generalizes the anticommutation of Pauli matrices ($m = 2$). Since we identify $|\alpha + m\rangle \equiv |\alpha\rangle$, we also have $\hat{\mathcal{Z}}^m = \hat{\mathcal{X}}^m = \mathbb{1}$.

6.4.1 Square ice

For spin-1/2 degrees of freedom (i.e., $m = 2$), the parent Hamiltonian for the QF model that we present in Eq. (6.16) is unitarily equivalent to square ice [78, 86, 120] in a magnetic field, allowing us to make exact statements about the number of constraint-satisfying states. To see this, consider the unitary transformation that flips the sign of $\hat{\mathcal{Z}}$ operators on vertically oriented edges:

$$\hat{U} = \prod_{e: \text{vertical}} \hat{\mathcal{X}}_e . \quad (6.21)$$

Under this transformation, the constraint on faces that selects local ground state configurations becomes

$$\hat{N}_{\partial f}^\uparrow = \sum_{e_j \in \partial f} (-1)^j \hat{\mathcal{P}}_{e_j}^\uparrow \xrightarrow{\hat{U}} \sum_{e_j \in \partial f} \hat{\mathcal{Z}}_{e_j} = 0 , \quad (6.22)$$

with the same expression for $\hat{N}_{\partial f}^\downarrow$, up to a sign. Hence, the constraint in this rotated basis corresponds to requiring that there exist two up spins and two down spins around every face of the square lattice, which (up to a sublattice-dependent sign) is equivalent to the two-in-two-out “ice rule” [8, 34]. For consistency with established conventions for square ice, we will interchange the vertices

and faces of the square lattice, such that the constraints are on vertices. On one sublattice the six constraint-satisfying spin configurations take the form

$$\left| \begin{array}{c} \textcolor{red}{\bullet} \\ \square \\ \textcolor{red}{\bullet} \end{array} \right\rangle \mapsto \left| \begin{array}{c} \textcolor{black}{\circ} \\ \textcolor{black}{\circ} \\ \textcolor{black}{\bullet} \end{array} \right\rangle \equiv \left| \begin{array}{c} \rightarrow \\ \uparrow \\ \leftarrow \\ \downarrow \end{array} \right\rangle, \quad \left| \begin{array}{c} \textcolor{red}{\bullet} \\ \square \\ \textcolor{blue}{\bullet} \end{array} \right\rangle \mapsto \left| \begin{array}{c} \textcolor{black}{\circ} \\ \textcolor{black}{\circ} \\ \textcolor{black}{\bullet} \end{array} \right\rangle \equiv \left| \begin{array}{c} \rightarrow \\ \uparrow \\ \leftarrow \end{array} \right\rangle, \quad (6.23)$$

with the sign convention for the arrows reversed for vertices belonging to the other sublattice. The correspondence in (6.23) means that we can deduce the size of the constrained Hilbert space for the $m = 2$ QF model, since the number of two-in-two-out configurations is known to scale as $W_2^{L^2}$ with $W_2 = (4/3)^{3/2}$ [78, 79].

The QF dynamics described in Sec. 6.3 – in which closed loops of a single color passing through four spins are simultaneously flipped to a different color – can now viewed as “ring-exchange” dynamics. In particular, in the rotated basis, spins around a face can be flipped between clockwise and anticlockwise orientations:

$$\left| \begin{array}{c} \rightarrow \\ \leftarrow \end{array} \right\rangle \leftrightarrow \left| \begin{array}{c} \leftarrow \\ \rightarrow \end{array} \right\rangle. \quad (6.24)$$

Since the states in Eq. (6.23) are in one-to-one correspondence with one another, ring-exchange dynamics acting within the manifold of two-in-two-out states will exhibit conservation laws identical to those in the $m = 2$ QF model. However, in the QF model with just two colors, fragmentation is confined to symmetry sectors of maximal one-form charge [126]; in all other sectors each symmetry sectors hosts just a single label. This is in stark contrast to the $m > 2$ generalizations discussed in Sec. 6.3, which exhibit fragmentation in *generic* symmetry sectors.

6.4.2 Dualities and generalized PXP models

6.4.2.1 From pair-flip to constrained spin flips

We now show how the pair-flip model in one dimension is dual to a parity-sensitive PXP-type model. We will work with $m = 3$ for simplicity, with the generalization to $m > 3$ straightforward.

Let us define a Kramers-Wannier duality transformation for clock variables⁹ $\widehat{Z}_v \widehat{Z}_{v+1} = \widehat{\mathcal{Z}}_e$, which relates the degrees of freedom on the edge e and the two adjacent vertices v and $v + 1$. As in the edge picture, we define the following states on vertices: $|0\rangle \equiv |\blacksquare\rangle$, $|1\rangle \equiv |\square\rangle$, $|2\rangle \equiv |\blacksquare\square\rangle$. With open boundary conditions we must add an extra spin in the vertex picture that can be chosen arbitrarily (making the mapping one-to-three). Setting the boundary spin to $|\blacksquare\rangle$, the duality acts as

$$|\bullet \bullet \bullet \bullet \bullet \bullet \bullet \bullet \bullet \rangle \mapsto |\square \square \square \square \square \square \square \square \square \rangle . \quad (6.25)$$

The flippable pairs in the edge picture have been replaced by motifs of the form $|\square \square \square \rangle$ or $|\square \square \square \square\rangle$, i.e., a central spin surrounded by two spins of equal value. If the pair from which this motif is derived is permuted, $00 \rightarrow 11 \rightarrow 22 \rightarrow 00$, then, in the dual picture, this has the effect of permuting the central spin only, $0 \rightarrow 1 \rightarrow 2 \rightarrow 0$, leaving its neighbors unchanged. Hence, in the dual language, the generic pair-flip model from Sec. 6.2 may be written

$$\widehat{H}_{\text{PF}} = g \sum_{v=1}^{L-1} \sum_{\alpha, \beta, \gamma=0}^{m-1} \xi_v^{\alpha+\gamma, \beta+\gamma} \widehat{P}_{v-1}^\gamma \widehat{X}_v^{\alpha-\beta} \widehat{P}_v^\beta \widehat{P}_{v+1}^\gamma + \text{h.c.} \quad (6.26)$$

Note that the central projector does not affect the possible transitions; it merely ensures that the appropriate matrix element $\xi_v^{\alpha\beta}$ is selected. In the above equations $\widehat{X} |\alpha\rangle = |\alpha + 1\rangle$ permutes the dual m -level systems, while $\widehat{P}_v^\alpha = |\alpha\rangle\langle\alpha|_v$ projects onto color α on vertex v .

As stated above, in the dual language (6.26), spins are only dynamical if their neighbors are equal to one another. This model strongly resembles the PXP model [76, 80, 84, 129, 130], for spin-1/2 degrees of freedom, where spins may only flip if both neighbors are in the ‘0’ (ground) state due to the Rydberg blockade constraint. Equation (6.26), on the other hand, also permits the central spin to flip if both neighbors are in the ‘1’ (excited) state. The dual model (6.26) therefore generalizes the Rydberg constraint to a *parity*-sensitive constraint in which only the parity of neighboring 1’s determines whether a given spin can flip.

⁹This transformation differs slightly from the “standard” Kramers-Wannier transformation for clock variables, which takes the form $\widehat{\mathcal{X}}_e = \widehat{Z}_v^\dagger \widehat{Z}_{v+1}$.

The model in the vertex language appears to have an extra discrete symmetry

$$\prod_v \hat{X}_v^{(-1)^v} = \hat{X}_0 \hat{X}_1^\dagger \hat{X}_2^\dagger \hat{X}_3^\dagger \dots ,$$

due to the choice of initial spin state. This symmetry can be retained in the edge picture by keeping track of an extra degree of freedom in the edge picture as a noninteracting spin on which the symmetry acts. Then, both pictures enjoy a \mathbb{Z}_m symmetry, although it is local in the edge picture and global in the vertex picture. This is a generic feature of nonlocal dualities [26].

In the parity-sensitive PXP picture, we can also create Krylov sector labels via (i) working from left to right, identify motifs of the form $|\blacksquare \blacksquare \blacksquare \blacksquare\rangle$ (including three identically colored sites), (ii) for each motif identified, replace the pattern by the majority color, e.g., $|\blacksquare \blacksquare \blacksquare \blacksquare\rangle \mapsto |\blacksquare\rangle$, (iii) repeat the previous two steps until there are no such motifs remaining. This prescription leads to a dual conserved pattern. As an example, all of the following configurations [which are connected by local dynamics generated by the dual Hamiltonian (6.26)] map to the same conserved pattern:

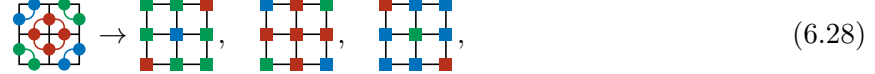
$$[|\blacksquare \blacksquare \blacksquare \blacksquare\rangle \leftrightarrow |\blacksquare \blacksquare \blacksquare \blacksquare\rangle \leftrightarrow |\blacksquare \blacksquare \blacksquare \blacksquare\rangle] \mapsto |\blacksquare \blacksquare\rangle . \quad (6.27)$$

In general it is not necessary to start with the left-most motif; all choices lead to the same label. Note that the patterns on the left-hand side are dual to the patterns in (6.5) and the label on the right-hand side is dual to the label $|\bullet\rangle$ that would be found from removing paired spins from (6.5).

6.4.2.2 Two-dimensional generalization

As for the one-dimensional model, we may introduce dual variables living on vertices via a similar Kramers-Wannier duality. These variables satisfy $\hat{Z}_v \hat{Z}_{v'} = \hat{\mathcal{Z}}_e$ for the two neighboring vertices $\langle vv'\rangle$ at either end of the edge e . Note that, for i, j, k, l labeling the edges clockwise around a face f , we must have $\hat{\mathcal{Z}}_i \hat{\mathcal{Z}}_j^\dagger \hat{\mathcal{Z}}_k \hat{\mathcal{Z}}_l^\dagger = \mathbb{1}$ for \hat{Z}_v to be independent of the path used to define it. This constraint is automatically satisfied within the source-free subspace.

We can therefore find (via a one-to- m map) the spin configuration on vertices that corresponds to a given “domain wall” configuration on edges. For example,



where we have shown the three possible states on the right-hand side, and spins on vertices have been represented using colored squares. The allowed configurations (6.9) become



where $a + b = \alpha \pmod{m}$ and $a + c = \beta \pmod{m}$. More generally, if i, j, k, l label spins on vertices clockwise around the face f , then the operator $\hat{N}_{\partial f}^{\alpha}$ that measures violations of the constraint, written in terms of the operators on vertices, is

$$\hat{N}_{\partial f}^{\alpha} = \frac{1}{m} \sum_{\beta=0}^{m-1} e^{-2\pi i \alpha \beta / m} (\hat{Z}_i^{\beta} - \hat{Z}_k^{\beta})(\hat{Z}_j^{\beta} - \hat{Z}_l^{\beta}), \quad (6.30)$$

and the ground space is still given by the requirement that $\hat{N}_{\partial f}^{\alpha} = 0$ for every face and color α . From (6.29) or (6.30) it is clear that, in the vertex language, every face must have at least one identically colored diagonal pair in the source-free subspace. This suggests a further dual description of the system in terms of domain wall variables between such diagonal pairs [126]. More precisely, we introduce two degrees of freedom for every elementary face of the form $\hat{Z}_i^{\dagger} \hat{Z}_k$ and $\hat{Z}_j^{\dagger} \hat{Z}_l$, which correspond to domain wall variables between spins belonging to the same sublattice (i.e., even or odd). In this picture, the constraint implies that domain walls (defined by $\bar{Z}_{v_1} Z_{v_2} \neq 1$) between the even and odd sublattices cannot intersect, as illustrated in Fig. 6.4c. A discussion of this final dual description is presented in Appendix C.1.

In the vertex language, the “parent” Hamiltonian is

$$\hat{H} = \tilde{J} \sum_f \sum_{\alpha} (N_{\partial f}^{\alpha})^2 - g \sum_v \sum_{\alpha=0}^{m-1} \sum_{\beta=0}^{m-1} \tilde{\xi}_v^{\alpha\beta} |\alpha\rangle\langle\beta|_e , \quad (6.31)$$

where $\tilde{J} > 0$, and the second term is the most general single-site term, which is assumed to be weaker than the first term. We can play the same game of projecting the dynamics into the constrained subspace, the groundspace of the first term. In this basis we only need to go to first order in perturbation theory, finding

$$\hat{H}_{\text{QF}} = -g \sum_v \sum_{\alpha=0}^{m-1} \sum_{\beta=0}^{m-1} \tilde{\xi}_v^{\alpha\beta} |\alpha\rangle\langle\beta|_e \hat{\Pi}_v^{\gamma}, \quad (6.32)$$

where $\hat{\Pi}_v^{\gamma} = \prod_{v':\langle vv'\rangle} \hat{P}_{v'}^{\gamma}$ projects all vertices v' that neighbor v into the state γ . We can compare to Eq. (6.17) to see that $\tilde{\xi}_v^{\alpha\beta} \sim \xi_v^{\alpha+\gamma, \beta+\gamma}$. The QF Hamiltonian (6.17) is therefore dual to a Hamiltonian in which a spin is only dynamical if all four spins on its neighboring vertices are equal to one another. This correspondence is illustrated in Fig. 6.4, where flippable closed loops of length four in (a) map to vertices whose neighbors are all equal in (b). The model (6.32) is equivalent (for $m = 2$) to the first-order term that arises when projecting a transverse field into the ground space of the “CZ _{p} ” Ising model introduced in Ref. [126]. As in 1D, one can view Eq. (6.32) for $m = 2$ as arising from a parity-sensitive Rydberg blockade constraint. Namely, as shown in Ref. [126], Eq. (6.32) arises at first order in a model where an odd number of neighboring 1’s are forbidden around every face.

In fact, the $m = 2$ case of the 2D parity-sensitive PXP model with periodic boundary conditions is precisely the CZ _{p} model of Ref. [126]. The CZ _{p} model exhibits topologically robust ergodicity breaking, but only in maximal one-form charge sectors and with those sectors being fully frozen. Maximal charge sectors shatter into $\mathcal{O}(2^L)$ frozen states, while nonmaximal sectors are fully ergodic. Meanwhile, with open boundary conditions, the maximal charge sectors of the CZ _{p} model have only a single state and there is no ergodicity breaking to be had. In contrast, with $m > 2$ the parity-sensitive PXP model (like the QF model) exhibits ergodicity breaking with both periodic

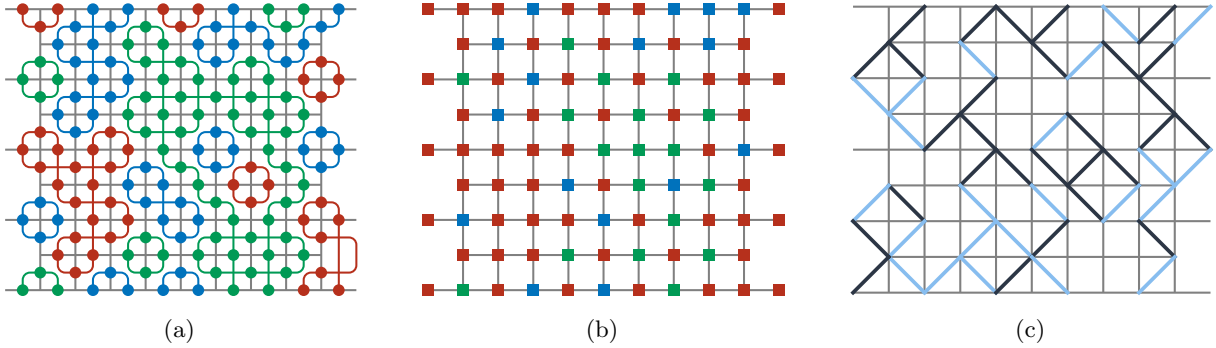


Figure 6.4: Three dual descriptions of the same state obeying the source-free constraint in models exhibiting topologically robust fragmentation. (a) The QF model (6.17), with degrees of freedom on edges. The four spins around a vertex are able to flip only if they match. (b) The parity-sensitive PXP model (6.32), with degrees of freedom on vertices. A given spin is able to flip only if its four neighbors are equal to one another. (c) The dual description introduced in Appendix C.1, where a domain wall is drawn if two adjacent spins belonging to the same sublattice do not match.

and open boundary conditions, there is fragmentation in generic symmetry sectors (not just sectors of maximal charge), and the fragmentation is not ‘all or nothing,’ i.e., there exist Krylov subsectors with a distribution of sizes between one (frozen states) and exponentially large in system size. the size of the full symmetry sector. As with the CZ_p model, this basic phenomenology is topologically robust.

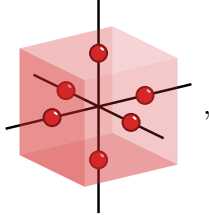
6.4.3 Three-dimensional models

The natural generalization of the PF and QF models to 3D is a model on a cubic lattice with a 2-form symmetry. To define the model, let us put m -level degrees of freedom (6.1) on the edges of a cubic lattice. The symmetry operators take the same form as in Eq. (6.8), now defined on one-dimensional paths embedded in three-dimensional space. The 2-form symmetry once again breaks the constrained Hilbert space into $\mathcal{O}(L^{m-1})$ symmetry sectors.

Requiring $\hat{N}_{\partial f}^\alpha = 0$ on all faces f allows the same configurations as shown in Eq. (6.9), now on faces in any orientation. Graphically, these constraints require that the 3D state decomposes into a collection of closed membranes that do not intersect, both contractible and noncontractible.

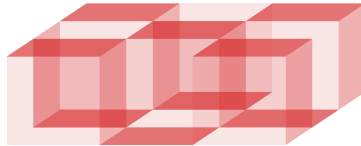
The allowed dynamics involve flipping all the spins around a vertex, of which there are now

six. We will call the whole family of models the vertex-flip (VF) models. When viewed on a 2D slice of the system, the allowed moves look the same as those in (6.11). The VF move changes the color of the smallest contractible membrane:



where the red spheres live on the edges of the primary cubic lattice and the shaded faces connect vertices of the dual cubic lattice. As in 2D, any contractible membrane may be flipped by a series of VF moves. Flipping a noncontractible membrane without violating the constraint now requires simultaneously flipping $\mathcal{O}(L^2)$ spins.

Operators charged under the 2-form symmetry are membranes on the dual lattice. As in 2D, they have nontrivial microscopic geometric requirements. They are required to turn at every edge of the dual lattice. For example, the operator



is a section of a valid charged operator, drawn on the dual lattice. For clarity of illustration, we have omitted the spins and the edges of the underlying lattice.

We can once again define rough and smooth boundary conditions. The smooth boundary conditions are simple: just truncate the lattice so that no edges stick out. Charged operators may end on this boundary but symmetry operators may not. The rough boundaries must again be defined on a staggered lattice truncation. In a cubic lattice, the edges sticking out from a ordinary rough boundary form a square lattice. Now, remove the outward-pointing edges from one sublattice. This leaves behind doubled boundary faces, on which we permit configurations as in (6.13). Finally,

we put the rough boundary conditions on two opposite boundaries and smooth boundary conditions on the other four boundaries. With this choice of boundary conditions, the counting of sectors works the same way as in the PF and QF models. There are $\mathcal{O}(L^{m-1})$ symmetry sectors and $\mathcal{O}[(m-1)^L]$ Krylov sectors, some frozen and some nonfrozen.

Sectors are labeled by a pattern of system-spanning membranes of nonrepeating color. One key difference to the two-dimensional case is that, if all source-free states have equal energy, there is a macroscopic energy barrier between states from any two different Krylov sectors. If, instead, source-free states are separated by an extensive energy $\propto g$, there can exist energetic competition between the constraint violations (scaling as $J|\partial R|$) and this extensive energy (scaling as $g|R|$), leading to an energy barrier $\sim J^2/g$ that diverges as $g \rightarrow 0$. This timescale is analogous to magnetization reversal in a 2D Ising model at finite temperature in the presence of a longitudinal field. This energy barrier could make the fragmentation in the 3D VF model even more robust than the fragmentation in the QF model. This possibility remains to be fully explored.

6.5 Conclusions

We have constructed a family of quantum loop based models exhibiting ergodicity breaking with topological robustness. These models simultaneously generalize the CZ_p model of Ref. [126] to local Hilbert space dimensions $m > 2$ (in a dual representation), and the pair-flip model [18, 88] to higher dimensions, with the extra dimension(s) endowing the system with a topological stability that the pair-flip model lacks. The ergodicity breaking derives from $(d-1)$ -form symmetries in $d > 1$ spatial dimensions, which can emerge (in a prethermal sense) from simple parent Hamiltonians that softly (i.e., energetically) implement a ‘source-free’ constraint. The simplest $m = 2$ version of this physics—the CZ_p model—exhibits exponential fragmentation of Hilbert space, but only with periodic boundary conditions, and only in sectors of extremal symmetry charge. Moreover, the fragmentation is ‘all or nothing,’ i.e., either a given symmetry sector is fully frozen, or it is not fragmented at all. Once we generalize to $m > 2$, fragmentation is no longer limited to sectors of extremal charge, survives (suitable) open boundary conditions, and is not ‘all or nothing.’ That is,

there arise Krylov subsectors of size intermediate between one (frozen states) and exponentially large in system size. All of this phenomenology is topologically stable, i.e., it is robust to arbitrary k -local perturbations, as long as $k/L \rightarrow 0$ as we take system size $L \rightarrow \infty$. The results are exact if the constraint is imposed exactly (exact one-form symmetry), and valid up to an exponentially long prethermal timescale if the constraint is imposed energetically (emergent one-form symmetry).

This work opens up a new direction for exploration of ergodicity-breaking quantum dynamics. The models we have constructed provide proof of principle that qualitatively new phenomena in many-body quantum dynamics can arise protected by higher-form symmetries (which can emerge from simple local Hamiltonians). The exploration of emergent higher-form symmetries and their consequences, however, has only just begun. Particularly fruitful in this regard is the extension of such constructions to three spatial dimensions – we have sketched some considerations in Sec. 6.4.3, but a detailed exploration remains to be performed. We look forward to further exploration of these ideas.

It is also interesting to note that our results are exact when the higher-form symmetries are exact, and it has been shown that emergent higher-form symmetries can in fact be exact in the low-energy subspace [83, 96]. Might results analogous to ours therefore continue to hold even beyond the exponentially long ‘prethermal’ timescale that we estimate? This too presents a fruitful topic for future investigation.

Finally, while our discussion has focused on the quantum *dynamics*, the equilibrium properties of generalized loop model could also be of interest. During the preparation of this manuscript, we became aware of parallel work by Shankar Balasubramanian, Ethan Lake, and Soonwon Choi [4] on the ground state properties of no-crossing models, and this too presents an interesting direction for future work.

Chapter 7

Conclusions

In the end, we conclude with all the interesting quantum dynamics we have found from exotic symmetries.

References

- [1] D. Aasen, D. Bulmash, A. Prem, K. Slagle, and D. J. Williamson, “Topological defect networks for fractons of all types”, *Phys. Rev. Research* **2**, 043165 (2020).
- [2] D. Abanin, W. De Roeck, W. W. Ho, and F. Huveneers, “A rigorous theory of many-body prethermalization for periodically driven and closed quantum systems”, *Communications in Mathematical Physics* **354**, 809 (2017).
- [3] D. A. Abanin, E. Altman, I. Bloch, and M. Serbyn, “Colloquium: many-body localization, thermalization, and entanglement”, *Reviews of Modern Physics* **91**, 021001 (2019).
- [4] S. Balasubramanian, E. Lake, and S. Choi, *2D Hamiltonians with exotic bipartite and topological entanglement*, 2023.
- [5] M. Barkeshli, P. Bonderson, M. Cheng, and Z. Wang, “Symmetry fractionalization, defects, and gauging of topological phases”, *Phys. Rev. B* **100**, 115147 (2019).
- [6] R. J. Baxter, *Exactly solved models in statistical mechanics* (Elsevier, 2016).
- [7] D. Becker, T. Tanamoto, A. Hutter, F. L. Pedrocchi, and D. Loss, “Dynamic generation of topologically protected self-correcting quantum memory”, *Physical Review A* **87**, 10.1103/physreva.87.042340 (2013).
- [8] J. D. Bernal and R. H. Fowler, “A theory of water and ionic solution, with particular reference to hydrogen and hydroxyl ions”, *The Journal of Chemical Physics* **1**, 515 (1933).
- [9] H. Bombín, R. W. Chhajlany, M. Horodecki, and M. A. Martin-Delgado, “Self-correcting quantum computers”, *New Journal of Physics* **15**, 055023 (2013).
- [10] H. Bombín, “Gauge color codes: optimal transversal gates and gauge fixing in topological stabilizer codes”, *New Journal of Physics* **17**, 083002 (2015).
- [11] H. Bombín, “Single-shot fault-tolerant quantum error correction”, *Phys. Rev. X* **5**, 031043 (2015).
- [12] S. B. Bravyi and A. Y. Kitaev, *Quantum codes on a lattice with boundary*, 1998.
- [13] S. Bravyi, G. Duclos-Cianci, D. Poulin, and M. Suchara, “Subsystem surface codes with three-qubit check operators”, *QIC* **13**, 963 (2013).
- [14] J. C. Bridgeman, A. Kubica, and M. Vasmer, *Lifting topological codes: Three-dimensional subsystem codes from two-dimensional anyon models*, 2023.
- [15] B. J. Brown, D. Loss, J. K. Pachos, C. N. Self, and J. R. Wootton, “Quantum memories at finite temperature”, *Rev. Mod. Phys.* **88**, 045005 (2016).
- [16] D. Bulmash, O. Hart, and R. Nandkishore, *Multipole groups and fracton phenomena on arbitrary crystalline lattices*, 2023.

- [17] F. J. Burnell, X. Chen, L. Fidkowski, and A. Vishwanath, “Exactly soluble model of a three-dimensional symmetry-protected topological phase of bosons with surface topological order”, *Physical Review B* **90**, 10.1103/physrevb.90.245122 (2014).
- [18] L. Caha and D. Nagaj, *The pair-flip model: a very entangled translationally invariant spin chain*, 2018.
- [19] C. Castelnovo and C. Chamon, “Topological order in a three-dimensional toric code at finite temperature”, *Phys. Rev. B* **78**, 155120 (2008).
- [20] A. Chandran, T. Iadecola, V. Khemani, and R. Moessner, “Quantum many-body scars: a quasiparticle perspective”, *Annual Review of Condensed Matter Physics* **14**, 443 (2023).
- [21] S. Chesi, B. Röthlisberger, and D. Loss, “Self-correcting quantum memory in a thermal environment”, *Physical Review A* **82**, 10.1103/physreva.82.022305 (2010).
- [22] C. Cordova, T. T. Dumitrescu, K. Intriligator, and S.-H. Shao, *Snowmass white paper: generalized symmetries in quantum field theory and beyond*, 2022.
- [23] M. Creutz, L. Jacobs, and C. Rebbi, “Experiments with a gauge-invariant Ising system”, *Phys. Rev. Lett.* **42**, 1390 (1979).
- [24] M. Crossley, P. Glorioso, and H. Liu, “Effective field theory of dissipative fluids”, *J. High Energ. Phys.* **2017**, 95 (2017).
- [25] E. Dennis, A. Kitaev, A. Landahl, and J. Preskill, “Topological quantum memory”, *Journal of Mathematical Physics* **43**, 4452 (2002).
- [26] O. DeWolfe and K. Higginbotham, “Entanglement entropy and non-local duality: Quantum channels and quantum algebras”, *Annals of Physics* **448**, 169196 (2023).
- [27] T. D. Ellison, Y.-A. Chen, A. Dua, W. Shirley, N. Tantivasadakarn, and D. J. Williamson, *Pauli topological subsystem codes from Abelian anyon theories*, 2022.
- [28] J. Feldmeier, P. Sala, G. De Tomasi, F. Pollmann, and M. Knap, “Anomalous diffusion in dipole- and higher-moment-conserving systems”, *Phys. Rev. Lett.* **125**, 245303 (2020).
- [29] M. E. Fisher and J. Stephenson, “Statistical mechanics of dimers on a plane lattice. II. Dimer correlations and monomers”, *Phys. Rev.* **132**, 1411 (1963).
- [30] P. Flajolet and A. Odlyzko, “Singularity analysis of generating functions”, *SIAM Journal on Discrete Mathematics* **3**, 216 (1990).
- [31] P. Flajolet and R. Sedgewick, “Complex analysis, rational and meromorphic asymptotics”, in *Analytic combinatorics* (Cambridge University Press, 2009), 223–288.
- [32] E. Fradkin and L. Susskind, “Order and disorder in gauge systems and magnets”, *Phys. Rev. D* **17**, 2637 (1978).
- [33] D. Gaiotto, A. Kapustin, N. Seiberg, and B. Willett, “Generalized global symmetries”, *J. High Energ. Phys.* **2015**, 172 (2015).
- [34] M. J. P. Gingras, “Spin ice”, in *Introduction to frustrated magnetism: materials, experiments, theory*, edited by C. Lacroix, P. Mendels, and F. Mila (Springer Berlin Heidelberg, Berlin, Heidelberg, 2011), pp. 293–329.
- [35] P. Glorioso, M. Crossley, and H. Liu, “Effective field theory of dissipative fluids (ii): Classical limit, dynamical kms symmetry and entropy current”, *J. High Energ. Phys.* **2017**, 096 (2017).

- [36] P. Glorioso, L. V. Delacrétaz, X. Chen, R. M. Nandkishore, and A. Lucas, “Hydrodynamics in lattice models with continuous non-Abelian symmetries”, *SciPost Phys.* **10**, 015 (2021).
- [37] P. Glorioso, J. Guo, and A. Lucas, “Breakdown of hydrodynamics below four dimensions in a fracton fluid”, *Nature Physics* **18**, 912 (2022).
- [38] P. Glorioso, X. Huang, J. Guo, J. F. Rodriguez-Nieva, and A. Lucas, *Goldstone bosons and fluctuating hydrodynamics with dipole and momentum conservation*, 2023.
- [39] A. Gromov, “Towards classification of fracton phases: the multipole algebra”, *Phys. Rev. X* **9**, 031035 (2019).
- [40] A. Gromov, A. Lucas, and R. M. Nandkishore, “Fracton hydrodynamics”, *Phys. Rev. Research* **2**, 033124 (2020).
- [41] K. T. Grosvenor, C. Hoyos, F. Peña-Benitez, and P. Surówka, “Hydrodynamics of ideal fracton fluids”, *Phys. Rev. Res.* **3**, 043186 (2021).
- [42] S. Grozdanov, A. Lucas, and N. Poovuttikul, “Holography and hydrodynamics with weakly broken symmetries”, *Phys. Rev. D* **99**, 086012 (2019).
- [43] E. Guardado-Sánchez, A. Morningstar, B. M. Spar, P. T. Brown, D. A. Huse, and W. S. Bakr, “Subdiffusion and heat transport in a tilted two-dimensional Fermi-Hubbard system”, *Phys. Rev. X* **10**, 011042 (2020).
- [44] J. Guo, P. Glorioso, and A. Lucas, “Fracton hydrodynamics without time-reversal symmetry”, *Phys. Rev. Lett.* **129**, 150603 (2022).
- [45] J. Haah, “Local stabilizer codes in three dimensions without string logical operators”, *Phys. Rev. A* **83**, 042330 (2011).
- [46] F. M. Haehl, R. Loganayagam, and M. Rangamani, “The fluid manifesto: Emergent symmetries, hydrodynamics, and black holes”, *J. High Energ. Phys.* **2016**, 184 (2016).
- [47] A. Hamma, C. Castelnovo, and C. Chamon, “Toric-boson model: toward a topological quantum memory at finite temperature”, *Phys. Rev. B* **79**, 245122 (2009).
- [48] O. Hart, A. Lucas, and R. Nandkishore, “Hidden quasiconservation laws in fracton hydrodynamics”, *Phys. Rev. E* **105**, 044103 (2022).
- [49] O. Hart and R. Nandkishore, “Hilbert space shattering and dynamical freezing in the quantum Ising model”, *Phys. Rev. B* **106**, 214426 (2022).
- [50] O. Hart, Y. Wan, and C. Castelnovo, “Coherent propagation of quasiparticles in topological spin liquids at finite temperature”, *Phys. Rev. B* **101**, 064428 (2020).
- [51] M. B. Hastings, “Topological order at nonzero temperature”, *Phys. Rev. Lett.* **107**, 210501 (2011).
- [52] M. B. Hastings and J. Haah, “Dynamically generated logical qubits”, *Quantum* **5**, 564 (2021).
- [53] C. L. Henley, “From classical to quantum dynamics at Rokhsar–Kivelson points”, *Journal of Physics: Condensed Matter* **16**, S891 (2004).
- [54] C. L. Henley, “Relaxation time for a dimer covering with height representation”, *Journal of statistical physics* **89**, 483 (1997).
- [55] T. Horiguchi, “Lattice Green’s functions for the triangular and honeycomb lattices”, *Journal of Mathematical Physics* **13**, 1411 (1972).

- [56] A. Hutter, F. L. Pedrocchi, J. R. Wootton, and D. Loss, “Effective quantum-memory hamiltonian from local two-body interactions”, *Physical Review A* **90**, 10.1103/physreva.90.012321 (2014).
- [57] A. Hutter, J. R. Wootton, B. Röthlisberger, and D. Loss, “Self-correcting quantum memory with a boundary”, *Physical Review A* **86**, 10.1103/physreva.86.052340 (2012).
- [58] J. Iaconis, A. Lucas, and R. Nandkishore, “Multipole conservation laws and subdiffusion in any dimension”, *Phys. Rev. E* **103**, 022142 (2021).
- [59] J. Iaconis, S. Vijay, and R. Nandkishore, “Anomalous subdiffusion from subsystem symmetries”, *Phys. Rev. B* **100**, 214301 (2019).
- [60] J. Z. Imbrie, “On many-body localization for quantum spin chains”, *Journal of Statistical Physics* **163**, 998 (2016).
- [61] K. Jensen, N. Pinzani-Fokeeva, and A. Yarom, “Dissipative hydrodynamics in superspace”, *J. High Energ. Phys.* **2018**, 127 (2018).
- [62] K. Jensen and A. Raz, *Large N fractons*, 2022.
- [63] A. Kapustin and L. Spodyneiko, “Hohenberg-Mermin-Wagner-type theorems and dipole symmetry”, *Phys. Rev. B* **106**, 245125 (2022).
- [64] P. W. Kasteleyn, “The statistics of dimers on a lattice: I. The number of dimer arrangements on a quadratic lattice”, *Physica* **27**, 1209 (1961).
- [65] P. W. Kasteleyn, “Dimer statistics and phase transitions”, *Journal of Mathematical Physics* **4**, 287 (1963).
- [66] C. W. von Keyserlingk, F. J. Burnell, and S. H. Simon, “Three-dimensional topological lattice models with surface anyons”, *Phys. Rev. B* **87**, 045107 (2013).
- [67] V. Khemani, M. Hermele, and R. Nandkishore, “Localization from Hilbert space shattering: From theory to physical realizations”, *Phys. Rev. B* **101**, 174204 (2020).
- [68] A. Khudorozhkov, A. Tiwari, C. Chamon, and T. Neupert, “Hilbert space fragmentation in a 2D quantum spin system with subsystem symmetries”, *SciPost Phys.* **13**, 098 (2022).
- [69] A. Kitaev and L. Kong, “Models for gapped boundaries and domain walls”, *Commun. Math. Phys.* **313**, 351 (2012).
- [70] A. Yu. Kitaev, “Fault-tolerant quantum computation by anyons”, *Annals of Physics* **303**, 2 (2003).
- [71] A. Kubica and M. Vasmer, “Single-shot quantum error correction with the three-dimensional subsystem toric code”, *Nat Commun* **13**, 6272 (2022).
- [72] A. Kubica and B. Yoshida, *Ungauging quantum error-correcting codes*, 2018.
- [73] E. Lake, *Higher-form symmetries and spontaneous symmetry breaking*, 2018.
- [74] E. Lake, M. Hermele, and T. Senthil, “Dipolar Bose-Hubbard model”, *Phys. Rev. B* **106**, 064511 (2022).
- [75] O. Landon-Cardinal, B. Yoshida, D. Poulin, and J. Preskill, “Perturbative instability of quantum memory based on effective long-range interactions”, *Phys. Rev. A* **91**, 032303 (2015).
- [76] I. Lesanovsky and H. Katsura, “Interacting Fibonacci anyons in a Rydberg gas”, *Phys. Rev. A* **86**, 041601 (2012).

- [77] Y. Li, C. W. von Keyserlingk, G. Zhu, and T. Jochym-O'Connor, *Phase diagram of the three-dimensional subsystem toric code*, 2023.
- [78] E. H. Lieb, “Exact solution of the problem of the entropy of two-dimensional ice”, *Phys. Rev. Lett.* **18**, 692 (1967).
- [79] E. H. Lieb, “Residual entropy of square ice”, *Phys. Rev.* **162**, 162 (1967).
- [80] C.-J. Lin, V. Calvera, and T. H. Hsieh, “Quantum many-body scar states in two-dimensional Rydberg atom arrays”, *Phys. Rev. B* **101**, 220304 (2020).
- [81] H. Liu and P. Glorioso, “Lectures on non-equilibrium effective field theories and fluctuating hydrodynamics”, in Theoretical advanced study institute summer school 2017 “physics at the fundamental frontier”, Vol. 305 (2018), p. 008.
- [82] H. Ma, E. Lake, X. Chen, and M. Hermele, “Fracton topological order via coupled layers”, *Phys. Rev. B* **95**, 245126 (2017).
- [83] J. McGreevy, “Generalized symmetries in condensed matter”, *Annual Review of Condensed Matter Physics* **14**, 57 (2023).
- [84] A. A. Michailidis, C. J. Turner, Z. Papić, D. A. Abanin, and M. Serbyn, “Stabilizing two-dimensional quantum scars by deformation and synchronization”, *Phys. Rev. Research* **2**, 022065 (2020).
- [85] K. P. Michnicki, “3d topological quantum memory with a power-law energy barrier”, *Phys. Rev. Lett.* **113**, 130501 (2014).
- [86] R Moessner, O. Tchernyshyov, and S. L. Sondhi, “Planar pyrochlore, quantum ice and sliding ice”, *Journal of statistical physics* **116**, 755 (2004).
- [87] R. Moessner and K. S. Raman, “Quantum dimer models”, in *Introduction to frustrated magnetism: Materials, experiments, theory* (Springer, 2010), pp. 437–479.
- [88] S. Moudgalya and O. I. Motrunich, “Hilbert space fragmentation and commutant algebras”, *Physical Review X* **12**, 011050 (2022).
- [89] S. Moudgalya, A. Prem, R. Nandkishore, N. Regnault, and B. A. Bernevig, “Thermalization and its absence within Krylov subspaces of a constrained Hamiltonian”, in *Memorial volume for shoucheng zhang* (World Scientific, 2022), pp. 147–209.
- [90] S. Moudgalya, N. Regnault, and B. A. Bernevig, “Entanglement of exact excited states of Affleck-Kennedy-Lieb-Tasaki models: Exact results, many-body scars, and violation of the strong eigenstate thermalization hypothesis”, *Physical Review B* **98**, 235156 (2018).
- [91] R. Nandkishore and D. A. Huse, “Many-body localization and thermalization in quantum statistical mechanics”, *Annu. Rev. Condens. Matter Phys.* **6**, 15 (2015).
- [92] R. M. Nandkishore and M. Hermele, “Fractons”, *Annu. Rev. Condens. Matter Phys.* **10**, 295 (2019).
- [93] Z. Nussinov and G. Ortiz, “Sufficient symmetry conditions for topological quantum order”, *Proceedings of the National Academy of Sciences* **106**, 16944 (2009).
- [94] Z. Nussinov and G. Ortiz, “A symmetry principle for topological quantum order”, *Annals of Physics* **324**, 977 (2009).
- [95] A. Osborne and A. Lucas, “Infinite families of fracton fluids with momentum conservation”, *Phys. Rev. B* **105**, 024311 (2022).

- [96] S. D. Pace and X.-G. Wen, “Exact emergent higher-form symmetries in bosonic lattice models”, *Phys. Rev. B* **108**, 195147 (2023).
- [97] A. Paetznick and B. W. Reichardt, “Universal fault-tolerant quantum computation with only transversal gates and error correction”, *Phys. Rev. Lett.* **111**, 090505 (2013).
- [98] S. Pai, M. Pretko, and R. M. Nandkishore, “Localization in fractonic random circuits”, *Phys. Rev. X* **9**, 021003 (2019).
- [99] F. L. Pedrocchi, S. Chesi, and D. Loss, “Quantum memory coupled to cavity modes”, *Physical Review B* **83**, 10.1103/physrevb.83.115415 (2011).
- [100] F. L. Pedrocchi, A. Hutter, J. R. Wootton, and D. Loss, “Enhanced thermal stability of the toric code through coupling to a bosonic bath”, *Phys. Rev. A* **88**, 062313 (2013).
- [101] D. Poulin, “Stabilizer formalism for operator quantum error correction”, *Phys. Rev. Lett.* **95**, 230504 (2005).
- [102] A. Prem, J. Haah, and R. Nandkishore, “Glassy quantum dynamics in translation invariant fracton models”, *Phys. Rev. B* **95**, 155133 (2017).
- [103] M. Pretko, “Subdimensional particle structure of higher rank $U(1)$ spin liquids”, *Phys. Rev. B* **95**, 115139 (2017).
- [104] M. Pretko, X. Chen, and Y. You, “Fracton phases of matter”, *Int. J. Mod. Phys. A* **35**, 2030003 (2020).
- [105] S. J. Puterman, “Superfluid hydrodynamics”, Amsterdam **3** (1974).
- [106] M. Qi, O. Hart, A. J. Friedman, R. Nandkishore, and A. Lucas, “Hydrodynamics of higher-rank gauge theories”, *SciPost Phys.* **14**, 029 (2023).
- [107] M. Qi, L. Radzihovsky, and M. Hermele, “Fracton phases via exotic higher-form symmetry-breaking”, *Annals of Physics* **424**, 168360 (2021).
- [108] T. Rakovszky, P. Sala, R. Verresen, M. Knap, and F. Pollmann, “Statistical localization: from strong fragmentation to strong edge modes”, *Phys. Rev. B* **101**, 125126 (2020).
- [109] R. Raussendorf, J. Harrington, and K. Goyal, “A fault-tolerant one-way quantum computer”, *Annals of Physics* **321**, 2242 (2006).
- [110] R. Raussendorf, S. Bravyi, and J. Harrington, “Long-range quantum entanglement in noisy cluster states”, *Phys. Rev. A* **71**, 062313 (2005).
- [111] J. Richter and A. Pal, “Anomalous hydrodynamics in a class of scarred frustration-free Hamiltonians”, *Phys. Rev. Res.* **4**, L012003 (2022).
- [112] S. Roberts and S. D. Bartlett, “Symmetry-protected self-correcting quantum memories”, *Phys. Rev. X* **10**, 031041 (2020).
- [113] S. Roberts and D. J. Williamson, *3-fermion topological quantum computation*, 2020.
- [114] S. Roberts, B. Yoshida, A. Kubica, and S. D. Bartlett, “Symmetry-protected topological order at nonzero temperature”, *Phys. Rev. A* **96**, 022306 (2017).
- [115] D. S. Rokhsar and S. A. Kivelson, “Superconductivity and the quantum hard-core dimer gas”, *Phys. Rev. Lett.* **61**, 2376 (1988).
- [116] P. Sala, J. Lehmann, T. Rakovszky, and F. Pollmann, “Dynamics in systems with modulated symmetries”, *Phys. Rev. Lett.* **129**, 170601 (2022).

- [117] P. Sala, T. Rakovszky, R. Verresen, M. Knap, and F. Pollmann, “Ergodicity Breaking Arising from Hilbert Space Fragmentation in Dipole-Conserving Hamiltonians”, *Phys. Rev. X* **10**, 011047 (2020).
- [118] N. Seiberg, “Field theories with a vector global symmetry”, *SciPost Phys.* **8**, 050 (2020).
- [119] D. Sels and A. Polkovnikov, “Dynamical obstruction to localization in a disordered spin chain”, *Physical Review E* **104**, 054105 (2021).
- [120] N. Shannon, G. Misguich, and K. Penc, “Cyclic exchange, isolated states, and spinon deconfinement in an XXZ Heisenberg model on the checkerboard lattice”, *Phys. Rev. B* **69**, 220403 (2004).
- [121] N. Shiraishi and T. Mori, “Systematic construction of counterexamples to the eigenstate thermalization hypothesis”, *Phys. Rev. Lett.* **119**, 030601 (2017).
- [122] K. Siva and B. Yoshida, “Topological order and memory time in marginally-self-correcting quantum memory”, *Phys. Rev. A* **95**, 032324 (2017).
- [123] C. Stahl, *Self-correction from higher-form symmetry protection on a boundary*, 2022.
- [124] C. Stahl, E. Lake, and R. Nandkishore, “Spontaneous breaking of multipole symmetries”, *Phys. Rev. B* **105**, 155107 (2022).
- [125] C. Stahl and R. Nandkishore, “Symmetry-protected self-correcting quantum memory in three space dimensions”, *Phys. Rev. B* **103**, 235112 (2021).
- [126] D. T. Stephen, O. Hart, and R. M. Nandkishore, *Ergodicity breaking provably robust to arbitrary perturbations*, 2022.
- [127] H. N. Temperley and M. E. Fisher, “Dimer problem in statistical mechanics-an exact result”, *Philosophical Magazine* **6**, 1061 (1961).
- [128] D. Tong, *Gauge theory*, 2018.
- [129] C. J. Turner, A. A. Michailidis, D. A. Abanin, M. Serbyn, and Z. Papić, “Quantum scarred eigenstates in a Rydberg atom chain: entanglement, breakdown of thermalization, and stability to perturbations”, *Phys. Rev. B* **98**, 155134 (2018).
- [130] C. J. Turner, A. A. Michailidis, D. A. Abanin, M. Serbyn, and Z. Papić, “Weak ergodicity breaking from quantum many-body scars”, *Nature Physics* **14**, 745 (2018).
- [131] S. Vijay, *Isotropic layer construction and phase diagram for fracton topological phases*, 2017.
- [132] S. Vijay, J. Haah, and L. Fu, “Fracton topological order, generalized lattice gauge theory, and duality”, *Phys. Rev. B* **94**, 235157 (2016).
- [133] K. Walker and Z. Wang, “(3 + 1)-TQFTs and topological insulators”, *Frontiers of Physics* **7**, 150 (2011).
- [134] F. J. Wegner, “Duality in generalized Ising models and phase transitions without local order parameters”, *Journal of Mathematical Physics* **12**, 2259 (1971).
- [135] X. G. Wen, “Topological orders in rigid states”, *Int. J. Mod. Phys. B* **04**, 239 (1990).
- [136] X.-G. Wen, “Emergent anomalous higher symmetries from topological order and from dynamical electromagnetic field in condensed matter systems”, *Phys. Rev. B* **99**, 205139 (2019).
- [137] J. R. Wootton, “Topological phases and self-correcting memories in interacting anyon systems”, *Physical Review A* **88**, 10.1103/physreva.88.062312 (2013).

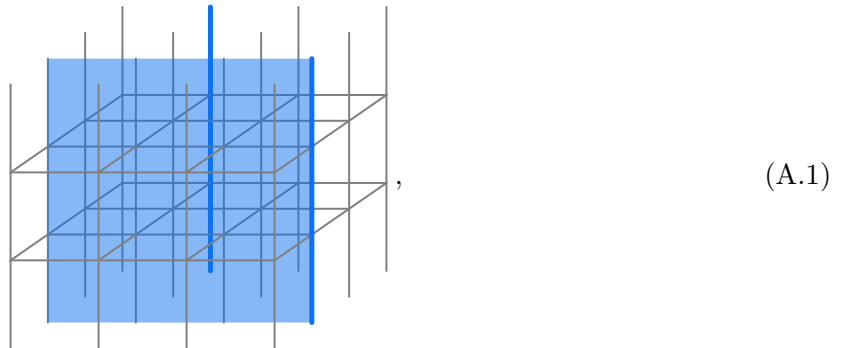
- [138] Z.-C. Yang, F. Liu, A. V. Gorshkov, and T. Iadecola, “Hilbert-space fragmentation from strict confinement”, [Phys. Rev. Lett. **124**, 207602 \(2020\)](#).
- [139] A. Yoshinaga, H. Hakoshima, T. Imoto, Y. Matsuzaki, and R. Hamazaki, “Emergence of Hilbert space fragmentation in Ising models with a weak transverse field”, [Phys. Rev. Lett. **129**, 090602 \(2022\)](#).
- [140] J.-K. Yuan, S. A. Chen, and P. Ye, “Fractonic superfluids”, [Phys. Rev. Research **2**, 023267 \(2020\)](#).

Appendix A

More boundary conditions for the intertwined toric code

As promised, we here define the e -condensed and m -condensed boundary conditions so that the ITC can be defined with a single logical qubit on a cubic lattice that is itself a cube (with no periodic boundary conditions).

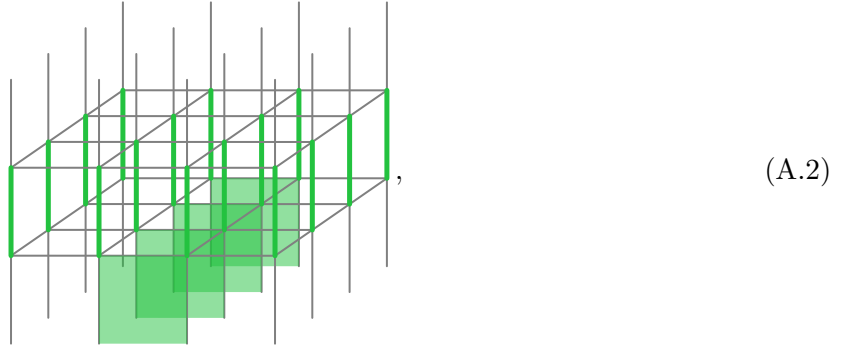
We put the e -condensed boundary on the top and bottom of the cube. To do so, start with the previously-defined trivial boundary and remove qubits from the boundary edges. We are left with the same B_e check operators but some B_f check operators are truncated to 3-body operators, which we leave in the check group. Now there are no boundary A_v stabilizers, but we keep the 5-body A_c stabilizers. On this boundary, the bare logical membrane operator \bar{Z} and the dressed logical stringlike operator Z' may both terminate,



but the X -type logical operators may not.

To construct the m -condensed boundary on the front and back of the cube, once again start with the trivial boundary. Now, add qubits to every boundary face. For every boundary edge

we can now define a 3-body B_e operator. We also define single-body Z_f operators on these new face qubits. The resulting stabilizers are the 5-body A_v operators we already had and new 6-body $A_c = \prod_{f \in \partial c} Z_f$ operators. The bare logical membrane operator \bar{X} and the dressed logical stringlike operator \bar{X}' may both end on this boundary,



but the Z -type logical operators may not.

These boundaries result in a cleaner code because they only encode a single logical qubit. There are $3L^3 + 2L^2 - L$ edges and $3L^3 - L^2$ faces for a total of $6L^3 + L^2 - L$ physical qubits. On these qubits we enforce $3L^3 - 3L$ single-site X_e check operators, $2L^2 + 2L$ of the K_e check operators (only counting those on the intertwined boundary), and $3L^3 - L^2$ single-site Z_f check operators. Between $3L^3 + L^2$ total B_f check operators we have L^3 relations and therefore $2L^3 + L^2$ independent B_f operators. There are $3L^3 - 2L^2 - L$ total B_e check operators with $L^3 - L^2 - L + 1$ relations between them, giving $2L^3 - L^2 - 1$ independent B_e operators. Along with $L^3 + L^2 - L - 1$ of the A_v stabilizers and L^3 of the A_c , we have

$$K = N - \frac{1}{2} (\log_2 |\mathcal{G}| + \log_2 |\mathcal{S}|) = 1 \quad (\text{A.3})$$

logical qubit.

We should think of this as the minimal intertwined toric code because it only encodes a single logical qubit and has no need for periodic boundary conditions. We can go through the analysis of Sec. 4.4 to see what these boundaries become in the different phases. For example, the e -condensed

boundary becomes the rough boundary conditions for the 2d toric code in the paramagnetic phase and for the 3d toric code in the TCE phase.

Appendix B

Appendices to Hydrodynamics

B.1 Quasihydrodynamics

To study the quasihydrodynamics mentioned in the main text, we need to choose a parameter to tune to be small. For the transition from the charge condensate into the dipole condensate, we will reintroduce the coefficients κ_1^ϕ and $\kappa^{\phi\psi}$ (κ_2^ϕ , g_2 , and g_3 will all be subleading). This gives a longitudinal continuity equation,

$$0 = \omega^2 + i \frac{\kappa_1^\psi}{\kappa_1^\phi - i\omega\sigma} \omega^2 k^2 - \frac{\kappa^{\phi\psi} + \kappa^\psi}{\chi} k^4, \quad (\text{B.1})$$

with $\kappa^\psi = \kappa_1^\psi + \kappa_2^\psi$ as before. This dispersion defines a time scale $\tau = \sigma/\kappa_1^\phi$. After this time, the dispersion is $\omega^2 = (\kappa^{\phi\psi} + \kappa^\psi)k^4/\chi$, reproducing the charge condensate. This shows that we are truly in the charge condensate. Before this scale, the dispersion looks like the dipole condensate (compare to (5.25)). There is no transverse mode in the charge condensate, even near the dipole condensate transition.

We can better understand (B.1) by looking at plots of the dispersion. In Fig. 5.2 we can see the dispersion with $\kappa^\psi\chi/\sigma^2 = 25$ chosen to place us firmly within the diffusive regime. At small k (true hydrodynamics) the dispersion looks like the charge condensate with $\omega^2 \sim k^4$, with an additional gapped mode. At large k (quasihydrodynamics) it looks like the diffusive regime of the dipole condensate ($\omega \sim -ik^2$). One of the diffusive modes becomes gapped at small k , while the other diffusive mode collides with the large- k gapped mode to give the propagating modes.

Fig. 5.2 also shows the dispersions at a value of $\kappa^\psi \chi / \sigma^2 = 1$ (recall the critical value is 4).

The propagating modes at small k become the propagating modes at large k , with no collision. There is an extra mode that is gapped at large and small k . This mode is not a hydrodynamic or quasihydrodynamic mode, but it cannot be removed from the analysis because it is the same mode that goes from diffusive to gapped in the other regime.

To study the small- T regime of the dipole condensate, let us revisit (5.20) in the small- σ limit. This allows us to retain ρ_i in the continuity equations, with the important contribution being $\rho_i = \chi^\psi \partial_t \psi_i$. The transverse part of the dipole continuity equation reads

$$0 = \chi^\psi \partial_t^2 \psi_i^t + \sigma \partial_t \psi_i^t - (\kappa_2^\psi - g_2) \nabla^2 \psi_i^t, \quad (\text{B.2})$$

with solution

$$\omega = \frac{-i\sigma}{2\chi^\psi} \pm \sqrt{\frac{-\sigma^2}{2(\chi^\psi)^2} + \frac{(\kappa_2^\psi - g_2)k^2}{\chi^\psi}}, \quad (\text{B.3})$$

introducing a timescale $\tau = \chi^\psi / \sigma$. The new timescale τ is large in the small- σ limit. On timescales smaller than τ the quasihydrodynamics consists of a linear propagating mode,

$$\omega = \pm \sqrt{\frac{(\kappa_2^\psi - g_2)k^2}{\chi^\psi}}, \quad (\text{B.4})$$

matching the $T = 0$ expectation. At timescales larger than τ the propagating mode splits into a gapped mode and a diffusive mode with diffusion constant $(\kappa_2^\psi - g_2)/\sigma$, as in (5.23).

With the introduction of χ^ψ , the analog of 5.24 is

$$0 = \begin{bmatrix} \chi \partial_t - \sigma \nabla^2 & \sigma \partial_t \\ -\sigma \nabla^2 & \chi^\psi \partial_t + \sigma \partial_t - \kappa^\psi \nabla^2 \end{bmatrix} \begin{pmatrix} \partial_t \phi \\ \nabla_j \psi_j \end{pmatrix}, \quad (\text{B.5})$$

with the same timescale $\tau = \chi^\psi/\sigma$. In the small- σ limit, the solutions are

$$\omega = -i\frac{\sigma}{\chi}k^2, \quad \omega = \frac{-i\sigma}{2\chi^\psi} \pm \sqrt{\frac{-\sigma^2}{2(\chi^\psi)^2} + \frac{\kappa^\psi k^2}{\chi^\psi}}. \quad (\text{B.6})$$

The first solution matches one of the diffusion modes from the dipole condensate phase, with a diffusion constant that vanishes in the small- σ limit. The other mode behaves like the transverse mode, transitioning from linear propagation in quasihydrodynamics to a gapped mode and a diffusive mode in the late-time hydrodynamics. These modes are shown in Fig. 5.3.

The above analysis shows that the dissipative coefficient σ is crucial in that it completely changes the nature of the dispersion relation from $T = 0$ to finite T , going from a ballistic to a quadratic scaling. While we determined the presence of this transport coefficient in terms of simple symmetry arguments, we note that this term can be argued to be finite based on microscopic reasoning. Consider a lattice model described by a complex boson $b_{\mathbf{x}}$ and with dipole symmetry $b_{\mathbf{x}} \rightarrow b_{\mathbf{x}} e^{i\alpha \cdot \mathbf{x}}$. In the condensed dipole phase, hopping of a single boson is allowed through the term $b_{\mathbf{x}} b_{\mathbf{x}+\mathbf{e}_j} e^{i\psi_j} + \text{h.c.}$, where \mathbf{e}_j denotes a unit vector in the j -direction [74]. Note that ψ_i can exactly be viewed as a spatial gauge field $A_i = \psi_i$. Treating ψ_i as a background non-dynamical field, at finite temperature, this coupling will generically lead to a finite conductivity term in the current $J_i = \sigma E_i = \sigma \partial_t \psi_i$, which is precisely the last term in the third line of (5.20). This argument not only confirms that σ *must* generically be finite, it also shows that, given a $U(1)$ -invariant system without dipole symmetry, this can be straightforwardly extended to a dipole symmetric system in the dipole condensed phase.

B.2 Derivation of the effective action

The effective actions we consider must obey the KMS symmetry in (5.10). Ref. [63] shows that we can construct KMS-invariant terms in two distinct ways, which correspond to dissipative

and nondissipative terms in the effective action. The nondissipative terms are

$$\mathcal{L}_{\text{nd}} = \left(\Phi \frac{\delta}{\delta \phi} + \Psi_i \frac{\delta}{\delta \psi_i} \right) \int d^3x dt \Omega, \quad (\text{B.7})$$

where Ω is a Lagrangian that depends on ϕ and ψ_i but not on Φ or Ψ_i . Thermodynamic stability of the effective action requires that Ω is negative when Wick-rotated. The dissipative terms are

$$\mathcal{L}_{\text{d}} = \frac{1}{2} (X(\phi, \psi_i, \Phi, \Psi_i) + X_{\text{KMS}}(\phi, \psi_i, \Phi, \Psi_i) - X(\phi, \psi_i, 0, 0) - X_{\text{KMS}}(\phi, \psi_i, 0, 0)), \quad (\text{B.8})$$

where X is quadratic in Φ and Ψ_i and is even under time-reversal. The function X_{KMS} is the result of the transformation in (5.10) applied to X .

For the nondissipative part, we will consider terms of order ω^2 , $\omega^2 k^2$, k^2 , and k^4 . This is not a strictly valid gradient expansion at any value of z , but will give us all the terms we need for our analysis. Then, we have

$$\begin{aligned} 2\Omega = & \chi(\partial_t \phi)^2 + \chi_2^\phi (\partial_t \nabla_i \phi)^2 + 2g_1 \partial_t \nabla_i \phi \partial_t \psi_i + \chi^\psi (\partial_t \psi_i)^2 - \kappa_1^\phi (\nabla_i \phi - \psi_i)^2 \\ & - \kappa_2^\phi (\nabla_i \nabla_j \phi)^2 - 2g_2 \nabla_i \nabla_j \phi \nabla_i \psi_j - 2g_3 \nabla^2 \phi \nabla_i \psi_i - \tilde{\kappa}_2^\psi (\nabla_i \psi_j)^2 - \tilde{\kappa}_1^\psi (\nabla_i \psi_i)^2, \end{aligned} \quad (\text{B.9})$$

where we have included various factors of 2 for convenience. All χ and κ coefficients must be nonnegative. The g coefficients may be positive or negative, but must obey the stability conditions $|g_1| \leq \min(\chi_2^\phi, \chi^\psi)$, $|g_2| \leq \min(\kappa_2^\phi, \tilde{\kappa}_2^\psi)$, $|g_3| \leq \min(\kappa_2^\phi, \tilde{\kappa}_1^\psi)$, and $|g_2 + g_3| \leq \kappa_2^\phi$. The Lagrangian

becomes

$$\begin{aligned}
\mathcal{L}_{\text{nd}} &= \left[\chi \partial_t \phi - \chi_2^\phi \partial_t \nabla^2 \phi - g_1 \partial_t \nabla_i \psi_i \right] \partial_t \Phi \\
&\quad + \left[g_1 \partial_t \nabla_i \phi + \chi^\psi \partial_t \psi_i \right] \partial_t \Psi_i \\
&\quad + \left[-\kappa_1^\phi (\nabla_i \phi - \psi_i) \right] (\nabla_i \Phi - \Psi_i) \\
&\quad + \left[-\kappa_2^\phi \nabla_i \nabla_j \phi - g_2 \nabla_i \psi_j - g_3 \delta_{ij} \nabla_k \psi_k \right] \nabla_i \nabla_j \Phi \\
&\quad + \left[-g_2 \nabla_i \nabla_j \phi - g_3 \delta_{ij} \nabla^2 \phi - \tilde{\kappa}_2^\psi \nabla_i \psi_j - \tilde{\kappa}_1^\psi \delta_{ij} \nabla_k \psi_k \right] \nabla_i \Psi_j \\
&= \left[\chi \partial_t \phi - \chi_2^\phi \partial_t \nabla^2 \phi - g_1 \partial_t \nabla_i \psi_i \right] \partial_t \Phi \\
&\quad + \left[g_1 \partial_t \nabla_i \phi + \chi^\psi \partial_t \psi_i \right] \partial_t \Psi_i \\
&\quad + \left[-\kappa_1^\phi (\nabla_i \phi - \psi_i) + \kappa_2^\phi \nabla^2 \nabla_i \phi + g_2 \nabla^2 \psi_i + g_3 \nabla_i \nabla_j \psi_j \right] (\nabla_i \Phi - \Psi_i) \\
&\quad - \left[(\kappa_2^\phi + g_2 + g_3) \nabla_i \nabla_j \phi + (\tilde{\kappa}_1^\psi + g_3) \nabla_i \psi_j + (\tilde{\kappa}_2^\psi + g_2) \nabla_j \psi_i \right] \nabla_j \Psi_i, \tag{B.10}
\end{aligned}$$

where we used $\nabla_i \nabla_j \Phi = \nabla_i (\nabla_j \Phi - \Psi_j) + \nabla_i \Psi_j$ and integration by parts. Note the sign and order of indices in the last line, chosen to match the convention in (5.7). We can identify the new coefficients $\kappa^{\phi\psi} = \kappa_2^\phi + g_2 + g_3$, $\kappa_1^\psi = \tilde{\kappa}_1^\psi + g_3$, and $\kappa_2^\psi = \tilde{\kappa}_2^\psi + g_2$, all of which are nonnegative.

The dissipative terms we need for our analysis descend from the expression

$$2\beta X = ib_0 (\nabla_i \Phi - \Psi)^2 + ib_1 (\nabla_i \nabla_j \Phi)^2 + 2i\xi \nabla_i \nabla_j \Phi \nabla_i \Psi_j + 2i\xi_2 \nabla^2 \Phi \nabla_i \Psi_i + ib_2 (\nabla_i \Psi_j)^2 + ib_3 (\nabla_i \Psi_i)^2, \tag{B.11}$$

where the b coefficients must be positive and $|\xi_1| \leq \min(b_1, b_2)$, $|\xi_2| \leq \min(b_1, b_3)$, and $|\xi_1 + \xi_2| \leq b_1$

by (5.9). Then,

$$\begin{aligned}
\mathcal{L}_d &= X - b_0 \partial_t (\nabla_i \phi - \psi_i) (\nabla_i \Phi - \Psi_i) \\
&\quad - [b_1 \partial_t \nabla_i \nabla_j \phi + \xi_1 \partial_t \nabla_i \psi_j + \xi_2 \delta_{ij} \partial_t \nabla_k \psi_k] \nabla_i \nabla_j \Phi \\
&\quad - [\xi_1 \partial_t \nabla_i \nabla_j \phi + \xi_2 \delta_{ij} \partial_t \nabla^2 \phi + b_2 \partial_t \nabla_i \psi_j + b_3 \delta_{ij} \partial_t \nabla_k \psi_k] \nabla_i \Psi_j \\
&= X + [-b_0 \partial_t (\nabla_i \phi - \psi_i) + b_1 \partial_t \nabla^2 \nabla_i \phi + \xi_1 \partial_t \nabla^2 \psi_i + \xi_2 \partial_t \nabla_i \nabla_j \psi_j] (\nabla_i \Phi - \Psi_i) \\
&\quad - [(b_1 + \xi_1 + \xi_2) \partial_t \nabla_i \nabla_j \phi + (b_2 + \xi_1) \partial_t \nabla_i \psi_j + (b_3 + \xi_2) \delta_{ij} \partial_t \nabla_k \psi_k] \nabla_i \Psi_j, \tag{B.12}
\end{aligned}$$

from which we can identify $\sigma = b_0$, $B_1 = b_1 + \xi_1 + \xi_2$, $B_2 = b_2 + \xi_1$, and $B_3 = b_3 + \xi_2$. The other terms end up being sub-leading so we may drop them. The terms in X itself are quadratic in Φ and Ψ_i , so they contribute to the fluctuating hydrodynamics but can be ignored for the purpose of computing the dispersion relations.

Appendix C

Appendix to Robust shattering

C.1 Additional dualities

Here, we describe a further duality of the two-dimensional models (6.17) and (6.32), which involves introducing two degrees of freedom per face that correspond to domain wall variables between spins belonging to the same sublattice. That is, a spin situated at a vertex with coordinates (x, y) belongs to the even (odd) sublattice if $x + y$ is even (odd). The introduction of these new degrees of freedom is motivated by Eq. (6.30), which requires that, around a given face, the two spins on the even sublattice must match, or the two spins on the odd sublattice must match (or both). Explicitly, given four vertices around a face, v_1, v_2, v_3 , and v_4 (no ordering implied), with v_1, v_3 belonging to the even sublattice, and v_2, v_4 to the odd sublattice, we construct domain wall variables $\hat{\tau}_{f,+}^z = \hat{Z}_{v_1}^\dagger \hat{Z}_{v_3}$ and $\hat{\tau}_{f,-}^z = \hat{Z}_{v_2}^\dagger \hat{Z}_{v_4}$. In this language, the constraint is particularly simple:

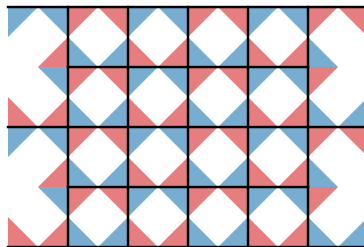
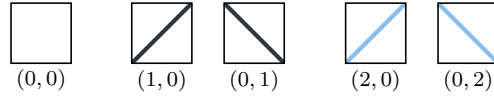


Figure C.1: The sign convention that we introduce to define domain wall variables of the form $\hat{Z}_i^\dagger Z_j$ living on faces, which correspond to domain walls amongst even sublattice spins and amongst odd sublattice spins. Vertices that contribute a Z (Z^\dagger) to the domain wall degree of freedom on a given face are denoted by red (blue) shaded regions. This choice affects the local constraints that any domain wall configuration must satisfy.

On any face f , domain walls (defined by $\tau_{f,s}^z \neq 1$) cannot intersect.

For $m > 2$, the \widehat{Z}_v operators are not Hermitian, so there exists a choice in which \widehat{Z} operators are conjugated. Illustrating those vertices that contribute a \widehat{Z} (\widehat{Z}^\dagger) by red (blue) shaded regions, the convention that we utilize is illustrated in Fig. C.1. In principle, there are $m - 1$ species of domain wall per sublattice. However, when illustrating spin configurations we choose not to distinguish between domain walls on the even and odd sublattices. The configurations on faces for $m = 3$ consistent with the constraint are:



where the labels denote $(\alpha_{f,+}, \alpha_{f,-})$ assuming the top left and bottom right vertices belong to the even sublattice (for a given face and sublattice, α is defined by $\tau^z = e^{2\pi i \alpha/m}$). The convention in Fig. C.1 enforces constraints on the colors of domain walls on adjacent faces. Namely, the domain wall variables on the four faces around a vertex v , belonging to sublattice s , satisfy $\prod_{f \in v} \widehat{\tau}_{f,-s}^z = \mathbb{1}$, equivalent to $\sum_{f \in v} \alpha_{f,-s} = 0 \pmod{m}$. Graphically, a domain wall will therefore change color at every vertex, unless it branches or meets another domain wall (at a vertex), as shown in Fig. 6.4c.

C.2 Enumerating sectors and frozen states

C.2.1 Krylov sectors in the pair-flip model

The Bethe lattice mapping presented in Fig. 6.1 can also be applied in 1D to facilitate the counting of labels and Krylov sector dimensions [18, 88]. The ‘final’ position on the Bethe lattice after traversing the entire system from left to right, having begun at the root node of the Bethe lattice, is in one-to-one correspondence with the label introduced in Sec. 6.2, which identifies distinct Krylov sectors in the 1D pair-flip model with open boundaries. Similarly, each walk is in one-to-one correspondence with a spin configuration. Hence, the number of spin configurations that map to the same label (with length ℓ) is equal to the number of walks of length L that reach a given point with depth ℓ on the Bethe lattice (note that this number will depend only on ℓ). The number of

such walks $G_L^{(\ell)}$ – equal to the dimension of the Krylov sector for a label of length ℓ – is enumerated by the generating functions found in Refs. [18, 50]:

$$G^{(\ell)}(x) = \sum_{L=0}^{\infty} G_L^{(\ell)} x^L = \left(\frac{1 - \sqrt{1 - 4(m-1)x^2}}{2(m-1)x} \right)^{\ell} \frac{2(m-1)}{m-2 + m\sqrt{1 - 4(m-1)x^2}}. \quad (\text{C.1})$$

Note that $G^{(\ell)}(x)$ enforces that $G_L^{(\ell)} = 0$ if ℓ and L have opposite parity, as is required. The number of sites on the Bethe lattice that are accessible after L steps is given by Eq. (6.7). The exponential growth the Krylov sector dimension $G_L^{(\ell)}$ is determined directly (up to subexponential factors) by the radius of convergence of Eq. (C.1) [31]. Specifically, we have

$$G_L^{(\ell)} \sim (2\sqrt{m-1})^L \quad (\text{C.2})$$

as $L \rightarrow \infty$ for fixed ℓ . Insight into the subexponential factors can be obtained by performing a singularity analysis of Eq. (C.1) [18, 30, 31]. Expanding around the singularities at $x = \pm 2\sqrt{m-1}$, we find that

$$G_L^{(\ell)} = 2 \left(\ell + \frac{m}{m-2} \right) \frac{m-1}{m-2} \sqrt{\frac{2}{\pi L^3}} 2^L \sqrt{m-1}^{L-\ell} [1 + \mathcal{O}(L^{-1})], \quad (\text{C.3})$$

as $L \rightarrow \infty$ for fixed, $\mathcal{O}(1)$ values of ℓ . This result shows that, at least for $m > 2$, sectors with larger label lengths ℓ are exponentially suppressed in size with respect to the $\ell = 0$ sector. Additionally, we can deduce that no Krylov sector grows faster than $(2\sqrt{m-1})^L$ as $L \rightarrow \infty$.

We can also write down a generating function that counts the number of labels belonging to each *symmetry sector*. That is, using this generating function, we can deduce into how many Krylov sectors a particular symmetry sector decomposes. To do this, we must account for the U(1) charges associated with each of the m colors. Let the generating variables $\mathbf{y} = \{y_\alpha\}$ keep track of the charge N^α defined in Eq. (6.2). Restricting to $m = 3$ for simplicity, we can then introduce the

two transfer matrices [the row (column) index corresponds to the current (previous) step]

$$T_\sigma = x \begin{pmatrix} 0 & y_r^\sigma & y_r^\sigma \\ y_g^\sigma & 0 & y_g^\sigma \\ y_b^\sigma & y_b^\sigma & 0 \end{pmatrix}, \quad (\text{C.4})$$

with $\sigma = \pm 1$. More generally, the transfer matrix will be an $m \times m$ matrix with the above structure; the zeros along the diagonal enforce that the color of a given dot cannot match the color of the previous dot in the label. The sign σ corresponds to whether an even or an odd edge is being traversed, which add to or subtract from the corresponding U(1) charge. The generating variable x records the length of the label. For open boundary conditions, the full generating function admits the expansion

$$F(x; \mathbf{y}) = 1 + \sum_{i=1}^m (T_0 + T_- T_0 + T_+ T_- T_0 + T_- T_+ T_- T_0 + \dots)_i, \quad (\text{C.5})$$

where the initial condition $T_0 = x(y_r, y_g, y_b)^T$ corresponds to the first (unconstrained) dot, which we assume belongs to the even sublattice. In the presence of periodic boundaries, an analogous expression can be obtained by removing the initial condition T_0 and replacing the sum over i by a trace. Factoring out the repeating combination $T_+ T_-$, we find that

$$F(x; \mathbf{y}) = 1 + \sum_{i=1}^m \sum_{\ell=1}^{\infty} [(\mathbb{1} + T_-)(T_+ T_-)^{\ell-1} T_0]_i \quad (\text{C.6a})$$

$$= 1 + \sum_{i=1}^m [(\mathbb{1} + T_-)(\mathbb{1} - T_+ T_-)^{-1} T_0]_i. \quad (\text{C.6b})$$

where we used $\sum_{n=0}^{\infty} A^n = (\mathbb{1} - A)^{-1}$, which is convergent if the spectral radius of the matrix A is strictly less than unity. The matrix inverse in Eq. (C.6b) can be evaluated exactly to arrive at the

expression

$$F(x; \mathbf{y}) = \frac{(1-x^2) [1+x(y_r+y_g+y_b)+2x^2]}{1+x^2+4x^4-x^2 \left[\frac{y_r}{y_g} + \frac{y_r}{y_b} + \frac{y_g}{y_b} + \frac{y_g}{y_r} + \frac{y_b}{y_r} + \frac{y_b}{y_g} \right]}. \quad (\text{C.7})$$

As required, throwing away the information about the U(1) charges reduces to $F(x; \mathbf{1}) = (1+x)/(1-2x)$, with coefficients $3 \times 2^{n-1}$ for $n \geq 1$, equal to the total number of labels of length n .

Performing the same procedure for case $m = 2$ provides another simple example:

$$\frac{y_r y_b (1-x^2) [1+x(y_r+y_b)+x^2]}{(x^2 y_r - y_b) (x^2 y_b - y_r)} = 1 + \sum_{n=1}^{\infty} \frac{y_r^n + y_b^n}{(y_r y_b)^{\lfloor n/2 \rfloor}} x^n, \quad (\text{C.8})$$

since there is only one label associated with each symmetry sector.

Returning to $m = 3$, let us evaluate the total number of labels that live in the symmetry sector with vanishing charge for all three colors, $N^\alpha = 0$. Such “uncharged” labels are also useful for constructing labels of arbitrary length compatible with a given set of symmetry quantum numbers: Given a label belonging to the appropriate sector, an uncharged label can be appended or prepended (subject to the constraint that neighbors may not match) to produce new labels belonging to the same sector. To extract the generating function of uncharged labels, we are required to evaluate the integral

$$\int_{-\pi}^{\pi} \frac{d\phi_r d\phi_g d\phi_b}{(2\pi)^3} \frac{(1-x^2) [1+x(e^{i\phi_r} + e^{i\phi_g} + e^{i\phi_b})+2x^2]}{1+x^2+4x^4-2x^2 [\cos(\phi_r - \phi_g) + \cos(\phi_g - \phi_b) + \cos(\phi_b - \phi_r)]}. \quad (\text{C.9})$$

The number of labels belonging to other symmetry sectors can be obtained similarly by first multiplying by $\exp(-i \sum_\alpha \phi_\alpha N^\alpha)$. We can make progress by shifting (say) $\phi_{g,b} \rightarrow \phi_{g,b} + \phi_r$, making the integral over ϕ_r trivial. Additionally, we define the function $E(x) = (1+x^2+4x^4)/x^2$ and restructure the trigonometric functions, which brings the integral into the form

$$\frac{(1-x^2)(1+2x^2)}{x^2} \int_{-\pi}^{\pi} \frac{dk_1 dk_2}{(2\pi)^2} \frac{1}{E(x) - 2 \left[\cos(k_1) + 2 \cos(\frac{k_1}{2}) \cos(\frac{k_1}{2} - k_2) \right]}. \quad (\text{C.10})$$

This integral is equal to the Green’s function of a single tight-binding quantum particle hopping on a

triangular lattice [55], for which (in appropriate coordinates) the dispersion relation may be written $E(\mathbf{k}) = 2 \left[\cos(k_1) + 2 \cos(\frac{k_1}{2}) \cos(\frac{k_1}{2} - k_2) \right]$. We can therefore write down an exact expression for the generating function of uncharged configurations

$$F_0(x) \equiv [y_r^0 y_g^0 y_b^0] F(x; \mathbf{y}) = \frac{2(1-x^2)(1+2x^2)}{\pi x^2 (\lambda-1)^{3/2} (\lambda+3)^{1/2}} K \left(\frac{4\lambda^{1/2}}{(\lambda-1)^{3/2} (\lambda+3)^{1/2}} \right), \quad (\text{C.11})$$

where $K(x)$ is the complete elliptic integral of the first kind and we have introduced $\lambda(x) = \sqrt{3+E(x)}$. The first few pattern lengths that belong to the uncharged symmetry sector that derive from Eq. (C.11) are

$$F_0(x) = 1 + 6x^6 + 6x^8 + 42x^{10} + 120x^{12} + 426x^{14} + \dots \quad (\text{C.12})$$

The shortest uncharged pattern has length six and corresponds to a three-dot pattern repeated twice, such as $|\bullet \bullet \bullet \bullet \bullet \bullet \rangle$. The six labels of length $\ell = 8$ are the same six labels as $\ell = 6$ surrounded by the unique color that is not equal to the first or last color in the corresponding $\ell = 6$ label. Asymptotically, the number of patterns of length ℓ within the uncharged symmetry sector scales (up to polynomial corrections) as $\sim 2^\ell$.

Lastly, we note that fragmentation in the PF model is *strong* [67, 117]: In the thermodynamic limit, an arbitrary state chosen from any fixed symmetry sector (i.e., one whose charge does not scale with L) belongs to that sector's largest Krylov sector with probability zero. To see this, recall that any symmetry sector has a minimal length L_{\min} on which it exists. To bound the size of the symmetry sector, we can then place any uncharged spin configuration on the remainder of the system. For $m = 3$ and systems of length $L = L_{\min} + 6n$, we can place n red spins, n blue spins, and n green spins on the even sublattice (and similarly for the odd sublattice), giving

$$D_0^{\text{sym}} > \left[\frac{(3n)!}{(n!)^3} \right]^2 \sim \frac{3^{6n+1}}{4\pi^2 n^2} \quad (\text{C.13})$$

uncharged spin configurations. Hence, every fixed symmetry sector has a dimension that scales

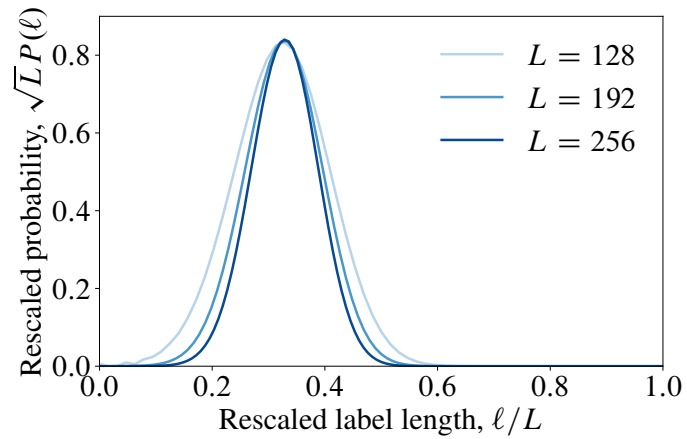


Figure C.2: Exact distribution of Krylov sectors in the uncharged symmetry sector, obtained from the generating functions (C.1) and (C.11). $P(\ell)$ is the probability that a state drawn at random from the uncharged symmetry sector with uniform probability belongs to a Krylov sector corresponding to label length ℓ . The largest Krylov sector, which corresponds to label length $\ell = 0$, represents a vanishingly small fraction of the symmetry sector.

asymptotically as $\sim 3^{L-L_{\min}}$ up to polynomial corrections, while no Krylov sector grows faster than $\sim (2\sqrt{2})^L$ (C.2). For larger m , symmetry sectors contain $\sim m^L$ states, while no Krylov sector grows faster than $\sim (2\sqrt{m-1})^L$. This result is illustrated for the uncharged symmetry sector in Fig. C.2, which shows that an arbitrary state is most likely to belong to a Krylov sector of intermediate size, and that the probability of belonging to any particular Krylov sector vanishes in the thermodynamic limit.

C.2.2 Labels in 1D with periodic boundaries

Let us consider PF dynamics with periodic boundaries. The procedure for finding the label is the same, except that spins on the left and right ends of the system may be paired so that the first and last spin in the label must not match. For labels of size L this is the end of the story; there are $(m-1)^L + (-1)^L(m-1)$ such sectors, the number of m -colorings of the cycle C_L . Each sector consists of a single frozen state.

For shorter labels, the dots are mobile, in the sense of Eq. (6.5). This allows us to cyclicly translate the label by a distance of two. Instead of just keeping track of the length of the label ℓ , let us also keep track of the shortest repeating pattern (“motif”) in a label and its length j . A motif can be repeated up to $n = \lfloor L/j \rfloor$ times. For j odd, a nonfrozen sector is labeled by a motif and a choice of n . For j even (which can only occur if L is even), a nonfrozen sector is labeled by a motif, n , and a choice of parity bit, since the label can only be shifted two positions at a time. Note that we could extend this labeling to frozen states if we supplement with a starting position within the motif, of which there are j .

The number of motifs of length j is given by the recurrence relation

$$N_j^{\text{motif}} = (m-1)^j + (-1)^j(m-1) - \sum_{k|j} N_k^{\text{motif}}, \quad (\text{C.14})$$

where $k|j$ means k divides j . The subtraction removes motifs that are periodic with period k . Asymptotically, we have $N_j^{\text{motif}} \sim (m-1)^j$. Explicit expressions for the subleading corrections can

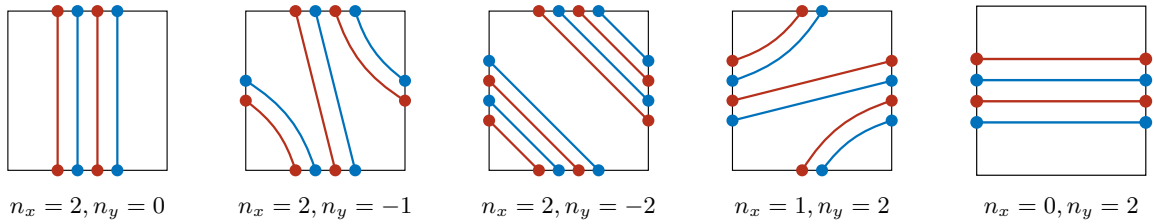


Figure C.3: In 2D, we can choose to repeat a particular motif (in this case, $|\bullet\bullet\rangle$) an integer number of times both horizontally and vertically. For example, in the left-most figure the motif is repeated $n_x = 2$ times horizontally and $n_y = 0$ times vertically. In the middle figure we have $n_y = -2$ because the label is reversed when read from top to bottom. We could in addition have states with $n_x > 2$ or $n_y > 2$, with an upper limit set by $L/2$ (L/j in general).

be found when j is a power of a prime, but are not particularly illuminating. Then, the number of labels of length ℓ is dominated by labels with a single motif, and also scales as $(m - 1)^\ell$. But, since the dots are mobile, sectors correspond to labels up to translation by 2. For odd j , translations by 2 are fully general so that any two motifs related by translation correspond to the same sector when repeated n times. This tells us there are $\sim (m - 1)^\ell/\ell$ sectors with label of length ℓ . If j is even then two motifs that are related by a translation by one cannot be transformed into each other. This means that sectors must have an additional parity bit which introduces a factor of 2 into the counting, but does not affect the scaling.

This all tells us that despite having $\sim (m - 1)^L$ frozen states, the PF model with periodic boundary conditions asymptotically has only $\sim (m - 1)^L/L$ nonfrozen sectors. This contrasts with open boundary conditions, where we found $\sim (m - 1)^L$ frozen sectors and $\sim (m - 1)^L$ nonfrozen sectors.

C.2.3 Labels in 2D with periodic boundaries

The labeling procedure in 2D with PBC is more complicated still, but does have some nice graphical interpretation. We now have the option of choosing a motif with length j and two integers, n_x and n_y , such that $\max(|jn_x|, |jn_y|) \leq L$. Then the horizontal label is the motif repeated n_x times (from left to right) and the vertical label is the motif repeated n_y times (from top to bottom). Negative values correspond to repeating the motif in reverse. A sector consists of a single frozen

state if either $j n_x = L$ or $j n_y = L$. Such states are discussed in Sec. C.2.4. Here, we will focus on nonfrozen sectors.

Different choices of n_x and n_y define how many times a motif is repeated horizontally and vertically. These values also define the average slope of the noncontractible loops: The average slope is $\pm n_x/n_y$. Figure C.3 demonstrates how a particular motif can be included different numbers of times either horizontally or vertically.

As in 1D, two nonmaximal labels related by translation (by two) belong in the same sector. This means there are once again only $\sim (m - 1)^L/L$ nonfrozen sectors in PBC, compared to $\sim (m - 1)^L$ nonfrozen sectors in OBC, or $\sim (m - 1)^L$ frozen states in either case.

C.2.4 Frozen states in the QF model

The counting of frozen states in the presence of periodic boundaries is more complicated than the case of open boundary conditions presented in the main text. We will work using the language of the QF Hamiltonian (i.e., spins on edges) and with square systems of size $L \times L$ for simplicity. The first ingredient in counting the number of such states is to identify the number of 1D configurations that are not mobile under pair-flip dynamics; namely, the number of configurations that do not contain any neighbors of the same color. When these 1D configurations are turned into system-winding loops in the second dimension, there will be no adjacent loops of the same color. For a ring of length j , the number of configurations with no identically colored neighbors is $(m - 1)^j + (m - 1)(-1)^j$. Suppose that such a constraint-satisfying pattern with $j = L$ is placed in the first row of the system. In the subsequent rows, the pattern can be shifted either left or right subject to the constraint that it must come back to itself around the periodic boundaries. Consequently, any *periodicity* of the pattern plays a nontrivial role; if the pattern repeats every j edges, the final displacement x of the pattern need only satisfy $x = 0 \pmod{j}$.

For simplicity, we will first focus on linear system sizes of the form $L_k = 2^k$, although the methods we present can be used to identify the number of frozen states for arbitrary L . Given this simplification, the pattern can, in principle, repeat every $j_n = 2^n$ edges for $1 \leq n \leq k$. For $k > 1$,

the number of frozen patterns of length L_k with no periodicity is

$$N_k = (m-1)^{L_k} + (m-1)(-1)^{L_k} - \sum_{1 < n < k} N_n, \quad (\text{C.15})$$

where the second term on the right-hand side subtracts off the contribution from periodic patterns; more generally, one must sum over all divisors of the length of the pattern, as in Eq. (C.14). The recursion relation (C.15) can be solved exactly to give

$$N_k = (m-1)^{L_k/2} \left[(m-1)^{L_k/2} - 1 \right] \text{ for } k > 1, \quad (\text{C.16})$$

and $N_1 = m(m-1)$. Asymptotically, we have $N_k \sim (m-1)^{L_k}$ for $k \gg 1$, as expected. That is, the contribution from periodically repeating patterns is exponentially suppressed. For a system of size $L_k \times L_k$, the full number of frozen configurations that wrap around the system in (at least) one direction is therefore

$$F_k = \sum_{j \mid L_k} \sum_{n=0}^{2L_k/j} \binom{L_k}{\frac{1}{2}nj} N_\ell, \quad (\text{C.17})$$

where the first summation is over nontrivial motif lengths j that divide L_k , i.e., $j \in \{2^n\}_{n=1}^k$. The leading term in the summation comes from the term $j = L_k$, which gives (for $m > 2$) the asymptotic growth

$$F_k = \left[2 + \binom{L_k}{\frac{1}{2}L_k} \right] N_{L_k} + O\left(\frac{2^{L_k}}{\sqrt{L_k}}(m-1)^{L_k/2}\right) \sim \sqrt{\frac{2}{\pi L_k}} [2(m-1)]^{L_k}, \quad (\text{C.18})$$

For $m = 2$, there is just a single frozen pattern composed of alternating colors of loops. Since this pattern necessarily has periodicity $j = 2$, there is no exponential enhancement of large, nonrepeating patterns. Hence, in this case, one must sum over all binomial coefficients, giving $\sum_{n=0}^{L_k} \binom{L_k}{n} = 2^{L_k}$. The asymptotic scaling in Eq. (C.18) is compared with the exact number of frozen states computed numerically for arbitrary L in Fig. C.4, which suggests that (C.18) describes the leading asymptotic growth for all even L . Note that an exact count of *all* frozen states would require us to enumerate configurations that wrap the torus in the other direction [not all of which are distinct from the

states already counted in Eq. (C.17)]; the asymptotic growth, however, will remain unchanged.

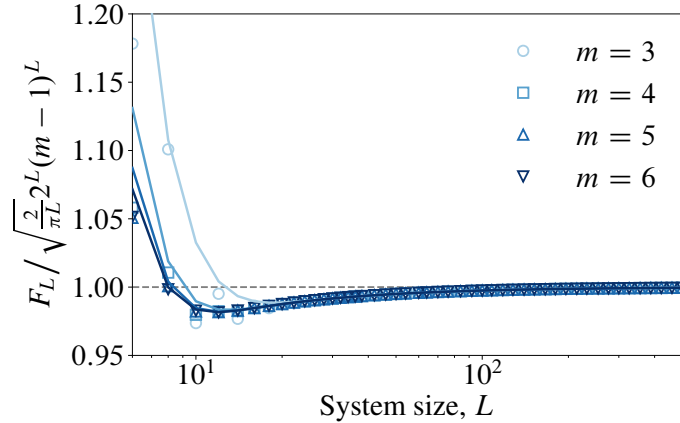


Figure C.4: Exact number of frozen states that wrap around the torus in one direction (C.17), obtained by numerical evaluation of the recursion relation (C.15), relative to the predicted asymptotic scaling (C.18) as a function of linear system size L (only even L are plotted). For all m , the asymptotic scaling is obeyed for sufficiently large L . The solid lines correspond to the contributions to (C.17) from $j = L$ and $j = L/2$, which provide a good description of the behavior down to $\mathcal{O}(1)$ values of L .